

May 2017

Adaptive Region-Based Approaches for Cellular Segmentation of Bright-Field Microscopy Images

Hady Ahmady Phoulady

University of South Florida, parham.ap@gmail.com

Follow this and additional works at: <http://scholarcommons.usf.edu/etd>

 Part of the [Computer Engineering Commons](#), and the [Computer Sciences Commons](#)

Scholar Commons Citation

Ahmady Phoulady, Hady, "Adaptive Region-Based Approaches for Cellular Segmentation of Bright-Field Microscopy Images" (2017).
Graduate Theses and Dissertations.
<http://scholarcommons.usf.edu/etd/6794>

This Dissertation is brought to you for free and open access by the Graduate School at Scholar Commons. It has been accepted for inclusion in Graduate Theses and Dissertations by an authorized administrator of Scholar Commons. For more information, please contact scholarcommons@usf.edu.

Adaptive Region-Based Approaches for Cellular Segmentation of
Bright-Field Microscopy Images

by

Hady Ahmady Phoulady

A dissertation submitted in partial fulfillment
of the requirements for the degree of
Doctor of Philosophy
Department of Computer Science and Engineering
College of Engineering
University of South Florida

Co-Major Professor: Dmitry Goldgof, Ph.D.

Co-Major Professor: Lawrence Hall, Ph.D.

Rangachar Kasturi, Ph.D.

Peter R. Mouton, Ph.D.

Tapas K. Das, Ph.D.

Date of Approval:

May 10, 2017

Keywords: Medical Image Processing, Nucleus Detection, Classification,
Machine Learning, Computer-Aided Diagnosis

Copyright © 2017, Hady Ahmady Phoulady

Dedication

To my mother and father, Zahra and Mahdy.

Acknowledgments

I would like to sincerely thank my advisers Dr. Dmitry Goldgof and Dr. Lawrence Hall for their continuous encouragement, support and guidance throughout this research. I would also like to thank Dr. Peter Mouton for his continuous support and collaboration.

Moreover, I would like to thank Dr. Rangachar Kasturi and Dr. Tapas Das for agreeing to serve on my dissertation committee and for their constructive comments.

Table of Contents

List of Tables	iv	
List of Figures	v	
Abstract	vii	
Chapter 1	Introduction and Overview	1
1.1	Motivation	1
1.2	Cancers	2
1.2.1	Cervical Cancer	3
1.2.1.1	Causes	3
1.2.1.2	Screening	4
1.3	Cytology vs Histology	6
1.3.1	Staining	6
1.4	CAD Systems	7
1.5	Dissertation Overview	9
Chapter 2	Related Work	11
2.1	Nucleus Detection	12
2.2	Nucleus Segmentation	18
2.2.1	Intensity Based Approaches	18
2.2.2	Region Based Approaches	19
2.2.3	Level Set Methods	20
2.2.4	Probabilistic Models	21
2.2.5	Graphical Models	21
2.2.6	Machine Learning Approaches	22
2.3	Cervical Cytology	24
2.3.1	Nucleus Segmentation	25
2.3.2	Free-lying Cell Segmentation	26
2.3.3	Overlapping Cell Segmentation	27
Chapter 3	Hierarchical Multilevel Thresholding for Nucleus Segmentation in Histology Images	30
3.1	Introduction	30
3.2	Method	31
3.2.1	Overview of the Method	31

3.2.2	Preprocessing	31
3.2.3	Automated Threshold Selection	33
3.3	Dataset	34
3.4	Results	34
3.5	Discussion	36
3.6	Summary	37
Chapter 4	Cervical Tissue Segmentation and Classification Using an Ensemble Approach	39
4.1	Introduction	39
4.2	Methods	42
4.2.1	Basic Segmentors	42
4.2.2	Non-Convex Blobs	44
4.2.3	Parameter Space	45
4.2.4	Case Removal	46
4.2.5	Volume Estimation	46
4.2.6	Final Estimated Volumes	47
4.3	Dataset	47
4.3.1	Image Acquisition	48
4.4	Results and Discussion	48
4.5	Summary	51
Chapter 5	Cervical Tissue Segmentation and Classification Using Adaptive Shape Modeling	53
5.1	Introduction	53
5.2	Methods	55
5.2.1	Adaptive Image Segmentation	56
5.2.2	Nucleus Shape Approximation by Ellipse Fitting	57
5.2.3	Feature Extraction and Classification	58
5.3	Dataset	59
5.4	Results and Discussion	59
5.4.1	Parameter Selection and Results	60
5.4.2	Discussion	61
5.5	Summary	62
Chapter 6	Overlapping Cervical Cell Segmentation in Cervical Cytology Images	64
6.1	Introduction	64
6.2	Methods	68
6.2.1	Nucleus Detection and Segmentation	68
6.2.2	Clump Segmentation	71
6.2.3	Cytoplasm Segmentation	72
6.2.3.1	Boundary Approximation	72
6.2.3.2	Coarse Refinement	74
6.2.3.3	Fine Refinement	75

6.3	Datasets	78
6.4	Results	79
6.4.1	Evaluation Metrics	80
6.4.2	Results on ISBI 2015 Dataset	82
6.4.3	Comprehensive Results on Both Datasets	84
6.4.3.1	Nucleus Detection	86
6.4.3.2	Cell Detection and Segmentation	87
6.5	Discussions	89
6.6	Summary	91
Chapter 7	Conclusions	93
7.1	Summary	93
7.2	Contributions	94
7.3	Future Directions	96
References		98
Appendices		116
Appendix A	Permissions for Use	117
About the Author		End Page

List of Tables

Table 3.1	Results summary - superior results are shown with bold font.	35
Table 4.1	AUC and accuracy of the methods	50
Table 6.1	Number of annotated cells in training and test set of the datasets.	79
Table 6.2	Four sets of values producing the two highest GM measures, highest DSC and lowest FNRo on training set of ISBI 2015 dataset.	84
Table 6.3	Comparison between current version with previous version of the method on test set of ISBI 2015 dataset.	84
Table 6.4	Detailed results of the framework on 810 synthetic images in the test set of the ISBI 2014 dataset.	85
Table 6.5	Nucleus detection methods results on 810 synthetic images in the test set of ISBI 2014 dataset.	87
Table 6.6	Four sets of values producing the two highest GM measures, highest DSC and lowest FNRo on the training set of ISBI 2014 dataset.	87
Table 6.7	Results of the framework and comparison with the other state-of-the-art methods.	88

List of Figures

Figure 1.1	Progression from HPV infection to invasive cancer.	5
Figure 2.1	Intermediate results of the segmentation method by Wienert et al.	15
Figure 2.2	Intermediate results of the segmentation method by Hafiane et al.	17
Figure 2.3	Intermediate results of the segmentation method by Veta et al.	20
Figure 2.4	Intermediate results of the improved joint optimization algorithm by Lu et al.	29
Figure 3.1	Flow of the hierarchal multilevel thresholding approach.	32
Figure 3.2	Segmentation results of four images in dataset.	36
Figure 4.1	Samples of cervical cytology and histology images.	40
Figure 4.2	Overview of the algorithm.	41
Figure 4.3	Results of Segmentor 3.	42
Figure 4.4	Sample results of final segmentation.	44
Figure 4.5	ROC curve for Image Ensemble and variants of Large Ensemble.	49
Figure 5.1	Overview of the proposed Adaptive Nucleus Shape Modeling (ANSM).	56
Figure 5.2	Steps of the segmentation algorithm.	59
Figure 5.3	Tissue classification accuracy.	62
Figure 5.4	Images from normal tissues.	62
Figure 6.1	The results of the framework steps on a real cervical cytology EDF image.	69
Figure 6.2	Histogram of pixel intensities of an EDF cervical cytology image in the training dataset, the estimated Gaussian Mixture Model and the selected threshold.	72
Figure 6.3	Coarse refinement: the subimages not reachable by centroid subimage are removed.	75

Figure 6.4	Fine refinement: the approximated boundary (red line) and the result (dashed red line) of selecting highest weighted gradient points on radials followed by Savitzky–Golay filter.	77
Figure 6.5	Visualization of results produced by different values of α and β .	83
Figure 6.6	Visualization of results in Table 6.4.	86
Figure 6.7	Five images with very low contrast nuclei (red and green lines are ground truth and segmentation region boundaries, respectively).	89
Figure 6.8	The ground truth (top row) and the nucleus and overlapping cells segmentation results of two real EDF and four synthetic images with nucleus.	90

Abstract

Microscopy image processing is an emerging and quickly growing field in medical imaging research area. Recent advancements in technology including higher computation power, larger and cheaper storage modules, and more efficient and faster data acquisition devices such as whole-slide imaging scanners contributed to the recent microscopy image processing research advancement. Most of the methods in this research area either focus on automatically process images and make it easier for pathologists to direct their focus on the important regions in the image, or they aim to automate the whole job of experts including processing and classifying images or tissues that leads to disease diagnosis.

This dissertation is consisted of four different frameworks to process microscopy images. All of them include methods for segmentation either as the whole suggested framework or the initial part of the framework for future feature extraction and classification. Specifically, the first proposed framework is a general segmentation method that works on histology images from different tissues and segments relatively solid nuclei in the image, and the next three frameworks work on cervical microscopy images, segmenting cervical nuclei/cells. Two of these frameworks focus on cervical tissue segmentation and classification using histology images and the last framework is a comprehensive segmentation framework that segments overlapping cervical cells in cervical cytology Pap smear images.

One of the several commonalities among these frameworks is that they all work at the region level and use different region features to segment regions and later either expand, split or refine the segmented regions to produce the final segmentation output. Moreover, all proposed frameworks work relatively much faster than other methods on the same datasets.

Finally, proving ground truth for datasets to be used in the training phase of microscopy image processing algorithms is relatively time-consuming, complicated and costly. Therefore, I designed the frameworks in such a way that they set most (if not all) of the parameters adaptively based on each image that is being processed at the time. All of the included frameworks either do not depend on training datasets at all (first three of the four discussed frameworks) or need very small training datasets to learn or set a few parameters.

Chapter 1

Introduction and Overview

1.1 Motivation

Cancer diagnosis relies on tissue and cellular analysis. Conventional analysis includes viewing cell smears or tissues under a microscope, examining the structure and functions of cells (cytology) or tissues (histology), scoring the expression and diagnosing or grading the disease, most of which is done manually. Using computer-aided diagnosis (CAD) systems to facilitate this process is desirable for several reasons, a few of which are listed below.

- Manual analysis is prone to interobserver variability and misdiagnoses: two pathologists can look at the same tissue and make a different diagnosis [1]. Also, misdiagnoses are occurring frequently at the rate of 15% to 28% according to The American Journal of Medicine and BMJ Quality and Safety respectively [2]. These misdiagnoses can subsequently lead to a patient's emotional distress, unnecessary practices and malpractice claims. It is estimated that medical errors cost between \$17 billion and \$29 billion annually in the U.S. [3].
- The workload on pathologists can be reduced by detecting benign areas and directing pathologists to work on more suspicious areas. For example, around 80% of all performed prostate biopsies in the U.S. are benign, suggesting that prostate pathologists are spending large portion of their time on benign tissues [4].
- Pathology quantification cannot be easily done by the human visual system. For example, to grade breast cancer, based on the commonly used modified Bloom-Richardson

system, tubule formation, nuclear atypia and mitotic rate need to be assessed which are hampered by observer variability [5]. Moreover, quantifying chromatin distribution, comparing average nuclear areas, assessing some morphometric descriptions, etc. are nearly impossible manually [1].

Increasing availability of automated and semi-automated microscope slide scanners, such as cost and time efficient whole slide imaging (WSI) scanners, have lead to a growing amount of image data which subsequently made CAD one of the major research subjects in medical imaging [6, 4]. CAD systems can automate manual medical procedures, help doctors by guiding them in medical operations and reduce their workload by localizing regions of interests. Therefore, they will facilitate medical research, decrease the costs of medical treatments and ultimately lead to earlier disease diagnosis while reducing mortality rates and emotional distress.

This chapter presents an introduction to the cancer diagnosis and the main approaches in which CAD systems tackle different tasks im microscopy image processing. In Section 1.2 the burden of cancers, specifically cervical cancer and its causes and screening are discussed. Section 1.3 compares cytology to histology and discusses tissue staining. Section 1.4 presents and discusses different category of methods in CAD systems designed for image segmentation, and finally in Section 1.5 the dissertation overview is presented.

1.2 Cancers

Diseases, such as different cancers, put a huge financial and emotional burden on the society. Only in the U.S., about 1,685,210 new cancer cases are expected to be diagnosed¹ and about 595,690 Americans are expected to die of cancer, which translates to about 1,630 people per day in 2016, according to American Cancer Society [7]. The Agency for Healthcare Research and Quality estimates that the medical costs for cancer in the U.S. were \$74.8

¹Excluding carcinoma in situ of any site except urinary bladder and basal cell or squamous cell skin cancers.

billion, in 2013 [7]. Moreover, in the U.S., the lifetime risk of developing cancer is 42% (1 in 2) in men and 38% (1 in 3) in women and it is the second most common cause of death, exceeded only by heart disease, and accounts for nearly 1 of every 4 deaths [7]. These facts and estimates highlight the importance of CAD systems.

1.2.1 Cervical Cancer

It is estimated that 12,900 new cases of invasive cervical cancer will be diagnosed in 2015 and it will result in 4,100 deaths in the U.S., according to American Cancer Society [7]. Although cervical cancer is not among the 10 most common cancers among women in the U.S., it is of much higher concern in lower-resource countries: it is the most prevalent cancer among women in 39 of the 184 countries worldwide, and is the leading cause of deaths from cancer in women in 45 countries [8]. Currently, worldwide, cervical cancer is the fourth most common cancer and the fourth cause of cancer death in women [8].

1.2.1.1 Causes

Virtually all cervical cancers are caused by persistent infection of high-risk Human papillomavirus (HPV) types which is the most common sexually transmitted infection in the U.S. [9]. HPV types 16 and 18 alone account for around 70% of all cervical cancer incidences. After infection with HPV, it may access the basal cells through micro-abrasions in the cervical epithelium [10] and cause cellular changes. Although most new infections will be suppressed by the immune system within 1 to 2 years without causing cancer, if not cleared, they may cause precancerous lesions. Typically within 5-10 years of infection, around 10% of new infections may persist and develop into precancerous lesions [11]. About 20% of precancerous lesions subsequently progress and develop into invasive cancer over many years, even decades. The slow overall progression of HPV infection into invasive cervical cancer makes its prevention more practical.

1.2.1.2 Screening

Although cervical cancer is one of the most deadly cancers in women worldwide, it is also one of the most preventable cancers with early screening. Cervical cancer incidence and mortality rates have decreased by more than 50% over the past three decades, with most of the reduction attributed to screening with the Papanicolaou (Pap) test, which can detect both cervical cancer and precancerous lesions [9]. In the U.S., the conventional Pap test has been replaced by an automated liquid-based Pap cytology test, in which, cervical cells are collected with plastic devices, either a cervical broom or combined plastic spatula and cervical brush, and are transported to a laboratory in preservative liquid [12]. There, they are processed to produce slide preparations using one of the approved systems, SurePath or Thin Prep, by the Food and Drug Administration (FDA).

The Bethesda System (TBS) is used to report the Pap test result. A Pap test result will be negative if there are no epithelial cell abnormalities. For abnormalities four main categories of results are as below.

- Atypical Squamous Cells (ASC): It can be either atypical squamous cells of undetermined significance (ASC-US) or atypical squamous cells (ASC-H) which cannot exclude a High-grade squamous intraepithelial lesion (HSIL).
- Low-grade Squamous Intraepithelial Lesions (LSILs): It shows the existence of mild dysplasia or cervical intraepithelial neoplasia, grade 1 (CIN-1). CIN-1 is not considered precancerous lesion and most of their cases will clear without any treatment.
- High-grade Squamous Intraepithelial Lesions (HSILs): It means that more severe abnormalities than LSIL exist. HSILs contain cells with moderate or severe dysplasia and may be classified as CIN-2 or CIN-3.
- Squamous Cell Carcinoma (SCC): It is invasive cervical cancer which invades deeply into cervix or other tissues or organs.

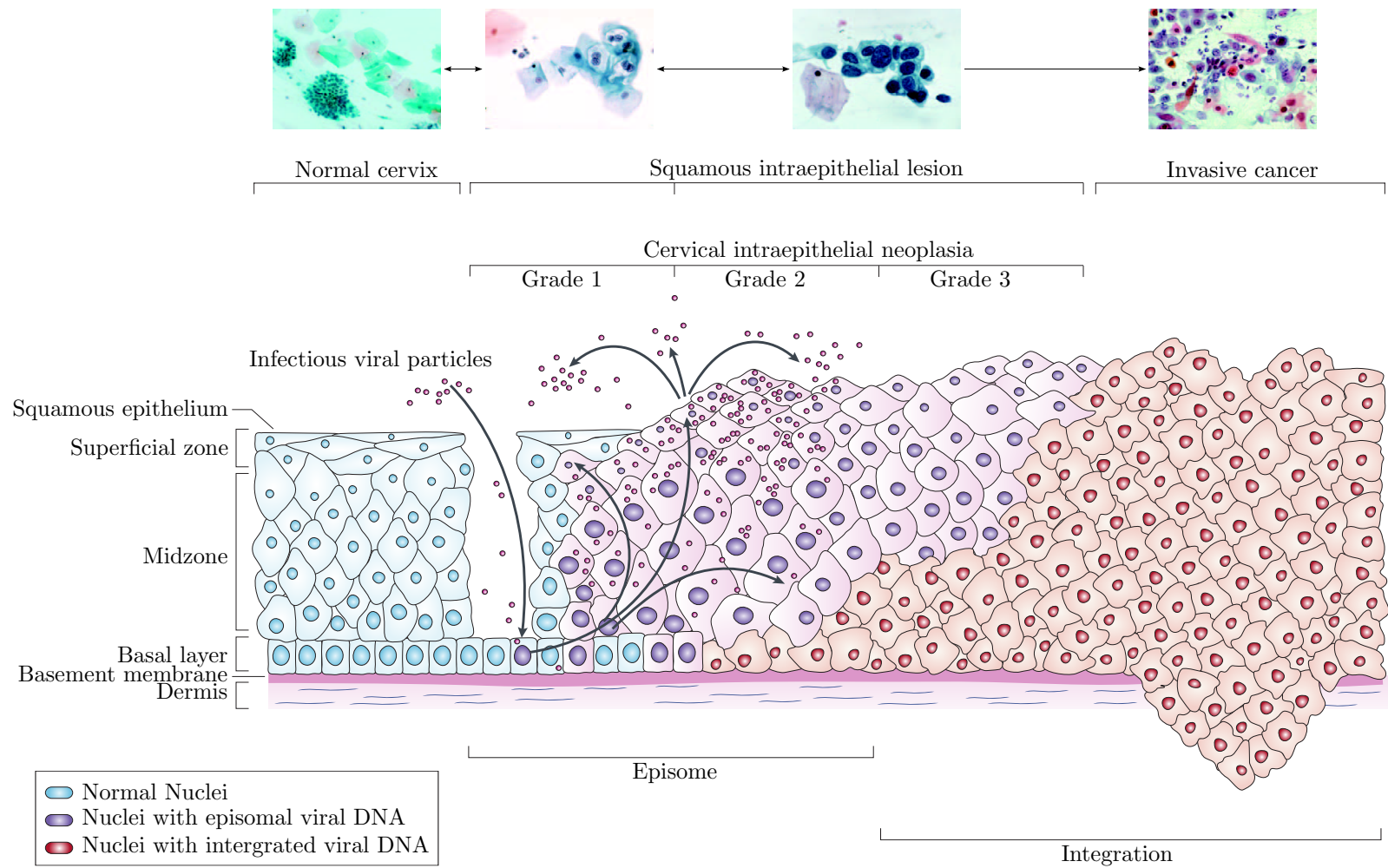


Figure 1.1: Progression from HPV infection to invasive cancer (Diagram is reused from [10] and four top images are taken from [11] – the second image from left shows an LSIL and the third image from left shows an HSIL. Permission of use can be found in Appendix A.)

Fig. 1.1 shows different stages of an HPV infection and its progression to invasive cervical cancer, with sample images from normal cervix, CIN-1, CIN-2/3 and invasive cancer.

If a Pap cytology test shows high risks of developing precancerous or cancer, usually a biopsy is performed and diagnosis and treatment are done based on histology. Actually, the clinical histology process begins when the physician determines that the treatment cannot proceed further without histology confirmation [1].

1.3 Cytology vs Histology

Microscopic image analysis includes processing and analysis of microscopy images which are obtained through one of the two main processes: cytology and histology. Cytology is the microscopic examination of cells whereas histology is the microscopic inspection of plant or animal tissue. Histology in comparison to cytology is usually more expensive, complicated, comprehensive, invasive and reliable [13, 14]. Because of faster preparation and being less invasive, cytology tests, such as cervical Pap smear, are more common. However, histology is considered the *gold standard* in diagnosing almost all types of cancers [4, 15].

1.3.1 Staining

Tissue samples or cell smears are stained to highlight different components of tissue or different parts of cell tissue. There are several histology stains. Some of them are used for very specific biological tissues, while some others are used for general purposes. The most common combination of histology stains used for general purpose staining is hematoxylin and eosin (H&E). Hematoxylin binds to acidic structures and appears blue/purple, while eosin is an acid aniline dye and stains basic structures and proteins and appears pink/red. Due to the presence of nucleic acids, hematoxylin binds to nuclei and they appear blue/purple. Cytoplasm, connective tissue, red blood cells, etc., bind with eosin and appear pink/red.

One of the advantages of different colors obtained by hematoxylin and eosin is that staining can be separated. The color formation in images produced with brightfield microscopy can be modeled based on the Lambert-Beer law. Ruifrok and Johnston [16] proposed a method to separate immunohistochemical. Using their proposed method colors in H&E stained images can be separated into hematoxylin, eosin and background channels. Using the hematoxylin channel to detect and segment nuclei can potentially improve the performance, because nuclei have higher contrast with surrounding structures in the hematoxylin channel image than the grayscale image. On a different note, technical or appearance variability (caused by different processes of preparation) can pose a difficulty in segmenting nuclei. Color normalization algorithms [17, 18] have been proposed to normalize staining in different images. It has been shown that stain normalization can improve segmentations [18, 16].

1.4 CAD Systems

In this section the nucleus segmentation algorithms used in different CAD systems are discussed. Based on how an algorithm approaches segmenting nuclei, most of the segmentation methods can be divided into two categories: pixel-based [19, 20, 21, 22, 23] and boundary-based [24, 25, 26, 27]. Pixel-based methods focus on classifying pixels as belonging to nuclei or background and boundary-based methods segment nuclei by finding the boundaries. Other than level set methods which find the boundaries of regions, most of the other methods classify pixels using thresholding, morphological operations, classifiers, watershed segmentation, probabilistic models, etc. The segmentation algorithms of microscopy images in the literature [4, 28, 5, 29, 1, 30, 31] can be broadly divided into six main categories, based on the main component of their algorithms as follows ².

²Many algorithms have a combination of these type of approaches in different steps and therefore, this categorization is clearly not optimal.

1. Intensity Based Approaches: Intensity based approaches [32, 33, 34, 35, 36, 37] use (adaptive) thresholding, contour tracing algorithms and morphological operations as their main tools to segment nuclei. They are usually developed for specific purposes (single type of tissue/image), are not generalizable and are susceptible to technical variability and staining variation. Such approaches use image information at the pixel level and therefore, do not take advantage of object level features. Although they may not obtain a very accurate segmentation, they are usually faster than other type of approaches and can achieve acceptable results in almost real time.
2. Region Based Approaches: Region based approaches [20, 22, 38, 39, 40, 22, 41, 42, 43, 44, 45], e.g. watershed segmentation and region growing, work by merging or dividing regions based on some criteria. Watershed segmentation methods usually over-segment the image and an extra step is needed to merge some regions or refine the region boundaries. Most of these approaches, whether they grow the region or divide the region to construct the segmentation, need seed points and therefore, are coupled with some nucleus detector algorithms described earlier.
3. Level Set Methods: Level set methods [24, 25, 26, 46, 27, 47, 48, 49, 50, 51, 52, 53], e.g. active contours, are one of the most popular approaches for microscopy image segmentation. They are computationally expensive, but can provide accurate segmentations. Active contours are deformable models that try to minimize an energy function based on image gradient and contour shape. Therefore, they are mostly segmenting regions by fitting to regions boundaries. Active contours can fit to boundaries most accurately if they are initialized close to the boundary. Therefore, these methods need initial seeds too and are usually coupled with detection algorithms.
4. Probabilistic Models: Probabilistic models [54, 55, 56, 57] represent nuclei as weighted sum of several Gaussian densities or as a mixture of Gaussian and other (e.g. Gamma)

densities [57] or create probability maps and determine the probability of each pixel belonging to a nucleus [55].

5. Graphical Models: Graphical models [58, 59, 60, 61, 62], e.g. graph cuts, represent the image as a graph in which pixels are nodes and pixel adjacencies are edges. A segmentation using these models partitions the graph into subgraphs so that the similarity within subgraphs is high and similarities between subgraphs is low. Although graph cuts [63, 64, 65, 66] were introduced and used in the computer vision more than two decades ago, they were not very popular for microscopy image segmentation until recently [59, 67, 60, 61, 62].
6. Machine Learning Approaches: Machine learning is another popular category of approaches which aim to cluster or classify pixels as different nuclei [19, 68, 69, 70, 71, 72, 73, 74, 75, 76]. Unsupervised or semi-supervised clustering algorithms or other classifiers such as Support Vector Machine (SVM) classifiers are used to construct a rough segmentation and usually another step is needed to refine the segmentation. A downside for these approaches is that they need training data.

1.5 Dissertation Overview

In this dissertation I explored several CAD systems that are designed to process microscopy medical images and diagnose cancers, specifically cervical cancer. This research focuses on cervical tissue segmentation and classification and the main aim is to design CAD systems for cervical cancer diagnosis with algorithms that have fewer steps overall, need less parameter tuning and are less sensitive to batch effects. Efficient and more accurate CAD systems to diagnose cervical cancer in cervical cytology images can lead to a more cost effective cervical screening by reducing the workload of the pathologists. Hence, it

can potentially decrease the mortality rate from cervical cancer in women especially in less developed countries with limited access to resources.

Chapter 2 discusses the recent methods and CAD systems. In Chapter 3, a method to segment nuclei in histology images is proposed. In Chapter 4, an ensemble approach for cervical tissue classification is proposed. Chapter 5 presents a framework to segment cervical histology images and classify cervical tissues using the nucleus level texture features. In Chapter 6, a method for segmenting overlapping cervical cells in Pap smear cervical cytology images is presented. Finally, in Chapter 7, the dissertation is summarized, the contributions are discussed, and future directions are presented.

Chapter 2

Related Work

Most of the limited work on analysis of cervical histology images aims to classify the tissues [77, 78, 79] and cervical histology image segmentation is less addressed [68]. On the contrary, a large focus in microscopy medical image analysis is on breast cancer histology images [22, 19, 80, 71, 26] and they mostly tackle the task of detection and segmentation of (overlapping) nuclei. This difference of focus levels can be justified: the majority of women in developed countries do repeated cervical screening, which is mostly done by the Pap cytology test and only a very small percentage of those patients undergo a biopsy. So, in other words, automation in cervical cytology is of much higher importance than cervical histology. However, breast cancer is the most prevalent cancer in women [8] and with a reported suspicious abnormality by mammography or ultrasound test, a biopsy is performed and diagnosis is carried out by histology confirmation. Because most sophisticated methods on histology image segmentation are proposed to segment images other than cervical histology images and because of the fact that most of these methods can potentially be modified to work on cervical histology images, I will also review the methods proposed and evaluated for other histology images, mostly breast histology images.

Most of the focus of CAD systems in histology is on nuclei and their degrees of abnormality¹ while in cytology nuclei and their corresponding cytoplasms² are of interest.

¹In histology, algorithms mostly try to detect or segment (and/or classify) nuclei rather than cells.

²Cell structure and features, such as ratio of nucleus area to cytoplasm area, are the most important factors for diagnosis in cytology.

In the following two sections I will investigate some of the most recent advances on nucleus detection and segmentation in histology. Then, in the third section I will review most recent algorithms for cervical cytology segmentation.

2.1 Nucleus Detection

Most of segmentation methods, such as region growing methods and watershed algorithms, depend on initial markers or seed points. Level set methods also usually need to initialize contours close to nuclei boundaries. Therefore, nucleus detection is a critical task. Commonly, algorithms detect nuclei using adaptive thresholding [81], peaks of Euclidean distance map and Laplacian of Gaussian (LoG) to find centers of large blobs [82, 67], color clustering of the pixels to identify subcellular components (nuclei, cytoplasm, neuropil, and background) [83], H-maxima/minima transform to detect maxima/minima as seeds [20, 68, 59] and a Hough transform to detect circular-shaped regions [84]. Fuzzy c-means clustering [48] and the expectation maximization (EM) algorithm [26] have also been employed. These methods are generally based on the assumption that nuclei are circular-shaped regions with relatively low and homogeneous intensity and a predetermined range of sizes. However, these assumptions usually do not hold for severely abnormal nuclei which can have very large sizes and heterogeneous area.

Dalle et al. [82] proposed a method that detects only a subset of *critical* nuclei which is used for a segmentation algorithm to ultimately score the nuclear pleomorphism in histopathological images. The proposed nucleus detector algorithm uses thresholding and morphological operations to detect the seeds and uses a distance transform to estimate the size of nuclei and reject those which are larger than a threshold. Detected patches of images are later transformed into a polar coordinate system and the nuclei are segmented. Then, using biquadratic filtering they produced a gradient image from which nuclei boundaries are delineated.

Nucleus detection can also be considered as a classification problem. Han et al. [85] trained a Support Vector Machine (SVM) classifier with positive and negative training sub-images centered at the nucleus centroid. They used raw pixel intensities and Laplacian of Gaussian edge intensities as the features and detected rectangular windows inside the images.

Some nucleus detectors perform the detection in two major steps: they first over-detect blobs and then rejects some of the blobs and keeps the other candidates. Three such methods are described below.

- Basavanhally et al. [23] proposed a region growing method to detect lymphocyte nuclei based on the fact that they are circular regions of low and continuous intensity. They smoothed the image with Gaussian kernels at different scales, and selected the darkest pixels at each scale as seeds. The seeds were expanded in a growing process: for each seed, n , a bounding box with size $12\sigma_G \times 12\sigma_G$ was constructed, where σ_G is the standard deviation used to create the Gaussian kernel. Then at each iteration, the darkest pixel along the eight-connected region boundary was added to the region. The growing process continued until a pixel on the boundary of the bounding box was added. Then the intermediate region which had the highest difference between its inner and outer boundaries was selected. This method over-detected lymphocytes and they used maximum a posteriori (MAP) estimation that incorporated size, luminance, and spatial proximity information to reject some of the regions.
- Wienert et al. [33] employed a contour tracing approach [86] to detect cells in a dataset composed of histological images from various tissues. Contour start pixels were defined as the positions at which the gradient between each pair of neighboring local minima/maxima or maxima/minima was maximal. Subsequently, the object contours were followed clockwise using an eight-connected neighborhood and those contours which reach their corresponding start pixel were considered valid. The *importance* of contours was measured by *mean gradient* and *gradient fit*. A non-overlapping segmen-

tation was then constructed by assigning each pixels to the most important contour (Fig. 2.1b). The resulting contours were then optimized using a distance transformation [87] (Fig. 2.1c) and some of them were rejected based on a concavity check (Fig. 2.1d). To classify the final contours as cell nuclei and other objects, color deconvolution [16] was used and those contours which have a higher Hematoxylin intensity than a threshold, computed by Otsu thresholding [88], were selected as cell contours (Fig. 2.1e). The total number of initial contours found from image in (Fig. 2.1a) was 29,815 and after different steps 119 cell contours remained in the final segmentation (Fig. 2.1e).

- Arteta et al. [89] employed a popular and efficient maximally stable extremal region (MSER) detector [90] to find initial regions. The MSER detector finds extremal regions which are *maximally stable* in the sense that the speed of their area variation with respect to changing a threshold t (which is used to binarize the image) is a local minimum and is below a separate *stability* threshold. By choosing a high similarity threshold, cell regions were over-detected. To each region a score, measuring how likely it is a cell region, was assigned using a classifier. A 92-dimensional feature vector was computed and learning was done in a principled fashion from the dot-annotated training data using a structured SVM classifier. The regions were organized into trees according to the nestedness property, so that each tree corresponded to a set of overlapping extremal regions, and a set of non-overlapping regions were selected in a dynamic programming fashion which maximized the sum of its regions' scores.

Other than the approach proposed by Arteta et al. [89], there exist a few other recent nucleus detectors which perform reasonably well and are applicable to different modalities. Hafiane et al. [48] proposed a nucleus detector by combining a fuzzy c-means with spatial constraints, active contours and iterative voting. Their method has three steps:

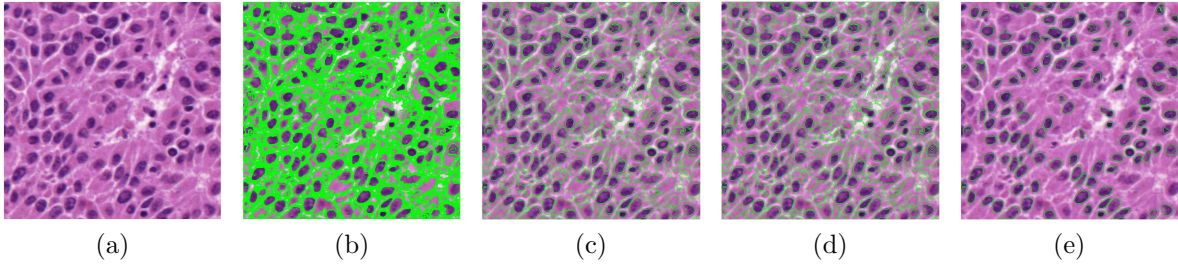


Figure 2.1: Intermediate results of the segmentation method by Wienert et al. (a) Original image and (b–e) results of different steps of the algorithm in [33] (Images are reused from [33]). Permission of use can be found in Appendix A).

- Fuzzy c-means clustering with spatial constraints is used to find potential regions. Traditional fuzzy c-means clustering algorithm minimizes the objective function $J(U, V)$ defined by the sum of similarity measured as,

$$J(U, V) = \sum_{i=1}^C \sum_{j=1}^N u_{ij}^m \|\mathbf{x}_j - \mathbf{v}_i\|^2, \quad (2.1)$$

where $X = \{\mathbf{x}_1, \mathbf{x}_2, \dots, \mathbf{x}_N\}$ denote the pixel feature vector and $V = \{\mathbf{v}_1, \mathbf{v}_2, \dots, \dots, \mathbf{v}_C\}$ represents the prototypes, known as the clusters centers. Also, $U = [u_{ij}]$, $u_{ij} \in [0, 1]$ is the partition matrix which satisfies the condition: $\sum_i^C u_{i,j} = 1, \forall j$ and m is a fuzzifier which indicate the fuzziness of membership for each point. It has been shown that incorporating spatial information brings more robustness and efficiency to the fuzzy c-means algorithm [91], thus, changing the objective function $J(U, V)$ in (2.1) to

$$J_m(U, V) = J(U, V) + \alpha \sum_{i=1}^C \sum_{j=1}^N u_{ij}^m \exp^{-\sum_{k \in \Omega} u_{ik}^m}, \quad (2.2)$$

where Ω is a set of neighbors, and α is the weight of the term containing spatial information. Optimization of 2.2 is solved by using Lagrange multipliers.

- Multiphase vector-based active contours were used to refine the segmentation obtained in the previous step. They used a variant of a multiphase level set framework proposed

by Vese and Chan [92] which involves minimization of a reduced or weak Mumford-Shah functional $F_n(c, \phi)$ [93] and is an extension to their two-phase level set segmentation algorithm [94]. The multiphase approach enables efficient partitioning of the image into n classes using just $\log(n)$ level sets without leaving any gaps or having overlaps between level sets. They simplified the computation of the length term in the reduced Mumford and Shah energy function by replacing the measure of the characteristic functions with the sum of the length of the zero-level sets of ϕ_i . They also used an edge stopping function obtained from Beltrami color metric tensor to define a geodesic length measure to make the approach *vector-based*. Therefore, their proposed variant also works on higher dimensional (color) images.

- Individual nucleus centers were then detected from the nuclei clusters segmented in the previous step. They used a technique based on iterative voting using the oriented kernels approach described in [95, 96]. The approach is immune to noise and detects nuclei centers from incomplete boundary information through voting and perceptual grouping by applying a series of cone-shaped kernels that vote iteratively along the radial or tangential directions [7]. The iterative approach refined the center of mass at each iteration until it converged to a focal response. At each iteration and location on the contour the voting kernel was aligned along the maximum response of the voting space and the shape of the kernel was refined. Fig. 2.2 shows the evolution of the voting landscape $\mathbf{V}(i, j)$ in a synthetic and a nucleus cluster image test image.

Some of the other more recent methods which can be specifically used to detect blobs are as follows.

- Radial basis symmetry that was proposed by Loy and Zelinsky [97] is a gradient-based algorithm to detect regions with high radial symmetry, and has been used by several other segmentation algorithms as a nucleus detection method [22, 41]. It determines

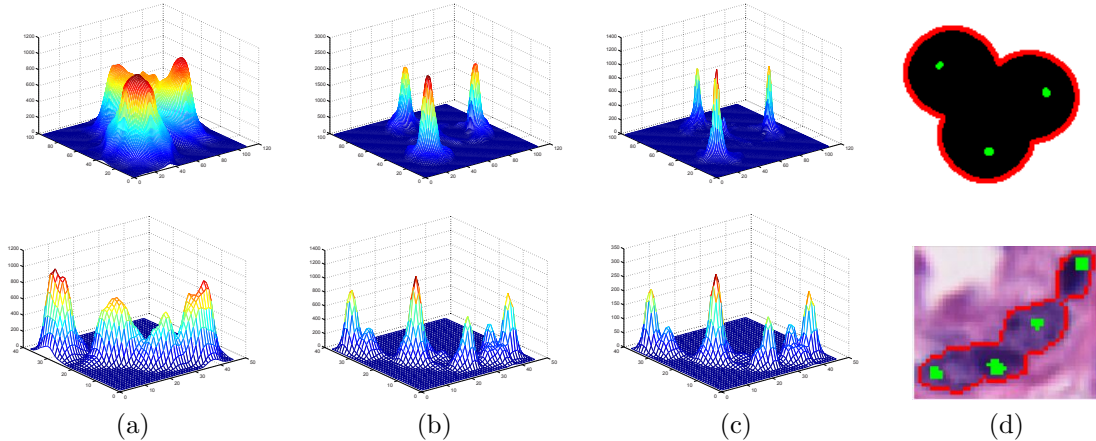


Figure 2.2: Intermediate results of the segmentation method by Hafiane et al. Evolution of the voting landscape $V(i, j)$ and the resulting centers for a synthetic image (top), and a nucleus cluster image (bottom). (a) iteration 1, (b) iteration 5, (c) iteration 10, (d) nucleus contours (red) and centers (green) superimposed on the original image (Images are reused from [48]. Permission of use can be found in Appendix A).

the symmetrical contribution of each pixel around an arbitrary pixel and therefore, centroids of circular regions are highlighted, which can be subsequently thresholded to find the seeds.

- An efficient machine learning approach was proposed by Vink et al. [21]. They constructed a large feature set and used a modified version of Adaboost which enables inclusion of the computational cost of each feature to create two detectors. The outputs of the two detectors are then merged by a globally optimal active contour algorithm to refine the border of the detected nuclei.
- A fast nucleus center localization approach proposed by Qi et al. [25][25] that utilizes single-path voting along the direction of the image gradient. It is used to both detect nuclei and also separate clumped nuclei.
- Hessian-based Laplacian of Gaussian (HLoG) using scale space theory as its foundation identifies the single optimal scale on which a pre-segmentation is conducted [98]. The

Hessian process is also able to delineate blobs and it's shown that it can outperform Radial basis symmetry and LoG-based detectors.

2.2 Nucleus Segmentation

The nucleus segmentation algorithms in the literature can be divided into six main categories as briefly discussed in previous chapter:

1. Intensity based approaches,
2. Region based approaches,
3. Level set methods,
4. Probabilistic models,
5. Graphical models, and
6. Machine learning approaches.

2.2.1 Intensity Based Approaches

Gurcan et al. [32] employed a morphological top-hat by reconstruction algorithm coupled with hysteresis thresholding [99] to both detect and segment the cell nuclei. Cell clumps were separated using a watershed transform.

Wienert et al. [33] used a contour tracing approach to first over-detect regions and then selected a set of non-overlapping regions from which some of the candidates were selected based on concavity and average intensity. Cong and Parvin [34] first binarized the image based on a threshold computed from an intensity histogram and used polygon approximation and employed a corner detector to find the corners with inward turning angles in cell clumps to separate nuclei. After finding the crease points, images were enhanced through a variation of nonlinear diffusion [100] to improve localization of crease points. Then hyperquadrics [101]

were fit to initial boundaries and crease points. Using prior knowledge about nuclei shapes, such as area and shape, hyperquadrics were evaluated and some were accepted as the cell regions.

2.2.2 Region Based Approaches

Kothari et al. [20] proposed a watershed segmentation to segment and count nuclei in fluorescently stained imagery of cervical and prostate carcinomas. Using the extended H-maxima, seeds were chosen for watershed segmentation in a way that each nucleus receives at least one seed. This led to an initial over-segmentation, i.e. a boundary was created where there is no strong edge. In another step, regions were merged based on the gradient magnitude along the boundary separating neighboring objects. Also, to separate clumped nuclei, they have used the 3–4 distance transform for 2D images [87] and the 3–4–5 distance transform for 3D images [102] to create a distance map and performed similar watershed segmentation and merging regions with weak boundaries steps as before, to separate nuclei inside clumps.

Veta et al. [22] proposed an automated nuclei segmentation method that works with H&E stained breast cancer histopathology which can be divided into four main steps: 1) pre-processing with color unmixing (Fig. 2.3b) and morphological operators (Fig. 2.3c), 2) marker-controlled watershed segmentation at multiple scales and with different markers, 3) post-processing for rejection of false regions and 4) merging of the results from multiple scales. They performed watershed segmentation with two sets of foreground and background markers: after employing fast radial symmetry transform (FRST) [97] (Fig. 2.3d) to localize nuclei, its foreground and skeleton of background (Fig. 2.3e) was used as the first set of markers for watershed segmentation (Fig. 2.3f) and regional minima foreground and background of the output of morphological operators (Fig. 2.3g) was used as the second set of markers (Fig. 2.3h).

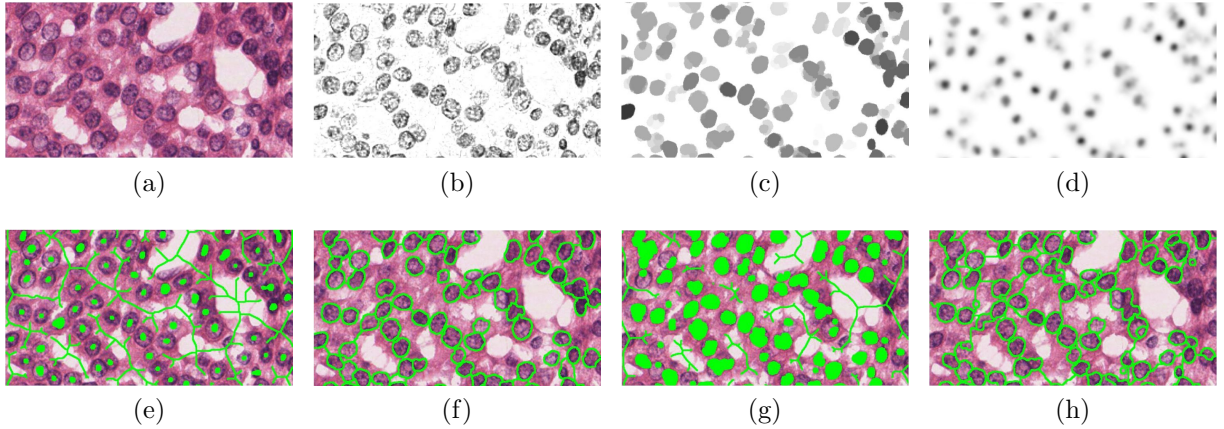


Figure 2.3: Intermediate results of the segmentation method by Veta et al. (a) Original image and (b–h) results of different steps of the algorithm in [22] (Images are reused from [31]. Permission of use can be found in Appendix A).

2.2.3 Level Set Methods

Cosatto et al. [84] employed a combination of difference of Gaussians and a Hough transform to detect candidate nuclei followed by active contour to perform segmentation. Li et al. [27] proposed a nucleus segmentation algorithm that is composed of three key steps: 1) generating a diffused gradient vector flow field [103], 2) performing a gradient flow tracking procedure to attract points to the basin of a sink, and 3) separating the image into small regions, each containing one nucleus and nearby peripheral background, and performing local adaptive thresholding in each small region to extract the cell nucleus from the background.

Fatakdawala et al. [26] used the output from a Gaussian mixture clustering algorithm to initialize a magnetostatic active contour (MAC) Model [104]. The MAC model implements a bidirectional force field F generated from a hypothetical magnetostatic interaction between the set of contours S and the object boundary and therefore, allowing the contour to grow or shrink towards object boundaries. Each MAC model may segment touching or overlapping nuclei and the algorithm separates clumped nuclei with a process in which contours segmenting nuclei clumps were split using a size heuristic and determining high concavity points. They finally used K-means clustering [105] of first-order statistical texture features

derived from within the object interior to classify the segmented regions as a lymphocyte or not.

2.2.4 Probabilistic Models

Veillard et al. [55] calculated a probability map from 180 features extracted from texture and scaled information in addition to simple pixel color intensities. The constructed map has a strong object-background contrast and smoothing out the irregularities within the nuclei and background. The probability map was then used for an active contour model with a nuclei shape prior for the actual segmentation.

Shenoy et al. [56] proposed a probabilistic approach to simultaneously classify and segment multiple cells of different classes in a multi-variate setting. Superpixels were extracted using the Simple Linear Iterative Clustering (SLIC) algorithm [106] from the input vector-valued image, and a 2D hidden Markov model (HMM) was set up on the superpixel graph. Instead of predicting the class label of each superpixel from its feature vector, information from adjacent superpixels was utilized using HMM emission probabilities to ensure high confidence in local class selection. Later, optimal superpixel-level class labels inferred using the HMM were aggregated to obtain global multiple object segmentation.

2.2.5 Graphical Models

Ta et al. [59] employed Voronoi diagrams to segment nuclei images in cytological and histological images and Chang et al. [58] proposed multi-reference graph cut (MRGC) based on color and Laplacian of Gaussian features and used heuristics to separate clustered nuclei, including curvature-based reasoning.

Bamford and Lovell [24] used Laplacian of Gaussian filtering with scale selection to detect nucleus seed points followed by local maximum clustering to form a rough initial segmentation. The refinement step in which nuclei in clumps were separated is done by

energy minimization using a graph cut algorithm known as α -expansions [64]. The refinement was formulated as an iterative binary labeling problem. At each iteration, one label was set to an integer α , and the rest of the labels were set to another value, denoted $\bar{\alpha}$, where $\bar{\alpha} \neq \alpha$. To make the algorithm more efficient on clumps with large numbers of nuclei (seed points) in them, they used graph coloring to color each seed point with a color different than its two-level adjacent neighbors. Then, at each iteration all the labels with the same color were set to α and all other labels were set to $\bar{\alpha}$. This made the algorithm more efficient by expanding several seed points concurrently.

Poulain et al. [60] used two relatively basic techniques of markers controlled, watershed [107] (or Skeleton by Influence Zones) with two sets of seeds and Fast Marching (FM) [108] (a curve evolution based approach) to construct a dictionary of shapes. Basically, the dictionary can be constructed using different segmentation algorithms or from the same segmentation algorithms with different parameters. In the next main step, the energy function defined to select the best candidates of shapes obtained from different segmentation maps was minimized using an iterative graph cut algorithm [109]. They showed that this process allows drastic improvement in the performance of each individual segmentation.

2.2.6 Machine Learning Approaches

Su et al. [72] proposed an ROI segmentation scheme using a fast scanning deep convolutional neural network (fCNN) [110] and used it for region segmentation in histopathological breast cancer images. Santamaria-Pang et al. [73] proposed a supervised machine learning method to enhance and improve more general segmentation methods by utilizing hierarchical shape ranking that uses a shape distance measure. Zhou et al. [75] used raw image patches and their corresponding annotated binary masks to jointly learn a bank of convolutional filters and a sparse linear regressor. They are used for feature extraction and building a likelihood map which includes the likelihood of each pixel belonging to a nuclear region or

background. Pixels were then labeled simply by thresholding the likelihood map. Kong et al. [69] extracted color-texture at the local neighborhood of each pixel by a local Fourier transform (LFT) from a new color space and used it, instead of pixel color intensities, to classify each pixel into either the cell or extra-cellular category. The used color space is called the most discriminant color space (MDC) and was learned by maximizing the classification performance.

Jung et al. [68] binarized the image after preprocessing steps and used a distance transform to generate a topographic surface. The surface was then modeled as a mixture of Gaussians and clusters were formed. By using a *separation* and *compactness* measure, they defined a *cluster validity index* based on a hypothetical number of nuclei. The number of regional maximas in each cluster gives an upper bound for the number of its overlapped nuclei and therefore, it was used as the initial number of nuclei. In an iterative fashion, this number was decreased and the number of nuclei giving the highest cluster validity index was selected. Then, separation lines between nuclei were found with a minimum-error-rate classification scheme based on Bayesian classification. Later, the occluded contours were reconstructed based on the fact that nuclei generally have ellipse-like shaped contours.

Su et al. [74] proposed an interactive semi-supervised segmentation method by classifying feature-homogeneous superpixels into specific classes, guided by human intervention. It consists of four main steps: 1) superpixel generation by clustering neighboring pixels, 2) active annotation by drawing samples that minimizes the expected prediction error, 3) superpixel classification by propagating labels over the affinity graph and 4) active verification to fix misclassifications. After clustering pixels into superpixels, the most informative superpixels were selected for human annotation. An affinity graph was constructed that characterizes the pairwise similarity between the superpixels and the superpixels were classified into specified classes by propagating the human specified-labels to the unlabeled superpixels. At each point, if the segmentation is not reliable, the algorithm selects a batch of error-prone super-

pixels to query for verification. The new information was systematically propagated over an augmented affinity graph to the unlabeled superpixels. This procedure was repeated until most superpixels were classified into a specific category with high confidence. The approach minimizes human effort by the early use of manual annotation/verification.

2.3 Cervical Cytology

In this Section I review some of the methods in the literature [51, 52, 42, 43, 53, 36, 111, 112, 113, 114, 115, 116, 117, 118, 119, 120, 121, 122, 123, 124, 125] proposed specifically for cervical cytology image segmentation.

Complete segmentation of cervical cells in Pap (or H&E) stained cervical cytology images is a difficult task for several reasons: 1) folded cervical cells with spurious edges, 2) poor contrast of cytoplasm boundaries, 3) presence of bacteria, neutrophils, mucus, blood and inflammatory cells, 4) cervical cells overlapping. Another issue is that although newer preparation techniques (ThinPrep, SurePath, etc.) make very thin slides compared to traditional techniques, remove most of the mucus and inflammatory cells and decrease the number of overlapping cells, they still can range upwards of 30 μ m from glass to coverslip [126] and therefore it is impossible to have all cervical cells in-focus simultaneously in a single focal plane. However, extended depth of field (EDF) algorithms are proposed [127, 128] to create a single image from a stack of images with different focal depth in a way that all objects in the image are in-focus at the same time.

Most of the work on cervical cytology segmentation was done in the last decade and only during the past couple years has the overlapping cervical cell segmentation in real cervical cytology images been addressed [51, 52, 53, 35, 36]. However, there are a few other earlier works which segment *touching* cells [117, 122].

To discuss the segmentation methods for cervical cytology images in the literature I suggest to first divide them into three categories and discuss them separately:

1. Nucleus segmentation,
2. Free-lying cell segmentation and
3. Overlapping cell segmentation.

2.3.1 Nucleus Segmentation

Nucleus segmentation [68, 45, 42, 43, 111, 114, 116, 119, 121, 123, 124, 125] is the most studied category of method for cervical cell segmentation. Most of these methods ignore cytoplasm segmentation, while a few other works [42, 43, 111, 120] segment the whole cytoplasm area too. Although this is not as useful as segmenting cytoplasms of each nucleus separately, which is a much more difficult task addressed mostly by the methods in the third category, such methods can be used to segment both the nucleus and corresponding cytoplasm in images containing free-lying cells.

Some of the nucleus detectors described in Section 2.1, like [90], are used for nucleus segmentation in cervical cytology images [51]. Wu et al. [123] first approximated the image with a parametric image by iteratively minimizing a defined cost function and then obtained the segmentation by simply segmenting the parametric image at its threshold parameter. Plissiti et al. [111] over-detected nuclei by morphological analysis and then refined them by incorporating a priori knowledge about the circumference of each nucleus. Later, classifiers were used to reduce the false positive rate. In a similar approach, Plissiti et al. [116] detected nuclei by the morphological image reconstruction process and their boundaries were delineated from the morphological color gradient image with the watershed transform using the nuclei markers extracted in the detection step. Classification was later carried out to reduce the false positive rate. Plissiti and Nikou [119] used a level set method to segment cells in images containing two overlapping nuclei. Zhang et al. [120] proposed a graph cut approach to segment overlapping nuclei and also cell clumps. Overlapping nuclei were then separated by two concave points-based approaches.

Bergmeir et al. [114] proposed a more complicated approach in which the Canny edge detector [129] was used to extract edges from the image after noise-removal and smoothing by mean-shift and median filtering. Edges close to the background were removed and a randomized Hough Transform was used to find ellipses. If an ellipse was reliable enough, an active contour was initialized around a circle centered at the ellipse center to fit to the boundary of the region. The region segmentation was accepted if its difference from the ellipse is above a threshold.

Gençtav et al. [42] proposed a watershed based segmentation approach to segment and classify overlapping nuclei. The method first extracts cell clumps in the image by converting the image to CIE Lab color space and processing the L channel. By using a hierarchical watershed-based segmentation, cell clumps were separated into smaller regions. Based on different segmentations at various scales and by using a classifier, regions were classified as a nucleus or cytoplasm region and they were finally merged to obtain the final segmentation of overlapping nuclei and cytoplasm area. They used their method to segment nuclei and their corresponding cytoplasm in a dataset of images containing free-lying cervical cells with different degrees of abnormality.

2.3.2 Free-lying Cell Segmentation

Free-lying cell segmentation methods [112, 113, 115, 117, 118, 122] aim to segment both the nucleus and its cytoplasm inside images containing free-lying cells. While most of these methods [112, 113, 115, 118] work only on free-lying cells, a few other approaches also try to separate touching cells [117] in an extra step.

Yang-Mao et al. [113] proposed an edge enhancement nucleus and cytoplasm contour which consists of five steps: 1) noise-removal with a *trim-meaning* filter while preserving the sharpness of object boundaries, 2) a bigroup approach to isolate the object contour pixels from background, 3) gradient computing using the Sobel operator, 4) edge enhancement

with the mean vector difference (MVD) enhancer and 5) contour extraction by thresholding the gradient map.

Béliz-Osorio et al. [122] used a locally constrained watershed transform to segment cervical cells, and Harandi et al. [117] used geometric active contours to segment cells and proposed an automatic circular decomposition method to separate touching cells. Pai et al. [115] used an adaptable threshold decision method [130] to delineate cytoplasm boundary. Then, they used a new method called the maximal gray-level-gradient-difference method which iteratively extends the cells contour inwards to maximize the difference of the average gray-levels of cytoplasm and nucleus.

Li et al. [118] proposed and used a variant of gradient vector flow (GVF), called radiating GVF snake, to detect nuclei and cytoplasm boundaries in which the edge map is computed in the direction of radials originated at the intensity-weighted centroid of the nucleus of the segmented cell.

2.3.3 Overlapping Cell Segmentation

The most difficult tasks for cervical cytology segmentation are to detect and segment nuclei and also their corresponding cytoplasm in real Pap smear images [51, 52, 53, 35, 36]. This can ideally lead to a fully automated system, which can segment images and extract features to diagnose cervical disease and its extent based on TBS. All works in this area are relatively recent. One of the first main works on this topic was done by Lu et al. [52]. Subsequently, two challenges and the datasets provided in the International Symposium on Biomedical Engineering (ISBI) 2014 and 2015, encouraged more work on this topic [53, 35, 36].

Lu et al. [51] used a level set method as the primary tool to segment overlapping cells. Their approach consists of three main steps: 1) cell clump segmentation, 2) nucleus detection

and segmentation, 3) overlapping cytoplasm segmentation, each of which are described briefly in the following.

- To segment the cell clump, the image was preprocessed with the quick shift algorithm [131] and then a map of superpixels was constructed by finding local maxima of a density function (Fig. 2.4b). Each superpixel was assigned a value in $[0, 1]$ as the mode of its pixel intensities and using an edge detector, superpixel edges were found (Fig. 2.4c). The convex hull of detected edges was computed and major parts of background separated (Fig. 2.4d). Finally, for each convex hull, by maximum likelihood estimation (MLE) a GMM was learned and used to classify its pixels as cell clump or background (Fig. 2.4e).
- Nuclei candidates were found by the MSER algorithm and some of them were rejected based on their features, such as eccentricity, area, mean intensity, and the area ratio between the blob and the cell clump to which it belongs (Fig. 2.4f).
- The main step is to segment overlapping cytoplasm. In this step, to each nucleus, a cytoplasm area was assigned using a level set method. A shape prior [132] was built for the level set with two types of attractors (the estimated boundaries of the clumps and individual cells) and two types of repellents (the background and the nuclei) and an initial segmentation was created in several steps, such as assigning boundary pixels to the closest nucleus, etc. For each of the N nuclei detected in a cell clump, a level set function (LSF) was initialized at the geometric center of each initial segmented cell with the computed shape prior and the energy functional to be minimized was defined as

$$\varepsilon(\{\phi_i\}_{i=1}^N) = \sum_{i=1}^N \varepsilon_u(\phi_i) + \sum_{i=1}^N \sum_{j \in \mathcal{N}(i)} \varepsilon_b(\phi_i, \phi_j), \quad (2.3)$$

where $\{\phi_i\}_{i=1}^N$ is the set of LSF's, $\varepsilon_u(\cdot)$ is the unary energy functional defined for each LSF, $\varepsilon_b(\cdot, \cdot)$ is the binary function defined over pairs of LSF's, and $\mathcal{N}(i)$ represents the

level set functions ϕ_j such that their zero level set intersects the zero level set of ϕ_i (Fig. 2.4g).

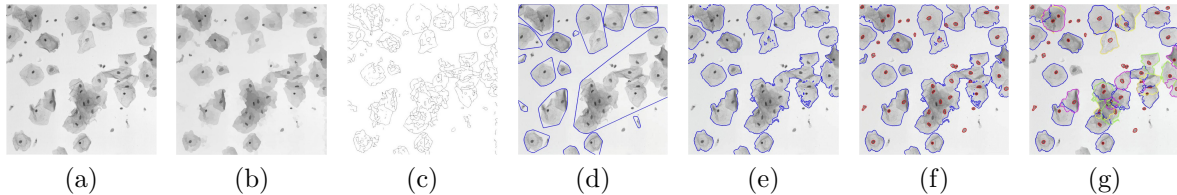


Figure 2.4: Intermediate results of the improved joint optimization algorithm by Lu et al. (a) Original image and (b–g) results of different steps of the algorithm in [51] (Images are reused from [51]. Permission of use can be found in Appendix A).

Ushizima et al. [35] used bilateral filtering [133], contrast limited adaptive histogram equalization [134] and statistical region merging [135] to segment cell clumps. Inside each of the clumps, they used a local thresholding method [136] to segment nuclei. Then the cytoplasm area was segmented by simply calculating Voronoi diagrams. The segmentation results in non-overlapping cytoplasm. As their next improvement, in [36], they used morphological reconstruction combined with optimization methods to determine the minimum enclosing ellipse from the stack of cervical cytology images at different focal planes, which is able to give overlapping cytoplasm segmentations.

Nosrati and Hamarneh [53] also used a level set method which uses a star-shape prior first introduced by Veksler [137]. To find the nuclei, similar to Ushizima et al. [35], they used bilateral filtering [133] and a local thresholding method [136] to detect the initial candidates. Then using histogram of oriented gradient (HOG) [138] features and a random forests (RF) classifier candidate regions were classified as nucleus or other objects. They reported that their algorithm achieved superior results in comparison to [52].

Chapter 3

Hierarchical Multilevel Thresholding for Nucleus Segmentation in Histology Images

Part of this chapter was published in the 2016 SPIE Medical Imaging Symposium on Digital Pathology [139].

3.1 Introduction

Automatic segmentation of histological images is an important step for increasing throughput while maintaining high accuracy, avoiding variation from subjective bias, and reducing the costs for diagnosing human illnesses such as cancer and Alzheimer’s disease. In this chapter, a novel method for unsupervised segmentation of cell nuclei in stained histology tissue is presented. Cellular features such as nuclear size, distribution and texture play an important role in diagnosis and grading of diseases from histology tissue. To automatically quantify features of microscopic nuclei in images of stained tissue, nuclei locations and boundaries must first be located. Nucleus detection and segmentation has been addressed with a variety of algorithms, including Gaussian mixture clustering [140], gradient flow tracking [141], watershed [22] and graph cuts [67]. Color normalization and color deconvolution can be used to take advantage of color information from different stains to enhance results of nuclear segmentation [18]. However, a general approach has been elusive because nuclei can be clustered and exhibit a range of shapes, sizes, and colors depending on staining method and tissue type [1]. Therefore, a general algorithm for segmenting nuclei stained with hematoxylin and eosin (H&E) is proposed and the performance is evaluated using a dataset of biopsy images

from various tissues. The proposed method requires no parameter learning or training data because the parameter values are set adaptively, making the approach insensitive to intensity variations. The Matlab code of the proposed method is made available publicly to enable further research and benchmarking ¹.

3.2 Method

The dataset used to evaluate the proposed method was provided by Wienert et al. [33], and is discussed in the following.

3.2.1 Overview of the Method

Steps of the method are divided into two main parts: preprocessing and segmentation. The preprocessing step consists of color deconvolution and image reconstruction. Segmentation is based on binarization of the image from a threshold obtained from a multilevel thresholding algorithm. The resulting segmentation divides “large” regions into smaller regions followed by morphological operations to separate close regions and smooth out the boundaries. The flow of the approach is presented in Fig. 3.1.

3.2.2 Preprocessing

The preprocessing step includes color deconvolution [16] by modeling the image colors based on the Beer-Lambert Law. Since hematoxylin stains nucleic acids in the cell nucleus, the hematoxylin channel was used for nuclear segmentation. The resulting grayscale image was then processed with opening by reconstruction to connect close background regions to each other.

The morphological process of closing by reconstruction is a common process after opening by reconstruction. Due to the low resolution of images, closing by reconstruction connects

¹http://www.csee.usf.edu/~hady/codes/2016SPIE_histology_segmentation.zip.

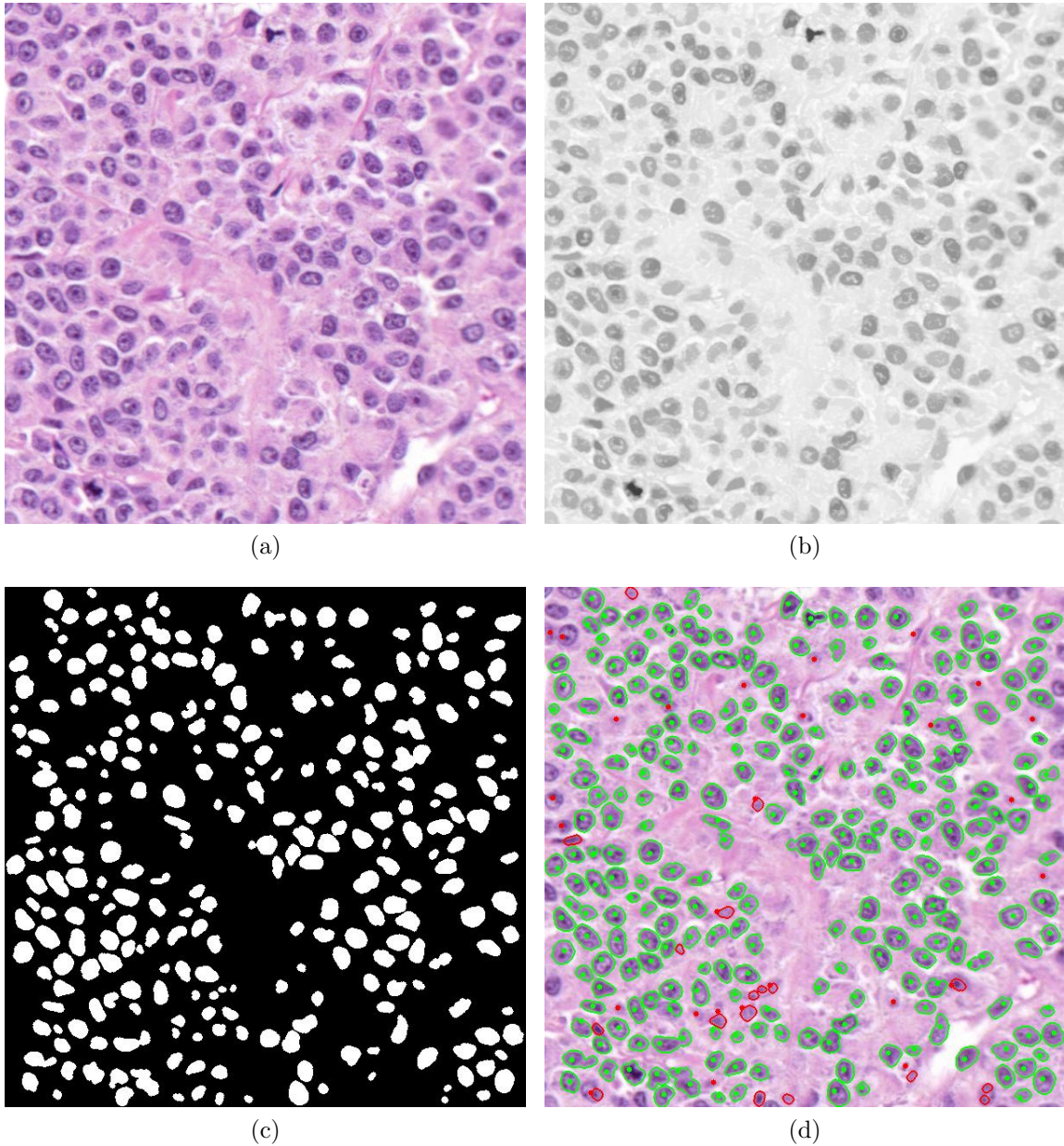


Figure 3.1: Flow of the hierarchical multilevel thresholding approach. (a) Original image, (b) Hematoxylin channel after color deconvolution, and Opening by reconstruction on hematoxylin channel, (d) Iterative binarizations followed by morphological operations, region splitting and removing boundary regions, (f) The contours on the original image - green dots, red dots and red contours are true positives, false negatives and false positives respectively.

some adjacent nuclei to each other and therefore segments them as a single nucleus. The processed image was then ready for segmentation.

3.2.3 Automated Threshold Selection

The next step was to iteratively binarize the preprocessed grayscale image and form the regions as nuclei. Selection of thresholds for this step was done using 1 through 10-level (multilevel) thresholding based on the Otsu method [88], as described by Liao et al. [142]. Each of these multilevel thresholdings divides the pixel intensities to $(\text{level} + 1)$ classes with minimal combined intra-class variance and equivalently maximal inter-class variance [88]. I retained the lowest thresholds of each multilevel thresholding, a total of up to 10 different thresholds that specified the darkest class in the image in each corresponding multilevel thresholding. After a descending sort on this set of thresholds, the image was binarized from the highest threshold. The first formed regions were considered as initial regions and each subsequent binarization produces a subset of (usually smaller) regions from a previous binarization. This process may cause division of some regions into two or more regions; in this case, the new (smaller) regions replaced the larger region. If a region was simply shrunk in a new binarization, however, that region was not replaced. Each initial region may therefore be replaced later only if it split into two or more regions.

After each binarization, an opening operation was performed to separate weakly connected regions. Holes in the regions were filled to reconstruct the regions with holes mostly obtained from cancer cells. Regions smaller than a predefined size, m , were removed to eliminate the segmented of tissue artifacts. Finally, regions connected to the boundary of an image were removed.

Because of the preprocessing step, segmented region boundaries were usually formed inside the nuclei area. Therefore, the final nuclei outlines were obtained by dilating the final

regions with a disk of radius one pixel, giving a more visually accurate approximation of the boundaries.

3.3 Dataset

The limited number of public datasets for histopathology analysis increases the difficulty of comparing different methods. This dataset includes a wide variety of tissues such as breast cancer samples representing a broad morphological variety, including normal tissue components; bone marrow with normal and pathologically altered cells; normal liver tissue; kidney tissue; and intestinal mucosa [33]. The dataset consists of thirty-six histology images (600x600 pixels each) with ground truth. The dataset includes a total of 7931 consistently labeled cells by consensus agreement of three pathologists.

3.4 Results

The single parameter in the method, m , specifies the size of the smallest permitted region. In the present study, m is set to 50 pixels as in the study by Wienert et al. [33] that provided the images. The structuring elements for opening by reconstruction and opening to separate weakly connected regions are set to a disk with radius three pixels based on the image size. Choosing a disk with radius two or four pixels affects the results by about one percent. The goal in selecting structuring elements with radius three pixels is to avoid: 1) a too large structuring element that removes important detail in the image; and 2) a too small structuring element that fails to connect close background parts to each other, which could degrade the results more than a couple percent. Increasing the number of levels when choosing the thresholds changes the computation time but does not significantly change the results.

True positive (TP) is defined as the number of manual points in ground truth that fall inside the segmented nuclei. False positive (FP) is the number of segmented nuclei that

include no manual points. False negative (FN) is the number of manual labeled points that do not fall into any segmented nucleus. The results are presented in terms of precision, recall, F-measure and conglomerate, which are described in the following.

Precision, recall and F-measure are computed as below:

$$\text{Precision} = \frac{\text{TP}}{\text{TP} + \text{FP}}, \text{ Recall} = \frac{\text{TP}}{\text{TP} + \text{FN}} \text{ and F-measure} = 2 \cdot \frac{\text{Precision} \cdot \text{Recall}}{\text{Precision} + \text{Recall}}.$$

Lastly, conglomerate is defined as

$$\text{Conglomerate} = \frac{N - \text{FP}}{\text{TP}},$$

where N is the number of segmented regions.

For comparison, I include the results of the proposed method along with four other sets of results. The first two sets of results are from a method [67] proposed by Al Kofahi et al., with two versions of “automatic” and “optimized”, which uses nine parameters. The other two sets of results are from methods proposed by Wienert et al. [33], which use five parameters and Veta et al. [22], which uses a fixed set of structuring elements and three parameters which need to be trained and are mainly used to select the best candidates for the final contours. A summary of the results is presented in Table 3.1².

Table 3.1: Results summary - superior results are shown with bold font.

	Precision	Recall	F-measure	Conglomerate
Al Kofahi (automatic) [67]	0.717	0.908	0.801	0.964
Al Kofahi (optimized)	0.823	0.908	0.863	0.966
Wienert [33]	0.908	0.859	0.883	0.958
Veta [22]	0.904	0.833	0.867	0.989
Proposed Method	0.929	0.886	0.907	0.952

²The results of the method proposed by Al Kofahi et al. are taken from Ref. 33. Also, the F-measure values are computed based on the corresponding precision and recall.

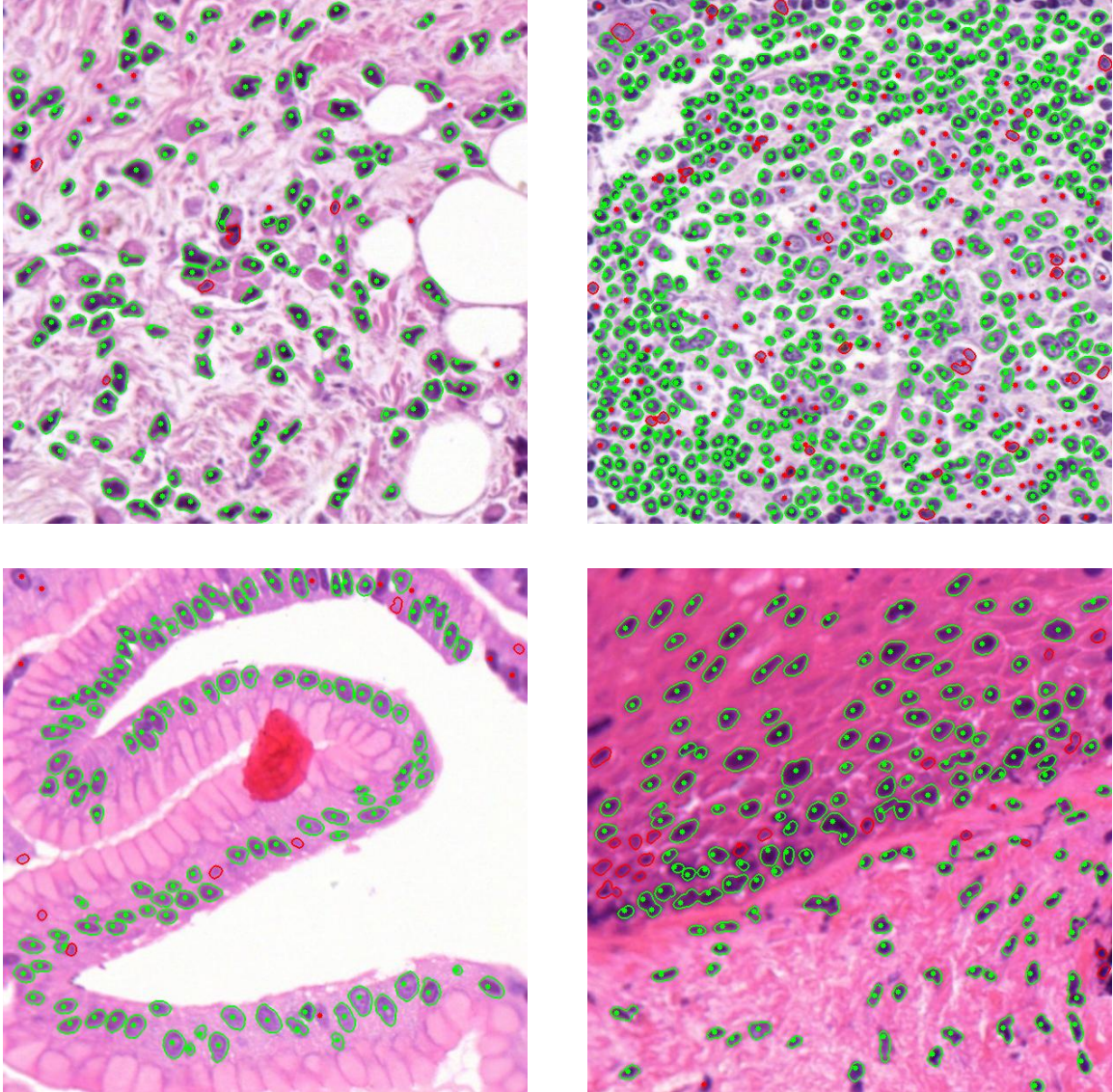


Figure 3.2: Segmentation results of four images in dataset. Green dots, red dots and red contours are true positives, false negatives and false positives respectively.

3.5 Discussion

The proposed method achieves the highest precision measure and its recall measure is very near the highest value among all methods. Hence, the proposed approach has the highest F-measure. The conglomerate measure is the lowest but comparable to first three methods.

Thus, the proposed method tends to segment overlapped (or touching) nuclei to a greater extent than the other methods. This result is expected since the regions are segmented by multilevel thresholding and, in this process, miss a low intensity difference between two close nuclei. The under-segmentation of the overlapped nuclei can be potentially handled by an additional post-processing step. For example, because a region that is segmenting overlapped nuclei usually has a low solidity (ratio of the region's area to the area of its convex hull), to improve the conglomerate score in post-processing all segmented regions with solidity less than 0.8 can be simply removed. With this step, the approach achieves a precision, recall, F-measure and conglomerate of 0.930, 0.860, 0.894 and 0.959, respectively. However, to achieve a high conglomerate measure as with the method proposed by Veta et al., and at the same time keep a good value of precision and recall, a more advanced post-processing step is required.

The algorithm is insensitive to minor parameter changes as evidenced by only a few percent changes in the results by modifications such as performing closing by reconstruction after opening by reconstruction in preprocessing; imposing a largest region's area limit during binarization; increasing the minimum permitted region's area; and using morphological features such as solidity and boundary saliency to reject some regions.

In terms of speed, the whole process, including color deconvolution, preprocessing, segmentation and computing different measures takes on average about one second (1.02 s) for each image on a PC with a 2.4 GHz CPU.

Four examples of segmentation results of different tissues are presented in Fig. 3.2.

3.6 Summary

An algorithm is proposed to segment nuclei in histology images stained with H&E, a general stain in pathology for evaluating a wide range of normal and diseased tissue. Using color deconvolution, image reconstructions, iterative multilevel thresholding and morpho-

logical operations, the approach segments nuclei in a wide variety of histology images from various tissue types. The algorithm requires a single parameter for specifying the smallest permitted region area during the process of removing regions. The results show high precision and recall on a dataset including normal and cancerous tissues of different types, and superior performance in terms of F-measure (with precision 0.929 and recall 0.886) as compared to other reported results on the same dataset. For future work, post-processing steps can be designed to separate clumped nuclei and refine the boundaries. Since many missed manual points lie very close to the boundaries of segmented regions and clumped nuclei, these can be effectively found by checking features such as solidity of the segmented regions. These additional steps can potentially increase the conglomerate measure while improving precision and recall measures.

Chapter 4

Cervical Tissue Segmentation and Classification Using an Ensemble Approach

Parts of this chapter were published in the proceedings of 2013 International Conference on Image Analysis and Processing [143] and 2014 IEEE International Conference on Systems, Man, and Cybernetics [144]. Permissions of use are included in Appendix A.

4.1 Introduction

Current manual approaches for cancer detection rely on experts. This approach suffers from expert's fatigue and poor inter-rater reliability. Hence, it increases the importance of having a highly accurate automated classification method.

Usually, to classify cells within a tissue sample from a patient into normal and cancer classes one first needs to segment tissue images. There has been a fair amount of work on segmentation of cervical cytology images [51, 43, 36, 111, 113, 117, 120, 125], but segmentation of cervical histology images, done here, is less studied. Fig. 4.1 shows how cytology images can be different from histology images. One the other hand, one of the important extractable features that discriminates between normal and cervical cancer cells is their Mean Nuclear Volume (MNV) [145, 146]. Normal tissues have only normal cells in their biopsy images but cancer tissues can contain both normal and cancer cells. This causes the MNV extracted from biopsy images of a normal tissue sample to be less than that extracted from biopsy images of a cancer tissue sample. In this work, I assumed that normal and cancer tissues can be separated linearly using their corresponding MNV, and instead of using a single segmentation algorithm, I used an ensemble approach. Such approaches have recently

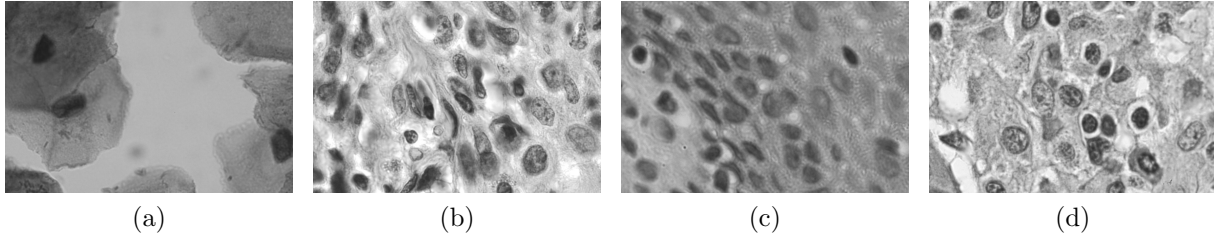


Figure 4.1: Samples of cervical cytology and histology images. (a) A sample cytology image and (b-d) samples of histology images.

been used widely for segmentation [147, 148, 149, 150]. Ensemble approaches use many different models to obtain higher performance than any individual. Some ensemble approaches use several weak classifiers to form a new classifier which performs better than each of the original classifiers. In these approaches the original classifiers use some fixed parameters which are set by the user. Examples of such approaches can be seen in [143, 151, 152, 153]. However, there exist some other ensemble approaches that aim to find the best suitable set of parameters for each particular case [154, 155]. The method that is proposed in this chapter uses a case based approach. The proposed method uses 72 classifiers which makes it a *large* ensemble approach in comparison to most of the other ensemble approaches in the field of image processing that mostly use only a few classifiers [152, 154, 147]. However, data mining ensemble approaches usually use larger numbers of classifiers [156, 157].

One of the advantages of this approach to the one previously published by the authors [143] is that it does not include the *manual screening* step in which the images of each case were visually examined and the case was discarded if the majority of the images had poor acquisition quality, a large number of overlapped cells, high variation in background intensity, etc. In [143] an ensemble approach was used in a way that a single segmentation was formed from three other segmentations (out of four segmentations). However, here, a new ensemble approach is proposed that uses a large number of individual segmentors. By using different combinations of parameter values, I generated several sets of four segmentations as discussed in Section 4.2 and instead of making a new final ensemble segmentation, I kept one

segmentation out of each set of four segmentations. The median of the extracted features from the final segmentations was then used for classification. During the segmentation and before feature extraction, cases which were labeled as *bad* cases by criteria discussed in 4.2.4 were automatically removed. It enabled using this method without any manual screening. Finally, it will be shown that the final feature acquired by this method can effectively distinguish between the two normal and cancer cases. An overview of the algorithm can be seen in Fig. 4.2.

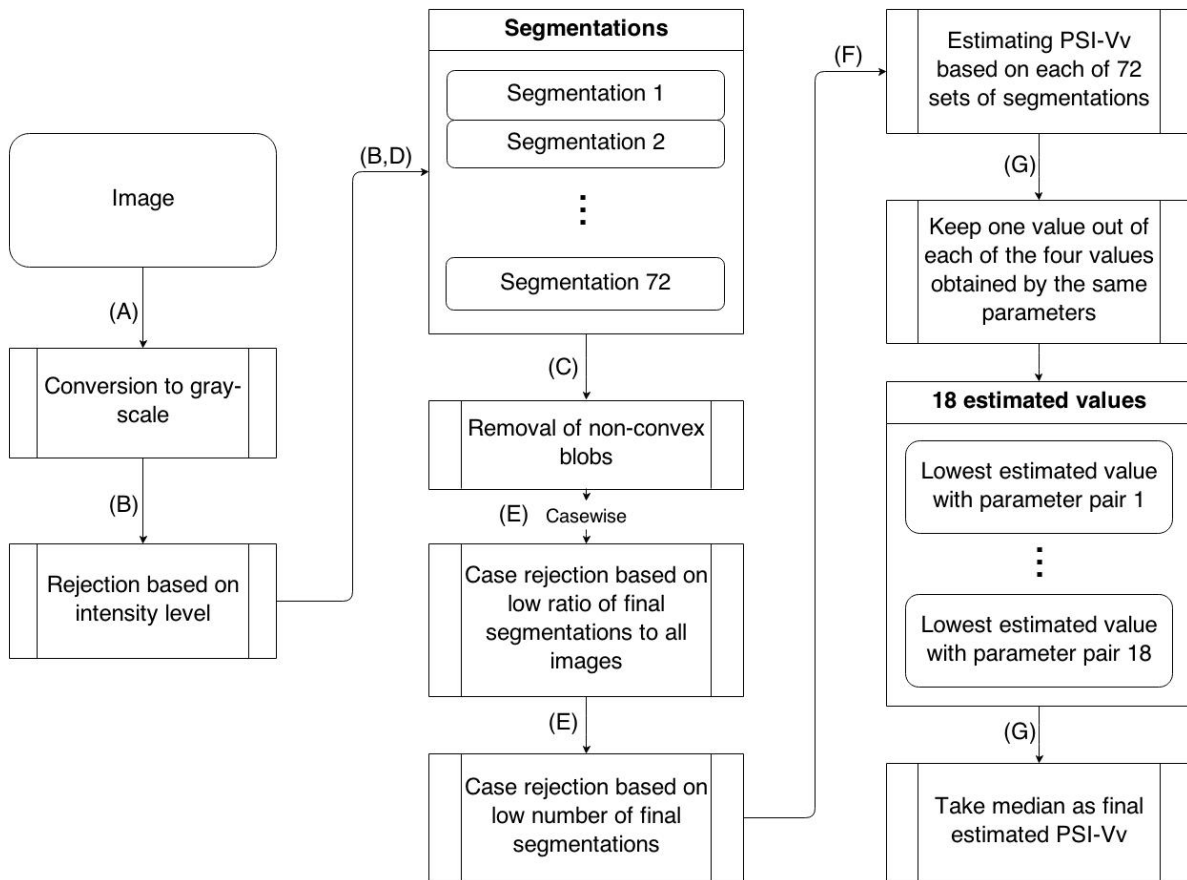


Figure 4.2: Overview of the algorithm.

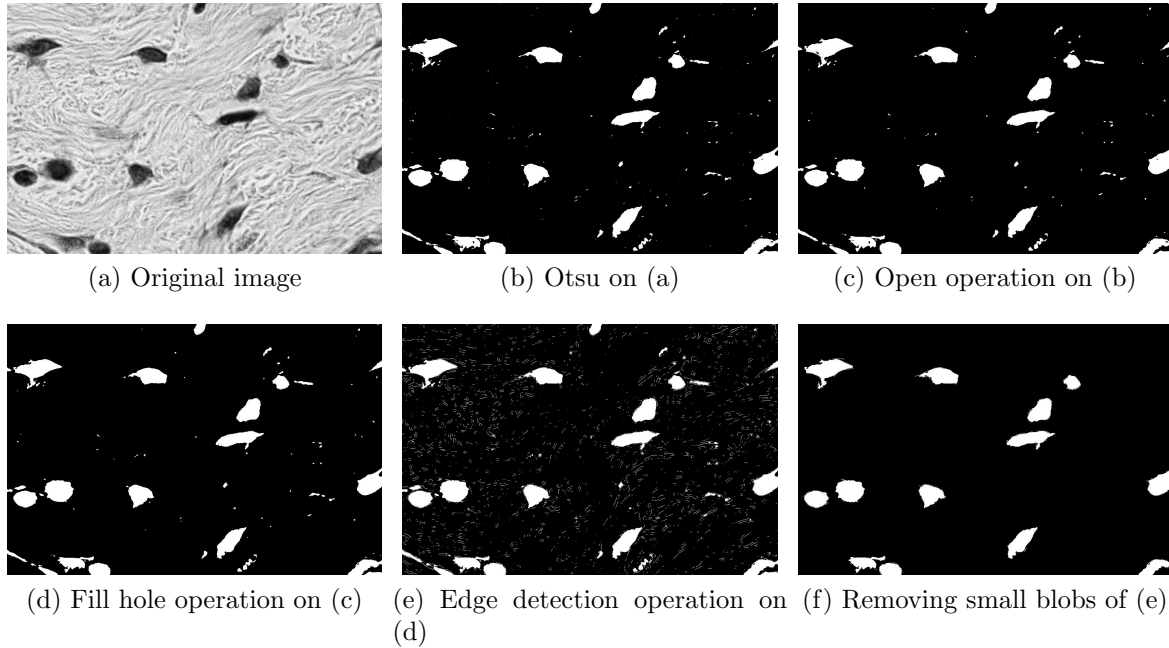


Figure 4.3: Results of Segmentor 3. Apply Segmentor 3 with parameters 4000 and 40000, as *MinBlobSize* and *MaxBlobSize* respectively, on a gray-scale image step by step and removing small blobs in the end.

4.2 Methods

The images were first converted to grayscale images using the Karhunen-Loeve transform [158].

4.2.1 Basic Segmentors

If the average intensity of the gray-scale image is higher than a threshold (250 in this study) the whole image was removed. For all other images, four segmentations were produced by each of the following segmentors.

- Segmentor 1: This segmentor starts with a three class Otsu [88]. The class with the highest intensity mainly represents the pixel values in region(s) of cell nuclei and therefore was kept. Then morphological operations, opening, and filling hole were applied.

- Segmentor 2: It starts with a three class Otsu. At the first step, the pixels with intensities in the class containing the lowest intensity were removed. After that, Segmentor 1 was applied to the new image (three class Otsu followed by morphological operations). This segmentor is expected to do better on cancer cells that commonly have some part of the cell nuclei segmented as background in a previous segmentor. This segmentor gives those parts of the cell nuclei another chance to be correctly segmented as foreground.
- Segmentor 3: Euchromatin in cancer cells makes the middle of the cells less dark. This is not the case for normal cells where heterochromatin causes a rather uniform intensity throughout the nucleus. As a workaround to this issue Segmentor 3, performs an edge detection operation on the segmentation obtained from Segmentor 1 which does a three class Otsu followed by morphological operations, open and fill hole. The added edge pixels cause the boundary to be closed at some very near points or even two separated parts of a specific nucleus to be merged and form a single nucleus.
- Segmentor 4: This segmentor starts with a three class Otsu which takes the darkest class as the region of interest and unlike Segmentor 3 (which performed the edge detection morphological operation as the final operation), it performs the edge detection morphological operation on the result of the three class Otsu and follows it with morphological operations, edge detection, dilation and fill hole.

After creating the different segmentations, new segmentations were generated based on the size of blobs within the segmentation. Also, blobs which smaller than a predetermined threshold, *MinBlobSize*, were removed. These small blobs can be noise or very small nuclei in the segmentation. Also, if a blob within a specific segmentation was larger than a threshold, *MaxBlobSize*, the whole set of (four) segmentations was rejected. By these two checks

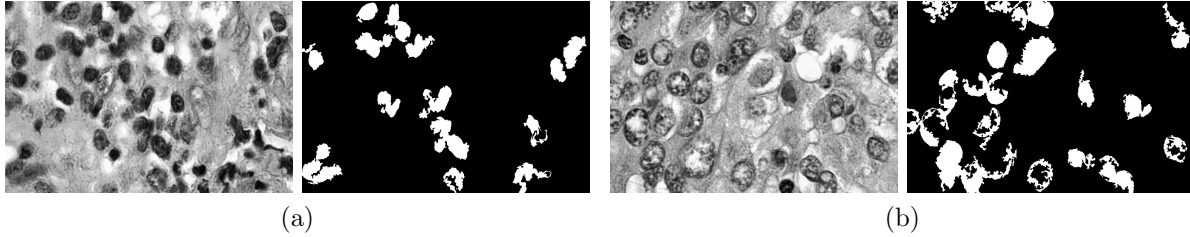


Figure 4.4: Sample results of final segmentation. (a) Two samples of segmentations including segmented clustered nuclei and (b) nuclei with nonuniform intensity.

the chance of noise and clustered nuclei being considered as a nucleus is reduced. Finally segmentations which contain no blobs are removed.

Fig. 4.3 shows an example of Segmentor 3 with parameters 4000 and 40000, respectively as *MinBlobSize* and *MaxBlobSize*, and the removal of small blobs done on a gray-scale image.

4.2.2 Non-Convex Blobs

There are several reasons that a nucleus might be segmented incorrectly. One of the reasons is the presence of clustered nuclei. These nuclei were usually segmented with each other. If the original nuclei were small, then the clustered nuclei could pass the maximum size check and therefore, it was increasing the estimated nuclear volume of normal cases. Also, some nuclei may not have uniformly high intensity on the boundary. This problem often occurs for cancer cells. It makes the nucleus segmentation difficult with the segmented blob missing parts of the nucleus. However, both of these (clustered nuclei and nuclei with non-uniform boundary) usually lead to a non-convex segmented blob (Fig. 4.4).

Because of the fact that nuclei have convex shapes with round boundaries in most cases, each blob was compared to its convex hull and if the absolute difference between the size of a nucleus and its convex hull was more than half of the original size, that blob was removed. This process removed several blobs from the segmentation in Fig. 4.4 that had non-convex shapes.

4.2.3 Parameter Space

In [143], it was shown that instead of using an individual segmentation, a generated ensemble segmentation from the four segmentors described above (with parameters (4000, 40000) and *SimilarityThreshold* of 55) could increase the separability between the two classes. Here, instead of creating a single segmentation from four segmentations, by changing the parameters, *MinBlobSize* and *MaxBlobSize*, several sets of four segmentations were generated. Generally, if m different values for *MinBlobSize* and n different values for *MaxBlobSize* are generated, there will be mn different pairs of parameters and $4mn$ segmentations will be generated. In this study, segmentations with $m = 3$ and $n = 6$ different values of *MinBlobSize* and *MaxBlobSize*, respectively, were generated as below.

Set

$$\textit{MinBlobSize} \in \{4000, 5000, 6000\},$$

and

$$\textit{MaxBlobSize} \in \{25000, 31000, 37000, 43000, 49000, 55000\}.$$

This gave us 18 different pairs of (*MinBlobSize*, *MaxBlobSize*). For each pair of parameters, four segmentations of each image were obtained and therefore, $4 \times 18 = 72$ different segmentations of each image were generated.

After obtaining the segmentation of all images of a case, the MNV (PSI-V_v) of cell nuclei within the segmentations of all images of each case was estimated. In fact, by decreasing *MinBlobSize* more small blobs are allowed to be in the segmentation and thus the final estimated MNV will be decreased. Similarly, when *MaxBlobSize* is decreased, more large nuclei will be removed, which in turn decreases the final estimated value. The process of nuclear volume estimation is discussed in Subsection 4.2.5. The classification was done based on the assumption that the MNV of cancer cells is larger than the MNV of normal cells.

4.2.4 Case Removal

During segmentation, some of the case images were rejected (such as when they had high average intensity or when their segmentation contained blobs that were beyond the threshold of *MaxBlobSize*). Rejecting a high percentage of images of a case during segmentation shows that the segmentation is failing for that specific case (the acquisition is bad, the segmentors are often segmenting clustered nuclei as a single nucleus, etc.). Also, a quite low number of accepted segmentations from a case can lead to an unreliable final estimation of volume (PSI-V_v).

Based on these observations, the whole case was removed and was not processed further if the number of accepted segmentations was less than *MinNumImage* or the ratio of accepted segmentations to original images was less than *MinRatio*. The number of accepted segmentations was set to the average number of accepted segmentations by each of those 72 segmentors.

4.2.5 Volume Estimation

To estimate the MNV which was the final feature for classification, stereological methods were used. This estimator uses a point-sampled intercept to sample segmented nuclei to estimate the MNV, which is termed volume-weighted MNV (PSI-V_v) [159]. The three main steps are placement of a point-grid for point sampled intercept (PSI) sampling, collection of line lengths across sampled nuclei (l), and finally the computation of estimated PSI-V_v as

$$V_v = \frac{\pi \sum_{i=1}^N l_i^3}{3N},$$

where N is total number of nuclei sampled by PSI in the region of interest [143].

4.2.6 Final Estimated Volumes

After performing all the steps above, 72 estimated (nuclear) volumes per tissue were computed. However, the number of estimated volumes was reduced to 18 as follows.

Intuitively, because the intersection of different blobs is at most as large as the smallest blob, the intersection of different segmentations will have a smaller MNV than all other segmentations. Minimizing the MNV meaningfully increases the separation. Hence, among each of the four segmentations with the same pair of parameters, (*MinBlobSize*, *MaxBlobSize*), the minimum estimated volume was chosen as the final estimation for that specific pair of parameters. Among the 18 remaining values for each case, the median value was taken as the final estimated MNV.

In several experiments it was observed that if after creating the 18 values for each case the maximum, median or mean of the four values (instead of the minimum estimated MNV) were extracted from four segmentations with the same pair of parameters, the final accuracy was always lower.

In a different experiment, the final MNV was computed from 72 estimated values as follows. After performing the convex check and removing non-convex blobs, the ratio of the remaining convex blobs to all original blobs was computed. For each case, 18 segmentors with the highest such ratios were selected and their corresponding 18 estimated MNV's were kept. Finally, the median of these 18 final values was selected as the final estimated nuclear volume. This process may select several segmentors with the same pair of parameters, (*MinBlobSize*, *MaxBlobSize*), while choosing none from some other pairs.

4.3 Dataset

The dataset used for experimenting had 30 normal cases and 32 cancer cases. On average, each normal case has 387 images and each cancer case has 534 images. The reason for the

difference in the average number of images in normal and cancer cases was that the chosen ROI's in cancer cases were larger on average.

The images sizes were 1138x759 and in all cases tissues were stained with H&E, which enhances the signal to noise ratio (SNR) of cell nuclei prior to image acquisition.

4.3.1 Image Acquisition

Archived cervical tissue from a cone biopsy or surgery sectioned at 6 um and stained with H&E at the Moffitt Cancer Center were used and their images were acquired using an integrated hardware-software-microscope system (Stereologer, Stereology Resource Center, Inc. Tampa - St. Petersburg, Fl.). Images were acquired by placing the tissue sample/ biopsy slide with normal or cancer (squamous cell carcinoma) tissue under the microscope. The automatic XYZ stepping motor and Stereologer software were used to manually outline an ROI at low magnification. Within each ROI around 200-1000 2-D images were captured over a single focal plane at 40x magnification.

4.4 Results and Discussion

In this section, the results, in terms of the Area Under the Receiver Operating Characteristic (ROC) Curve (AUC) and the accuracy (estimated by performing 10-fold cross-validation, 10 times and averaging over all values) are presented. The method *Ensemble 2* in [143] is denoted by *Image Ensemble* and the current proposed method is denoted by *Large Ensemble*. Moreover, the variant of the proposed method (which chooses segmentors based on their ratio of convex to non-convex blobs) is denoted by Ratio Ensemble. For the Image Ensemble no case was removed, as it does not have an automatic rejection step. However, for Large Ensemble and Ratio Ensemble, cases were removed automatically. This removal was done where there was a low ratio of accepted segmentations or low number of accepted segmentations (below the specified thresholds). The results (AUC and accuracy) for the

Large Ensemble and Ratio Ensemble are presented for four different pairs of parameters of *MinRatio* and *MinNumImage* of (10%, 50), (33%, 50), (10%, 75) and (33%, 75). Using these pairs of parameters respectively removed two, four, six and eight cases (out of 62 cases). The eight cases that were removed by the pair of parameters, (33%, 75), are listed below.

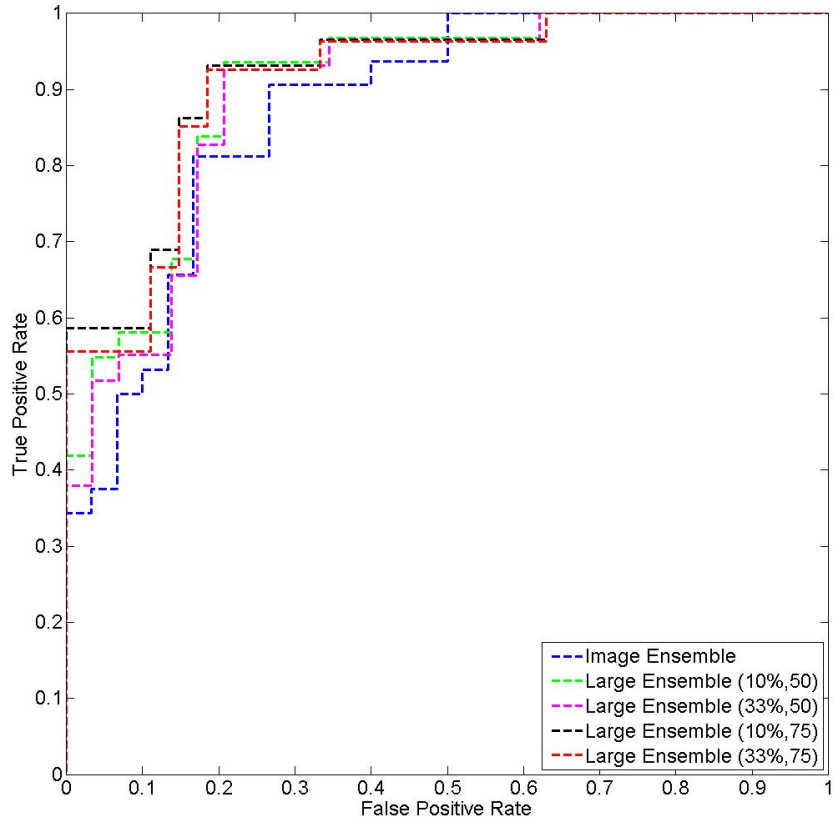


Figure 4.5: ROC curve for Image Ensemble and variants of Large Ensemble.

1. The ratio of accepted segmentations to all images was less than 33%.

This test removed four cases, one normal case, NL-38 with 0.125 ratio, and three cancer cases, CA-11, CA-1234 and CA-35 respectively with ratios of 0.281, 0.037 and 0.2557.

2. The number of accepted segmentations was less than 75.

This check removed six cases two of which were the same as cases which were recommended for removal in (1). The new cases for removal were two normal cases, NL-39

Table 4.1: AUC and accuracy of the methods

	AUC	Accuracy
Image Ensemble	0.8760	77.4%
Large Ens. (10%,50)	0.9010	80.5%
Large Ens. (33%,50)	0.8942	81.2%
Large Ens. (10%,75)	0.9170	82.5%
Large Ens. (33%,75)	0.9108	84.3%
Ratio Ens. (10%,50)	0.8598	73.2%
Ratio Ens. (33%,50)	0.8537	72.2%
Ratio Ens. (10%,75)	0.8851	76.4%
Ratio Ens. (33%,75)	0.8793	75.6%

and NL-65 respectively with 66 and 70 accepted segmentations and two cancer cases, CA-69 and CA-70 respectively with 63 and 66 accepted segmentations.

The ROC curves of both the Image Ensemble and Large Ensemble with the four different pairs of parameters are shown in Fig. 4.5 (for simplicity the ROC curves of the Ratio Ensemble are not presented). As ROC curves show, almost always, all variants of the Large Ensemble method had a better TP rate than the Image Ensemble with the same FP rate.

The AUC and the accuracy of these methods are summarized in Table 4.1. The AUC of all variants of the Large Ensemble are higher than Image Ensemble's (and also Ratio Ensemble's). The accuracy obtained from the Ratio Ensemble is always 5 to 10 percent lower than that of Large Ensemble with the same set of parameters. For the Large Ensemble, although the AUC was not monotonically increasing as the rejection criteria were relaxed, the accuracy was increasing as more cases were being rejected. However, it has been seen that by rejecting more than 15 cases (parameter pair of (33%, 100) rejects 14 cases and has accuracy 84.6%), the accuracy started to decrease.

4.5 Summary

A new large ensemble algorithm was proposed to distinguish between normal and cancer cases using a single feature, the estimated cell nuclei volume (PSI-Vv). Four different segmentors, which use several applications of Otsu thresholding along with morphological operations were used to segment microscopy images from normal and cancerous cervical tissues. During segmentation several checks (such as average image intensity, minimum and maximum blob size, etc.) were used to improve segmentation. Also, a concavity check ensured that a segmentation containing nuclei and blobs which do not pass the check are removed. This method also removed some cases automatically, if the number of accepted segmentations do not meet certain criteria. This means that in contrast to the approaches proposed in [143], a manual screening step is not required. The four main segmentors were used with several different pairs of parameters and the MNV of each cases was estimated from the results of each of those segmentors. In the end, 75% of all estimated values are discarded and the median of the remaining values were used for classification. The downside is the greater computation time. In the previous method, which is denoted by Image Ensemble here, a single pair of parameters, checked blob sizes, was used and four segmentations and an ensemble segmentation from them were computed. The process of creating the four segmentations took more than 80% of the computation time, but small blob removal and checking the size of the largest blobs took less than 5% (the rest was spent generating the ensemble segmentation and accessing and saving the data). In the proposed method, the four segmentations were generated 18 times using different sets of parameters. This increased the computation time to around three times that of the previous method. The results of the proposed method were compared to the Image Ensemble's. Results show that the new method has improved AUC plus accuracy of the Image Ensemble method. By setting the parameters such that two cases were removed, the accuracy was increased by 3% and by rejecting more cases accuracies as high as around 85% were achieved. One of the best results

was achieved with a large ensemble approach that rejected 8 cases (out of 62 cases) with an accuracy of 84.3% and AUC of 0.911.

Chapter 5

Cervical Tissue Segmentation and Classification Using Adaptive Shape Modeling

Part of this chapter was published in the 2016 IEEE International Conference on Image Processing [160].

5.1 Introduction

The manual diagnosis of diseases from histology or cytology images is costly and time consuming. Potential misdiagnoses may arise from fatigue or knowledge of the expert [161], leading to over-treatment and missed disease. Diagnostic classification of malignant and benign tissue from pathology images provides information to the pathologist for precise cancer staging assessment, accelerating patient-specific medical care. However, phenotypic niche areas including nucleus, fuzzy cell borders, and cytoplasm pose a significant barrier for evaluating slice-based malignancy.

Prior studies mostly focused the whole-slide level evaluation [162, 163] that do not consider nucleus-level features. The nucleus-level analysis from pathology images currently uses the human visual system without quantitative measurement [1]. Furthermore, current human assessment is largely restrained to semantic descriptions of size, thickness, or pleomorphism that could not substantially quantify various nucleus characteristics. In view of these challenges, the following specific questions can be asked: 1) How can a computational framework that is capable of capturing quantitative information from the *nucleus* – instead of *whole-slide pathology images* – be designed that is advantageous in providing useful clin-

ical interpretation for patients? 2) If the goal is to classify tissues, is it necessary to have the most accurate segmentation or may a simpler segmentation method be as effective for classification?

In this work, the problem of cervical cancer diagnostic classification based on pathology images is studied. To capture the nucleus-level dynamics a Adaptive Nucleus Shape Modeling algorithm is proposed to capture nucleus-level information from pathology images, including an adaptive nucleus segmentation and nucleus shape appropriation. The nucleus-level texture feature representation is then applied to classify the whole tissue malignancy. By comparing classification accuracy using features extracted by the proposed segmentation method to the results obtained by one of the state-of-the-art segmentation methods [89], it will be shown that features extracted from a subset of segmented nuclei using a simpler segmentation method can be more effective for classification. More generally, the proposed approach can be readily extended to classify different subregions of a whole slide cervical tissue image.

In what follows, an algorithmic framework of nucleus-level analysis to classify cervical tissues beyond conventional whole-slide analysis is introduced, and the methodological contribution is three-fold:

- Adaptive Nucleus Shape Modeling (ANSM) is proposed to capture the nucleus shape in pathology images, including adaptive nucleus segmentation using a multilevel thresholding scheme and nucleus shape approximation by ellipse shape fitting.
- The limitation of missed nuclei labeling information is overcome by proposing two intermediate steps to potentially remove poorly segmented nuclei and reduce the number of mislabeled training instances to boost classifier performance.
- It has been shown that nucleus-level texture features obtained from segmented nuclei are effective in classifying the whole cervical tissue malignancy, providing evidence that nucleus-level analysis is valuable in understanding cervical tissue characteristics.

Computer-aided diagnosis systems for histology analysis were proposed to classify tissue images [162] or subregions within the whole slide [164]. This is normally performed in two main steps: feature extraction and classification. Segmentation can also be used to create masks formed from patches aligned to nuclear centers [165]. Without using a proper segmentation, composite hashing and bag of features can be used to extract features [162, 166]. Popular methods to classify natural scenes [167, 168] may also be used for histology classification [165]. However, most of these systems are designed for tissue classification including lung [162, 163], breast [81, 169], prostate [164] and kidney [170] tissues and limited effort has been put on cervical tissue quantification and classification.

In [162], lung microscopic tissue images are classified as adenocarcinoma or squamous carcinoma using a Composite Anchor Graph Hashing algorithm with average accuracy 87.5%. In [81], breast histology images are separated into three regions based on blob density and classification. In [164], subregions in prostate tissue images are classified into stroma, normal or prostatic carcinoma using morphological characteristics and texture features with a classification accuracy of 79.3%. Biologically interpretable shape-based features and a series of SVM classifiers are used for classification of histological renal tumor images into three types of renal cell carcinoma and one benign tumor with an average accuracy of 77% [170]. Finally, in [144], mean nuclear volume of segmented nuclei within cervical histology images was used to classify cervical tissues with an average accuracy of 84.3% and a rejection rate of 13%.

5.2 Methods

Given a cervical tissue histology image, the goal is to approximate the nucleus location and shape boundary for effective nucleus-level analysis. In this work, multilevel thresholding is used to accomplish nucleus segmentation, and an ellipse shape fitting model has been used to maximally capture the nucleus information (Fig. 5.1). Details are given in the following.

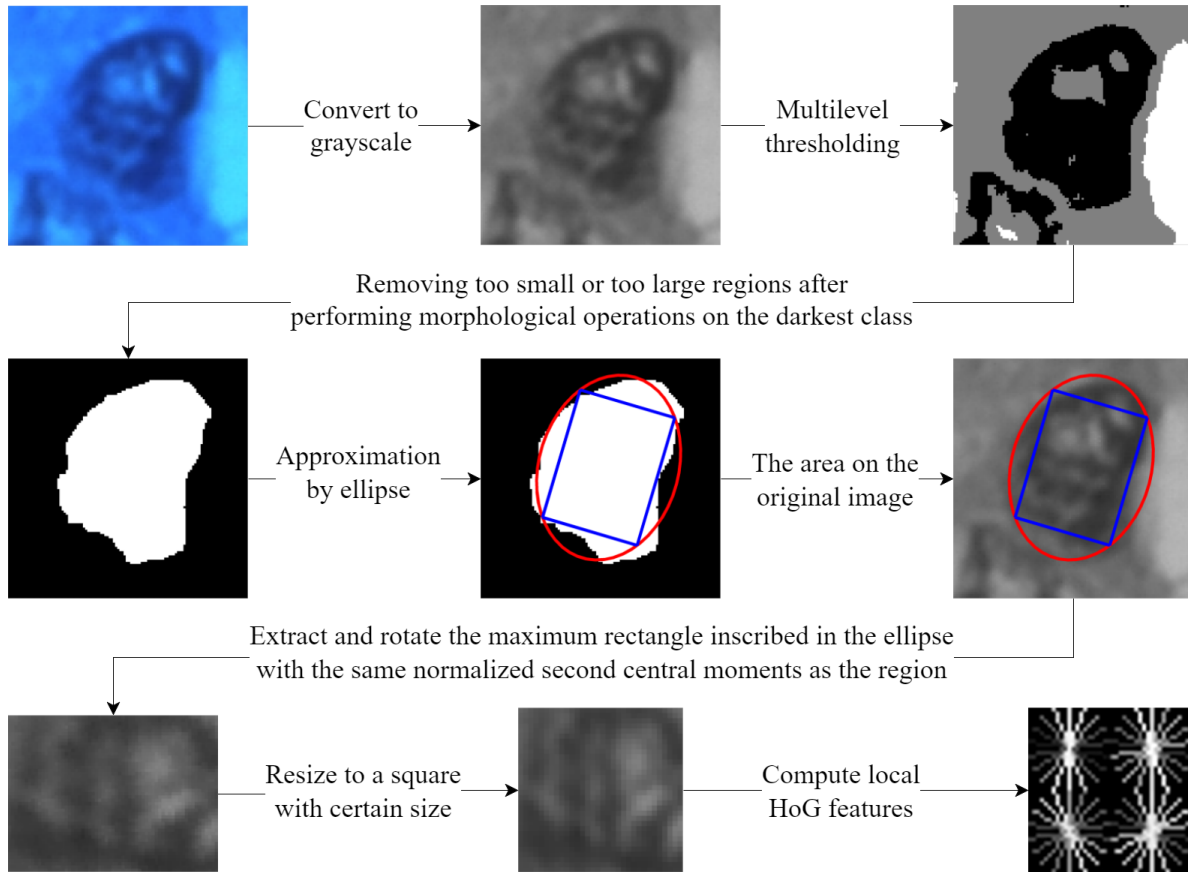


Figure 5.1: Overview of the proposed Adaptive Nucleus Shape Modeling (ANSM).

5.2.1 Adaptive Image Segmentation

An adaptive multilevel thresholding nucleus segmentation method was developed to identify the nuclei area from a raw pathology image. Due to the various nuclei morphology, it is challenging to use a single thresholding scheme for precisely delineating a nucleus shape from pathology images. To maximally preserve the nucleus geometrical shape information, while minimizing potential shape outliers, a framework to capture nuclei using a segmentation algorithm described in Algorithm 1 is proposed and used.

The segmentation algorithm can be understood as an iterative process: at each round, the darkest region R was obtained from a multilevel thresholding [142]. Morphological operations are incorporated to retain the primary blobs as S_i and by comparing the total nucleus area of

S_i , denoted as A_i , the *goodness* of S_i is measured. Algorithm takes the smallest and largest permitted nucleus size as input, which are denoted by m and M , respectively.

Algorithm 1: Adaptive Image Segmentation (m, M)

```

1 Set  $n = 0, A_0 = \epsilon$  while  $A_n > 0$  do
2   Set  $n = n + 1$ 
3   Perform  $n$ -level thresholding and let  $R$  denote the darkest region
4   Perform morphological operations filling and opening on  $R$ 
5   Remove blobs larger / smaller than  $M / m$  in  $R$ 
6   Denote the new region by  $S_n$ 
7   foreach segmented blob  $b$  do
8     Segment  $b$  using two-level thresholding
9     Remove  $b$  if it contains more than one region larger than  $m$ 
10  Set  $A_n$  as the area of  $S_n$ 
11 Return  $S_k$  as the final segmentation where  $k = \arg \max_i A_i$ 

```

5.2.2 Nucleus Shape Approximation by Ellipse Fitting

The blobs in the final segmentation were mostly a rough approximation of their exact nuclei area. Because a nucleus normally has an elliptic shape, each nucleus area was approximated with the ellipse with the same normalized second central moment as the segmented nucleus area. For each nucleus region, the coordinates of the centroid of the region, with pixel coordinates (x_i, y_i) for $i \in \{1, 2, \dots, N\}$, are

$$\bar{x} = \frac{\sum_{i=1}^N x_i}{N} \text{ and } \bar{y} = \frac{\sum_{i=1}^N y_i}{N}. \quad (5.1)$$

The central moments of order $p + q$ of a continuous bivariate probability distribution $f(x, y)$ about the mean $\mu = (\mu_X, \mu_Y)$ was defined as

$$\mu_{p,q} = \int_{-\infty}^{\infty} \int_{-\infty}^{\infty} (x - \mu_X)^p (y - \mu_Y)^q f(x, y) dx dy. \quad (5.2)$$

Therefore, for the discrete case of binary region pixels, by considering each pixel as a square with unit length, $f(x_i, y_i) = 1$ and the central moments are

$$\mu_{p,q} = \sum_{i=1}^N \left(\int_{y_i - \frac{1}{2}}^{y_i + \frac{1}{2}} \int_{x_i - \frac{1}{2}}^{x_i + \frac{1}{2}} (x - \bar{x})^p (y - \bar{y})^q dx dy \right). \quad (5.3)$$

Specifically, the second central moments, $\mu_{2,0}$, $\mu_{1,1}$ and $\mu_{0,2}$ are respectively computed as

$$\sum_{i=1}^N [(x_i - \bar{x})^2] + \frac{N}{12}, \quad \sum_{i=1}^N [(x_i - \bar{x}) + (y_i - \bar{y})], \quad \sum_{i=1}^N [(y_i - \bar{y})^2] + \frac{N}{12}, \quad (5.4)$$

and finally the normalized second central moments, $\mu'_{p,q}$, are defined as the second central moments divided by the number of pixels, N . Subsequently, the major axis, minor axis and orientation of the ellipse, and then coordinates of the rectangle inscribed in the ellipse were computed from the normalized central moments. This approximation using the best fit ellipse was designed to improve the area estimation for the cells with nonuniform intensity. Feature extraction then proceeded from the maximum rectangle inscribed in the defined ellipse.

5.2.3 Feature Extraction and Classification

The maximum rectangle inscribed in the obtained ellipse was rotated and then resized to a square with a fixed size (32x32 in this study). The shape normalization allowed for extracting the same dimension of Histogram of Oriented Gradients (HOG) or Local Binary Patterns (LBP) features from nuclei with different sizes. Instead of original HOG features [138], the UoCTTI variant [171] was used that compresses the 36 features into 31 features. The cell-size was set to 16, which decomposes the nucleus into 4 subregions, and a total number of 124 features were extracted. All the segmented nuclei in each training tissue were labeled as the label of their corresponding tissue. Segmented nuclei in testing tissues were classified by a Support Vector Machine (SVM) classifier with a Radial Basis Function

(RBF) kernel and k-Nearest Neighbor (kNN) classifier in separate experiments and tissue classification was done based on the majority class of its labeled nuclei.

5.3 Dataset

The dataset included 20 normal and 19 cancer sample tissues (cases). The tissues were stained with Hematoxylin and Eosin. Sample regions with normal or cancer cells were indicated on the glass slide by a pathologist and from the marked regions for each case, 10 images with size 1200x800 were acquired using a 40x objective.

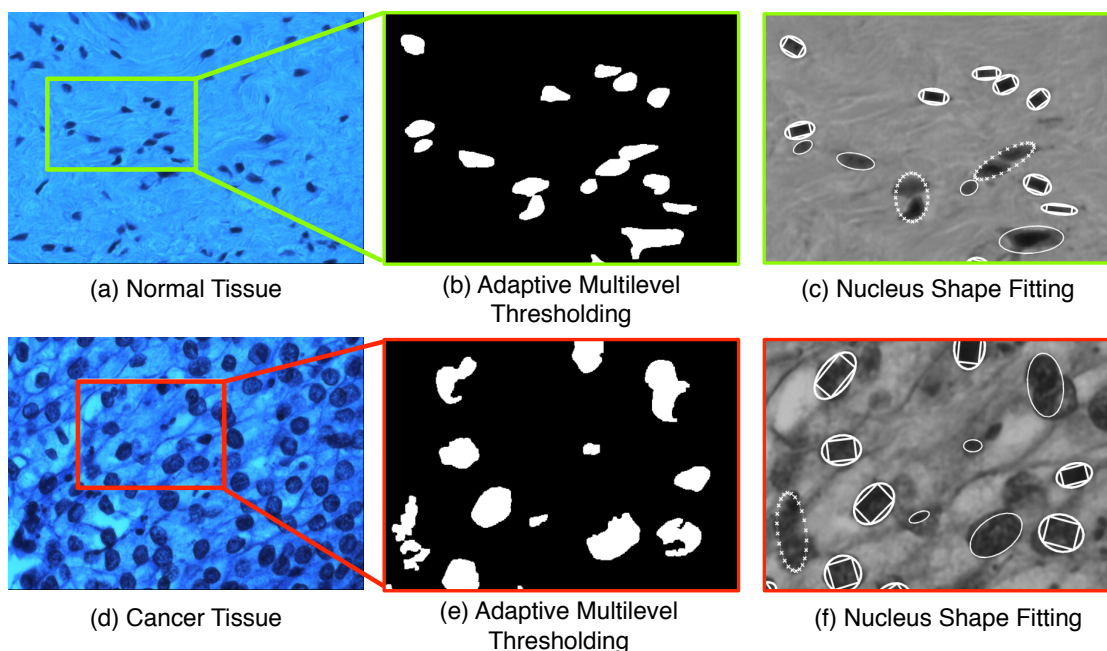


Figure 5.2: Steps of the segmentation algorithm. Segmentation of a normal (a) and a cancer tissue (d); darkest class after multilevel thresholding and performing morphological operations (b, e); cells shown with rectangular areas are kept and the others are rejected (c, f).

5.4 Results and Discussion

Due to the focus on nuclei-level analysis, nuclei segmentation can directly affect the classification performance. The observations indicated that, when segmentation inaccuracies

occur, images of normal tissues were typically under-segmented and the images from cancer tissues were typically over-segmented. The reason was apparent on inspection: normal nuclei appear solid with uniform staining intensities. If they were isolated from other nuclei, their areas were segmented accurately. If they overlapped with other nuclei, however, they were segmented together with those nuclei, leading to under-segmentation of the nucleus areas. In contrast, cancer nuclei have non-uniform staining intensities and exhibit more heterogeneous clumping within the nuclei, that in many cases cause the segmented nucleus to be separated and treated as two or more nuclei (Fig. 5.2). To address this issue, in a second version of the proposed model, denoted by ANSM₂ (the first version is denoted by ANSM₁), only features from half of the segmented nuclei were extracted and used: Segmented nuclei with corresponding inscribed rectangle size in the second and third quartile are kept and others are rejected.

Fig. 5.2 shows examples of images from normal and cancer tissues, their segmentations, nucleus approximation and rejected segmented nuclei.

5.4.1 Parameter Selection and Results

The only parameters used in the proposed segmentation method, m and M , were set to 250 and 5000, according to image size. To choose the parameters of the SVM kernel, C and γ , a grid search was performed and the best set of parameters were chosen based on the accuracy obtained from a 10-fold cross validation on the whole dataset. Similarly, the parameter k for kNN was set. The parameters were then fixed and the accuracy of a set of parameters were estimated again by the average of ten, 10-fold cross validations. Because the parameters were chosen based on a 10-fold cross validation on the whole dataset the final results can be slightly optimistic. The reported results in Fig. 5.3 were obtained by setting $C = 128$ and $\gamma = 0.25$ for SVM and $k = 5$ for kNN. The highest accuracy was obtained by ANSM₂ using HOG features and SVM. For these settings, an accuracy of 93.33% was

obtained, all misclassified tissues were normal tissues and therefore, the false negative rate was zero. The false positive rate was 13%, average precision through all cross validations was 87.96% and average recall was 100%.

For comparison purposes, the performance of one of the state-of-the-art segmentation methods [89] (denoted by LTDC) was evaluated. LTDC needs training data to build its model. Therefore, one image from each of the cases was manually annotated and the model was trained using the 39 annotated images. The rest of the images in each case were used for testing. Also common parameters, such as m and M , which are also used by LTDC are set as in the proposed method. The results of this method and both versions of ANSM are presented in Fig. 5.3.

Interestingly, ANSM₁ behaves very different than ANSM₂ while ANSM₂ behaves very similar to LTDC. For example, kNN and LBP features performed better than SVM and HOG features in ANSM₁ although it was exactly the other way for both ANSM₂ and LTDC. In fact, when removing half of the training and test instances, which contained most of the misclassified labels and instances, ANSM₂ could slightly outperform LTDC and behaved very similar to it. It suggests that, for the task of classification, choosing a subset of well-segmented regions by a simpler segmentation method can be as useful as using a more advanced segmentation method.

5.4.2 Discussion

Most of the misclassified tissues (29 out of 33) among all cross validations are related to only three normal tissues. Visual examination shows that images from these tissues have an atypical appearance from other normal tissues. Fig. 5.4 shows examples of these cases. Unlike other normal tissues, two of these cases have several clumps of adjacent cells and one of them has images with high contrast background and high intensity variance. A more accurate segmentation can provide better training instances and therefore allows for higher

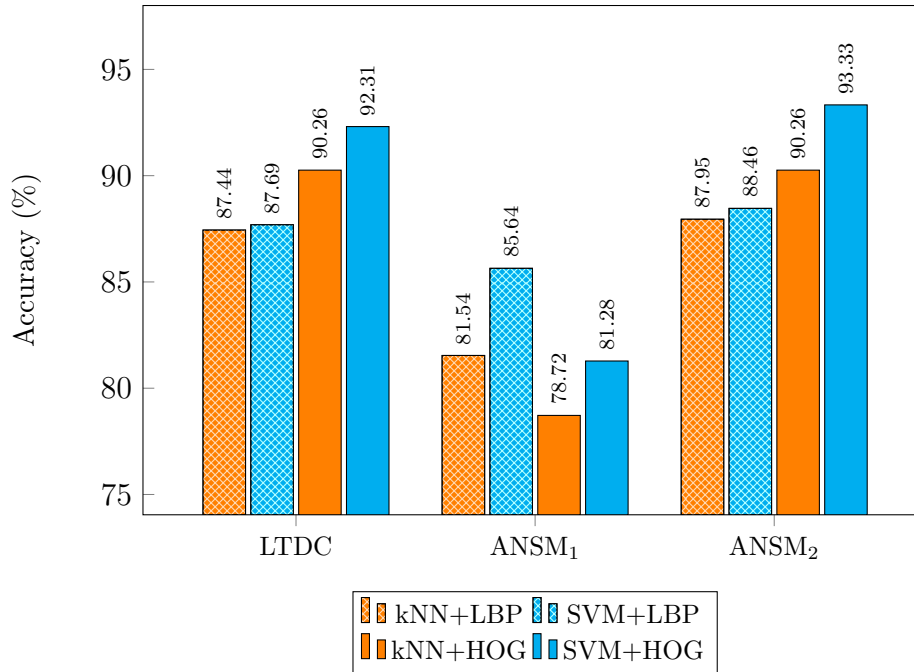


Figure 5.3: Tissue classification accuracy.

accuracy. One approach for improving the segmentation will be to reduce the variation of staining intensities in images from different tissues from the same class (normal or cancer).

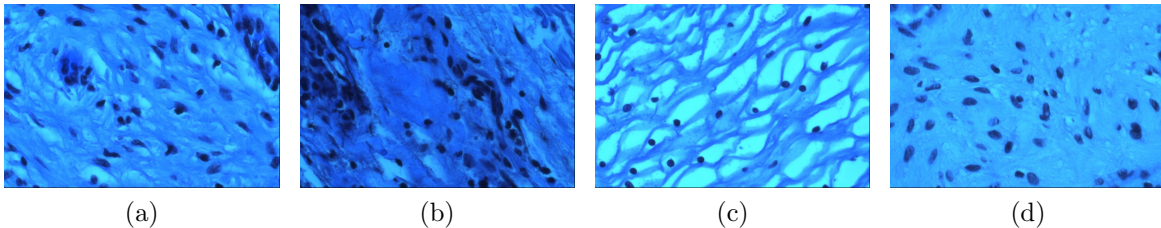


Figure 5.4: Images from normal tissues. (a-c) images from three normal tissue samples that contribute most of misclassified testing instances; (d) an example image from one of the other normal tissues.

5.5 Summary

A novel algorithmic framework to tackle the challenging problem of nucleus-level pathological image analysis for cervical tissue classification is proposed. Cell regions are approximated using the ellipse with the same normalized second central moments as the region

and the rectangular area inscribed in the ellipse. These areas are resized to a square with a selected size, followed by extraction of HOG features from each quadrant of the squared sub-image. The SVM classifier with a RBF kernel classifies each cell and different tissues are classified according to the majority of their cell classes. It has been shown that the texture features extracted from segmented nuclei are able to capture class-specific tissue characteristics, which opens the space for exploring nucleus-level analysis in pathological image evaluation. Experimental results showed that the proposed method achieved classification accuracy of 93.33% with false negative rate of zero and area under the ROC curve of 0.9997. The accuracy was estimated with the average accuracy of ten, 10-fold cross validations. By comparing classification accuracy obtained using the proposed segmentation method it has been shown that by using a proper shape modeling a simpler segmentation method can be as effective as a more advanced segmentation method, for the task of classification. Also, the proposed segmentation method is much faster than LTDC and does not need any extra detection ground truth dataset¹, which makes it more applicable in real life situations.

¹In other words, the proposed method does not need an extra training dataset with manually marked cells to learn the model/parameters unlike the LTDC method.

Chapter 6

Overlapping Cervical Cell Segmentation in Cervical Cytology Images

Part of this chapter was published in 2016 IEEE 13th International Symposium on Biomedical Imaging (ISBI) [172] and is under review for publication in the Journal of Computerized Medical Imaging and Graphics [173].

6.1 Introduction

The Pap test is one of the main screening tests used to diagnose cervical cancer in its early or precancerous stages. Conventionally, the slides containing the Pap smear are examined under a microscope by a cytologist or pathologist and the slide is graded based on a system such as The Bethesda System [174]. However, this manual process is time consuming and is prone to errors and intraobserver variability. False negative rates are as high as 20 to 30% [175]. These errors can occur because of clumping of cells, blood, bacteria or yeast contamination [175]. To reduce such errors and workloads on pathologists and produce more consistent results computer systems are proposed to automate the slide analysis. Although newer preparation techniques (such as ThinPrep, SurePath, etc.) remove most of the mucus and inflammatory cells and decrease the number of overlapping cells, automating analysis of slides is still a very challenging task due to 1) folded cervical cells with spurious edges, 2) poor contrast of the cytoplasm area, 3) presence of bacteria, neutrophils, mucus and inflammatory cells and 4) overlapping cells. Also, the prepared *monolayer* slides can still range upwards of $30\mu m$ from glass to coverslip [126]. Therefore, it is impossible to have all cervical cells in-focus simultaneously in a single focal plane. One solution is to capture

images at different focal planes in a way that each cell is in focus in at least one of them. This can be done by approximating the thickness of the slide by finding the top and bottom focal planes with cells and capturing images at intervals in between [176]. All the images in such stacks need to be checked for abnormal cells. However, with Extended Depth of Field (EDF) algorithms [127, 128], a single image can be created from the whole stack of images to have all cells in focus. These EDF images can subsequently be used by automated systems to be segmented and searched for abnormal cells.

Most of the current automated systems mainly aim to segment (overlapping) nuclei and cell clumps (cellular masses) [68, 42, 111, 120, 114, 119]. These methods focus on nucleus segmentation and/or cell clumps and do not address the individual cytoplasm segmentation. Some methods address the segmentation of free lying or partially overlapping cells cytoplasm [113, 117, 122]. These methods assume that either the cells are not overlapping or the overlapping degree is very low. However, this is not realistic as cells usually have higher overlapping degree in real cervical cytology images. Cell clumps have a median of three nuclei and they contain more than four nuclei on average [176].

Recently, there was an increase in the number of methods proposed for complete segmentation of overlapping cervical cells. This increase is mostly due to the first and second overlapping cervical cell segmentation challenges held in International Symposium on Biomedical Imaging (ISBI) 2014 and 2015 [177, 51]. The datasets in both challenges are publicly available and contain training (with ground truth) and test sets. This made the evaluation and comparison of different methods possible. Therefore, recent methods are mostly addressing the more challenging task of overlapping cytoplasm segmentation [51, 177, 178, 179, 172].

Lu et al. [51] segmented cell clumps by applying the Quick Shift method [180] that results in a map of super pixels, applying an edge detector and learning an unsupervised binary classifier. They detected and segmented nuclei by finding the Maximally Stable Extremal Regions (MSER) [90] and segmented overlapping cytoplasm by joint optimization

of multiple level set functions, where each function (representing a cell) has both unary (intra-cell) and pairwise (inter-cell) constraints. Ushizima et al. [181] created a map of super pixels by merging regions based on pixel adjacency and intensity similarity using a graph-based linear-time algorithm [135] and followed it by a global search cut-off algorithm [182] to segment cell clumps. To segment nuclei inside cell clumps they used a local thresholding method [136] and segmented overlapping cytoplasm by partitioning the image into convex polygons through Voronoi diagrams. Lee et al. [179] also generated superpixels to segment cell clumps: the SLIC superpixel method [106] was used to generate a superpixel map and the map was thresholded using adaptive thresholding algorithm [182] to obtain the final cell clump regions. To segment nuclei they performed a local thresholding and removed outliers based on features such as mean intensity, circularity and size. They finally segmented overlapping cytoplasm by superpixel partitioning and assigning each superpixel region to the nearest nucleus. Then, the boundaries were refined by a cell-wise contour refinement with graph cuts [66] for each cell separately.

Most of these methods rely on superpixel and/or level set methods. Superpixel methods usually do not give accurate segmentations and level set methods are computationally expensive and are sensitive to parameter initializations. Therefore, I propose a method that sets most of its parameters adaptively and is substantially faster than other recent methods. In the previous version of the algorithm [172] I segmented nuclei by iterative thresholding. Regions were grown naturally by subsequent thresholdings and were filtered based on their features such as mean intensity, solidity, standard deviation, circularity and size. Cell clump segmentation was done by thresholding based on a learned GMM followed by morphological operations. To segment overlapping cells I defined a focus measure for subimages in the images and assigned subimages to nuclei based on their location and focus similarity. The contours were then refined in two coarse (subimage level) and fine steps (pixel level). Current work is an improved version of the previous work [172]. The nucleus segmentation process

has been replaced by an algorithm that considers solidity of regions as their main feature. This simplified the algorithm, made it more resistant to brightness changes in images and also increased the method's nucleus detection accuracy in the experiments. The cell clump segmentation step is also improved by adding a filtering step. The main modification was done to the cytoplasm segmentation step, replacing the previous refinement step. For the refinement, I defined a weight vector and used it in the process of finding the new boundary points candidates. A smoothing filter was applied to the candidate points and the outliers were found based on the distance of each candidate point to its corresponding new location. After removing outliers, I applied the smoothing filter again and obtained the new estimated boundary. The whole process was repeated until the boundaries converged.

The major contribution of this work is the proposed novel method for the boundary approximation of overlapping cells that utilizes the information in the image stacks efficiently to approximate the boundary for the subsequent refinements (the method is discussed in 6.2.3.1). Two other contributions are: 1) the proposed nucleus detection and segmentation method that achieves superior results compared to other state-of-the-art methods in terms of F-measure (the method is discussed in Section 6.2.1 and the results are presented in Subsection 6.4.3.1), and 2) the fine refinement step (discussed in Subsection 6.2.3.3) with the defined weight vector (Eq. 6.7) that can refine the boundaries effectively if only a small ratio of useful edge pixels exist (note the refined boundaries in Fig. 6.1d).

Other than the contributions mentioned above the methods run very fast (as discussed at the end of Subsection 6.4.3) and achieves substantially better results compared to other state-of-the-art algorithms in terms of the rate of missed cells. Moreover, it has fewer parameters to tune (two parameters, as discussed in Section 6.4) than other state-of-the-art algorithms. Finally, I propose to report a new metric (in Subsection 6.4.1), False Discovery Rate at object level, that helps capturing the cell detection accuracy effectively.

6.2 Methods

Each cell contains a nucleus and segmenting nuclei is generally easier than segmenting individual cytoplasms. I start the segmentation process by segmenting nuclei and then segment corresponding cytoplasm for each nucleus. The framework contains three main steps: 1) nucleus detection and segmentation (Section 6.2.1), 2) cell clump segmentation (Section 6.2.2) and 3) overlapping cytoplasm segmentation (Section 6.2.3). The first two steps use the EDF image and the last step uses a stack of images to segment cytoplasm (in the case of the ISBI 2014 dataset that does not contain stack images, the algorithm was modified to only use the location of subimages as discussed in 6.4.3.2). Fig. 6.1 shows the steps on a real cervical cytology EDF image.

6.2.1 Nucleus Detection and Segmentation

The goal of this step is to detect and segment nuclei.

Nuclei are commonly represented by small uniform relatively dark and convex regions. Therefore, the three most visually distinctive and important features of nuclei are size, average intensity and solidity. I used these three features to design an iterative algorithm to detect and segment nuclei. Because each segmented nucleus is an indication of a cell the result of this step directly affects the outcome of the final cytoplasm segmentation. However, because of the way the cytoplasm segmentation method works, minor segmentation inaccuracies in this step will not affect the final results much. Therefore, generally, a detection inaccuracy has a more adverse affect on the final segmentation outcome and hence, the algorithm was mainly designed to have high sensitivity to nuclei rather than an accurate segmentation. The algorithm that I propose to do this task is a novel iterative approach to detect (and segment) nuclei and works as follows.

The image is first blurred using a 2-D adaptive noise-removal filter [183]. Then, the algorithm iteratively binarizes the image starting with a low threshold to find *seed points*

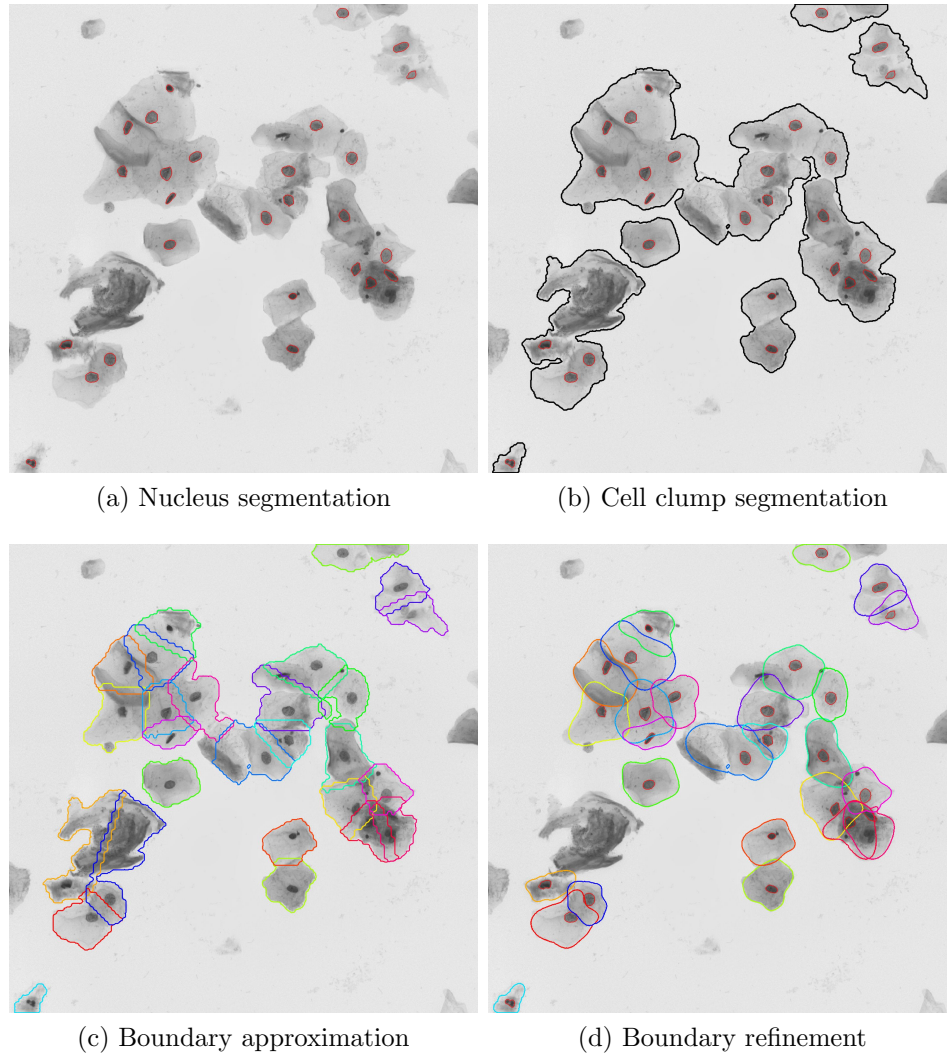


Figure 6.1: The results of the framework steps on a real cervical cytology EDF image.

from different nuclei. *Too small* or *too concave* regions are removed after each binarization and remaining regions are added to a nucleus mask. The nucleus mask keeps the nuclei regions segmented at each execution phase of the algorithm. A region replaces previous regions only if it has a larger solidity than all the previous region(s) overlapping it. This ensures that a newly appearing region does not replace any other more convex region(s). The thresholding range is decided based on the minimum and maximum average intensity of a typical nucleus in images. Also, the image is iterated in steps of 10 for faster computation. In two post-processing steps, regions are dilated and some of them are filtered. Those regions

whose difference between their outer boundary average intensity and region average intensity is smaller than a threshold are removed. Also, most of the artifacts are ignored because of their size (if they are isolated) or because of their solidity (if they are overlapping). As discussed in 6.4.3.1, although the algorithm is simple and very fast, it is also very accurate on both synthetic and real image datasets and outperforms other state-of-the-art algorithms. A detailed description of the algorithm is presented in Algorithm 2.

Algorithm 2: Nucleus Segmentation Algorithm

Input : EDF image I , min nucleus size m , min solidity s , low threshold t_1 , high threshold t_2 and min area and outer boundary average intensity difference d

Output: Binary mask of nucleus segmentation N

```

1  $N \leftarrow \emptyset$ 
2  $I \leftarrow \text{Wiener}(I)$ 
3 for  $t \leftarrow t_1$  to  $t_2$  step 10 do
4    $B \leftarrow I \leq t$ 
5   foreach region  $r$  in  $B$  do
6     if size of  $r < m$  or solidity of  $r < s$  then
7        $r \leftarrow \text{remove } r$ 
8     else if binary mask of  $r \cap N = \emptyset$  then
9        $N \leftarrow N \cup r$ 
10    else
11      /*  $r$  overlaps with regions  $r_1, r_2, \dots, r_n$  in  $N$  */
12      if solidity of  $r \geq$  solidities of all regions  $r_1, r_2, \dots, r_n$  then
13         $N \leftarrow N \cup r$ 
14      else
15         $r \leftarrow \text{remove } r$ 
16  foreach region  $r$  in  $N$  do
17    dilate  $r$ 
18    if average intensity of  $r -$  average intensity of outer boundary  $< d$  then
19       $r \leftarrow \text{remove } r$ 

```

Filtering regions based on a maximum size can also be considered in line 6 of Algorithm 2. Visually, it seems that including this filter may increase the segmentation accuracy. However,

including it does not change the results for the nucleus detection accuracy on the datasets used in the experiments.

6.2.2 Clump Segmentation

In this step, the cell clumps (cellular masses that contain cervical cells) are segmented from the background. Generally, the background in each EDF image is uniformly bright and the pixels of the foreground are darker but have more variation. It causes the brightness of the darkest background pixel to be essentially (and not always) higher than the brightest foreground pixel. Therefore, a simple thresholding and some morphological operations can potentially segment the background from foreground. Using this observation, a Gaussian Mixture Model (GMM) is learned with two components on the pixel intensities using the Expectation Maximization (EM) algorithm. One Gaussian estimates the distribution of foreground (cell clumps) pixel intensities and the other one estimates the background pixel intensities. Using the background Gaussian distribution the threshold T is set to $Q(q)$, where $Q(\cdot)$ is the quantile function of the normal distribution, which is defined as

$$\begin{aligned} Q(q) &= \inf \left\{ x \in \mathbb{R}, q \leq \frac{1}{\sqrt{2\pi}\sigma_b} e^{-\frac{(x-\mu_b)^2}{2\sigma_b^2}} \right\} \\ &= \mu_b + \sqrt{2}\sigma_b \operatorname{erf}^{-1}(2q - 1), \end{aligned} \tag{6.1}$$

where μ_b and σ_b are the mean and standard deviation of the background normal distribution and $\operatorname{erf}(\cdot)$ is the error function. Fig. 6.2 shows the histogram of pixel intensities of a real EDF image in the training set of the ISBI 2015 dataset, its corresponding estimated GMM and the selected threshold. After the image is binarized using the threshold T , a connected component analysis was performed. Those connected components that did not contain any nucleus or had *small* area or average intensity larger than $Q(q')$ are removed. Alternatively, those nuclei that do not overlap with any segmented cell clump are discarded.

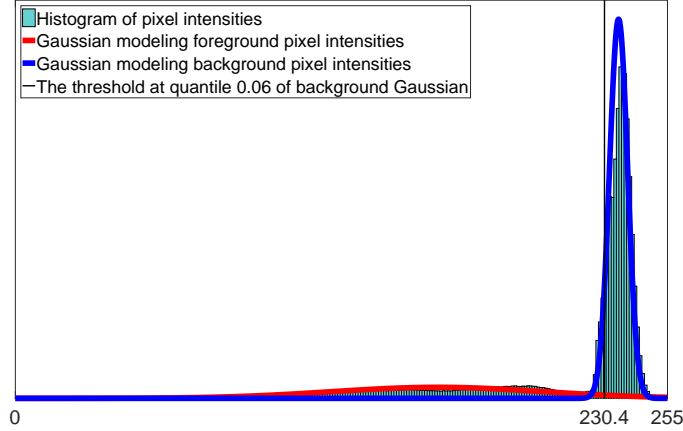


Figure 6.2: Histogram of pixel intensities of an EDF cervical cytology image in the training dataset, the estimated Gaussian Mixture Model and the selected threshold.

6.2.3 Cytoplasm Segmentation

This describes the main step of the framework segmenting the overlapping cytoplasm. Because of the squamous shape of cervical cells, usually the best focal plane to have a specific cell in focus is when the nucleus is in focus. Therefore, it can be safely assumed that when a nucleus is in focus its cytoplasm is also (at least relatively) in focus and vice versa. Based on this assumption, a cytoplasm boundary of a nucleus can be approximated by assigning the parts of the image that have a focus measure similar to the nucleus and are relatively close. These two criteria (being relatively close to the nucleus and having a similar focus measure to that of the nucleus) are the main criteria with which the cytoplasm boundaries using the image stack are approximated. After approximating the boundaries, they are refined in two more steps using the EDF image.

6.2.3.1 Boundary Approximation

To approximate the cytoplasm boundaries, a square grid with width W is first overlaid on each image in the stack. Instead of assigning pixels of the image to different nuclei, the boundaries are approximated by assigning grid squares (or subimages). This will increase the computational speed and also allows us to define a focus measure to estimate the focus

of the area enclosed in a grid square. Based on the assumption above, if two subimages near in distance to each other come into focus and go out of focus similarly in different images in the image stack then it is likely that they belong to the same cell. This will give us an approximation of cytoplasm boundaries.

Consider the (i, j) -th grid square (that is in row i and column j). For image k in the stack, the focus measure of $I_{i,j}^k$ ((i, j) -th grid square in the k -th image in the stack), $F_{i,j}^k$, is defined as the standard deviation of pixel intensities in the grid square. A focus vector of the (i, j) -th grid square is defined as the vector containing focus measures of all images in the stack, $(F_{i,j}^1, F_{i,j}^2, \dots, F_{i,j}^{20})$ (there are 20 images in each stack in the dataset). The focus vector is then normalized to have values within the range $[0, 1]$ and is denoted by $(\overline{F}_{i,j}^1, \overline{F}_{i,j}^2, \dots, \overline{F}_{i,j}^{20})$. Then the *focus distance* of the (i, j) and (i', j') -th grid squares, $S_{i,j}^{i',j'}$, is defined by the Euclidean distance of their corresponding normalized focus vectors,

$$S_{i,j}^{i',j'} = \sqrt{\sum_{k=1}^{20} \left(\overline{F}_{i,j}^k - \overline{F}_{i',j'}^k \right)^2}. \quad (6.2)$$

Also, to measure the closeness of (i, j) and (i', j') -th grid squares I set

$$C_{i,j}^{i',j'} = \sqrt{(i - i')^2 + (j - j')^2}. \quad (6.3)$$

Finally, the likelihood of the (i, j) and (i', j') -th grid squares belonging to the same cell is estimated by

$$L_{i,j}^{i',j'} = \exp \left(-\frac{C_{i,j}^{i',j'^2} + S_{i,j}^{i',j'^2}}{2\alpha^2} \right). \quad (6.4)$$

Using the likelihood measure, L , defined above on two subimages belonging to the same cell, the likelihood of a subimage belonging to the cytoplasm of a particular cell can be estimated using the fact that its nucleus is certainly a part of it. Therefore, to find out which subimages are a part of a particular cell I searched for subimages that have a high

likelihood of belonging to the same cell with the subimages overlapping with the nucleus. Hence, to compute the likelihood of the (i, j) -th subimage belonging to the cytoplasm of a cell with a nucleus that overlaps with $(i_1, j_1), (i_2, j_2), \dots, (i_{m'}, j_{m'})$ -th subimages, I set

$$L_{i,j}^m = \frac{1}{m'} \left(\sum_{s=1}^{m'} L_{i,j}^{i_s, j_s} \right), \quad (6.5)$$

where m is the index of the detected nucleus in a cell clump. Lastly, if there are N nuclei detected in a cell clump, namely nucleus 1 through N , (i, j) -th subimage is assigned to nucleus m if

$$\beta L_{i,j}^m - \sum_{\substack{n=1 \\ n \neq m}}^N L_{i,j}^n > 0. \quad (6.6)$$

In other words, a subimage is assigned as the cytoplasm of a cell if the weighted likelihood of it belonging to that cell is larger than the sum of the likelihoods of it belonging to other cells in the clump. By setting β the permitted degree of overlap between cells in a clump can be adjusted: by higher values of β the cells in a cell clump are allowed to overlap more with each other and vice versa.

In the next two processes I refined (revised, smoothed, etc.) the approximated boundaries.

6.2.3.2 Coarse Refinement

This step does *coarse* refinement as it only refines the boundary at the subimage level compared to the next refinement that is done at the pixel level. Unlike nuclei, which are almost always convex, the shape of cytoplasm can be concave. Therefore, enforcing convexity on cytoplasm boundaries is not realistic. However, only a limited level of concavity in cytoplasm boundaries is allowed. To do that, I defined *reachability* notation and removed those grid squares that are not reachable from the nucleus centroid. Suppose that the nucleus centroid falls in the (i, j) -th grid square. The (i', j') -th grid square is said to be

not reachable from the (i, j) -th grid square if there exists at least one grid square on the discretized line segment from (i, j) to (i', j') that is not assigned to the cell. Discretization can be implemented using the fast and simple Bresenham's algorithm [184]. Removing a grid square may make previously reachable grid squares not-reachable. The not-reachable grid squares are removed as long as such grid squares exist. Fig. 6.3 shows an example of two removed unreachable grid squares for a cell and its final shape.

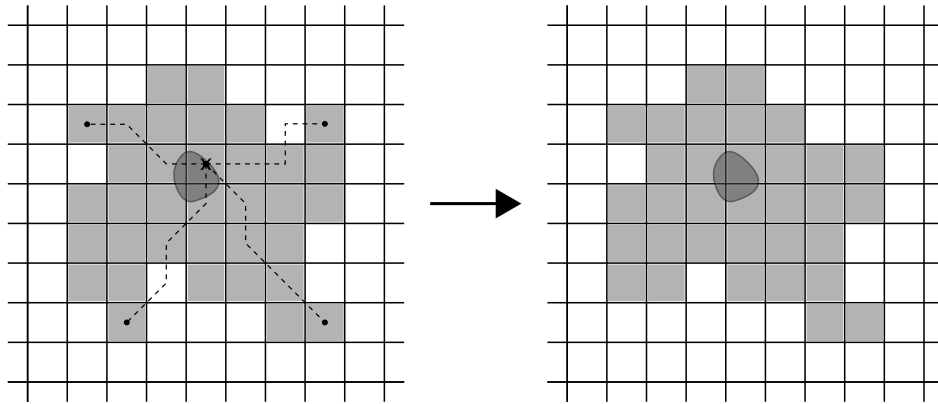


Figure 6.3: Coarse refinement: the subimages not reachable by centroid subimage are removed.

6.2.3.3 Fine Refinement

In this step the boundary is refined at the pixel level in an iterative process. I first removed the effect of nuclei on the boundary evolution by replacing each nucleus region's pixels intensity by the mean intensity of its outer boundary. This smooths the segmented nuclei regions significantly and edge pixels caused by nuclei will not attract the boundaries.

While moving from a pixel outside the cell towards the centroid of its nucleus, a transition from a (relatively) bright to a darker pixel occurs at the time of entrance to the area of the cell (at the cytoplasm boundary). In the first phase of each iteration such locations are found. However, finding the correct locations is usually not an easy task because 1) these *edge* pixels are not always easily detectable because of low contrast and signal to noise ratio and also 2) the presence of artifacts and non-cervical cells create spurious edges. To

address the first issue, a smoothing filter is used that refines the transition locations using the calculated transition locations before and after them. This will ensure that if enough edge pixels are detected correctly a missing/incorrectly detected edge pixel will be recovered. To minimize the adverse affect of the spurious edges in the first phase of each iteration a *more rough* smoothing filter is used to smooth the values and those values that are further from their smoothed values than a threshold are considered outliers and are removed. The filter is applied again to the remaining values and the new estimated values are used to refine the boundary. Also, a weight vector is defined to give higher preference to edge pixels in the vicinity of the refined boundary at the previous iteration (or approximated boundary from previous coarse refinement step). The details are as follows.

Suppose that the boundary contains pixels of coordinates $(c_x + r_\theta \cos \theta, c_y + r_\theta \sin \theta)$, for $\theta = 0, 1, \dots, 359$, where (c_x, c_y) are the coordinates of the nucleus centroid. In the first iteration, for each $\theta \in \{0, 1, \dots, 359\}$, the weight vector is defined as

$$W_\theta = \left(\frac{1}{1 + \exp \left(-a \left(\frac{1}{2} - \frac{|r_\theta - s|}{r_\theta} \right) \right)} \right)_{s=0}^{2r_\theta}, \quad (6.7)$$

that contains the values of the composite of a sigmoid function with the normalized distance of points on the radial from the boundary point. A pixel corresponded to radius θ and stride s , p_θ^s , has the coordinates $(c_x + s \cos \theta, c_y + s \sin \theta)$. The gradient at p_θ^s , $G(p_\theta^s)$, is defined as

$$I(p_\theta^{s+1}) - I(p_\theta^{s-1}), \quad (6.8)$$

where $I(p)$ is the intensity of pixel p . For strides larger than $2r_\theta$ and for strides smaller than 0 the intensity is respectively set to maximum or minimum. For each $\theta \in \{0, 1, \dots, 359\}$, $p_\theta^{i_\theta}$

is selected as the edge pixel where

$$i_\theta = \arg \max_{s \in \{0,1,\dots,2\theta\}} W_\theta(s)G(p_{\theta,s}). \quad (6.9)$$

After choosing the sequence of points, $(p_\theta^{i_\theta})_{\theta=0}^{359}$, on the boundary the x -coordinates (and similarly y -coordinates independently) are smoothed by the Savitzky–Golay filter [185]. To filter out the spurious edge pixels after the first smoothing, those pixels that have a distance larger than a threshold from their smoothed estimation are discarded. The filter is applied again to the remaining points and the new smoothed boundary replaces the previous estimated boundary. This will minimize the effect of the spurious or inaccurately selected pixels on the boundary evolution. Fig. 6.4 shows how newly selected boundary points and smoothing affects the previous boundary of a cell in a synthetic image.

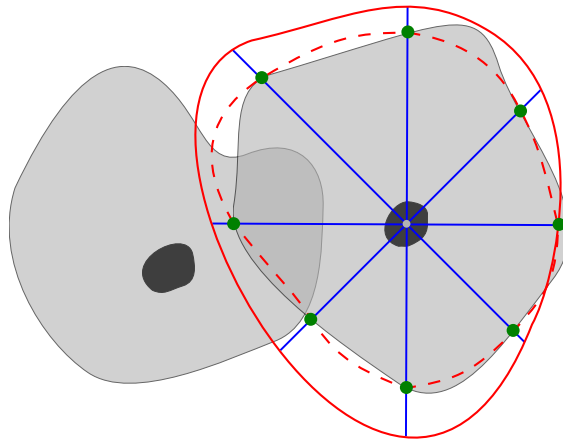


Figure 6.4: Fine refinement: the approximated boundary (red line) and the result (dashed red line) of selecting highest weighted gradient points on radials followed by Savitzky–Golay filter.

The only difference between the first iteration and the following iterations is that in the following iterations the strides in Eq. 6.7 are only considered from 0 through r_θ . Therefore, in the first iteration the area may grow but after that it only can shrink. Inflation in iterations other than the first iteration is restricted because, if there are no strong edge pixels due to very poor contrast the boundaries usually expand until they reach to the cell clump

boundary. The iterations are continued until the ratio of the size of non-overlapping area (between the new and previous areas) to the size of previous area is negligible (less than 0.01).

6.3 Datasets

The datasets that the framework is trained and tested on were provided in two ISBI challenges, the first and the second Overlapping Cervical Cytology Image Segmentation Challenge (2014 and 2015) [51, 177]. To the best of my knowledge, these are the only publicly available cervical cytology datasets that contain overlapping cells and their ground truth segmentation.

The first dataset (from the first challenge, ISBI 2014) contained 135 synthetic and 8 real cervical cytology EDF images in the training set and 810 synthetic and 8 real cervical cytology EDF images in the test set. The second dataset (from the second challenge, ISBI 2015) contained 8 real cervical cytology EDF images along with their volume images in the training set and 9 real cervical cytology EDF images along with their volume images in the test set. The main difference between the two datasets is the volume images that are included with the 2015 dataset. The synthetic images in the 2014 dataset were created by mirror transformations of background, and random rigid geometric and random linear brightness transforms of different annotated isolate cells in real EDF images [51]. The synthetic images have size 512x512 and each of them contains 2 to 10 different cells with varying overlapping ratios in different ranges: $[0, 0.1]$, $[0.1, 0.2]$, $[0.2, 0.3]$, $[0.3, 0.4]$, $[0.4, 0.5]$ [51], while real EDF images and the images in stacks have size 1024x1024.

Images in both datasets are accompanied by nucleus and cytoplasm annotation. Table 6.1 summarizes the number of annotated cells (nuclei and their corresponding cytoplasms) in each training and test sets of the two datasets. Note that because the annotation of individual cytoplasms of cells in the EDF images in ISBI 2014 dataset have not been released I did

not include them in Table 6.1 and they could not be used for the evaluation of cytoplasm segmentation.

Table 6.1: Number of annotated cells in training and test set of the datasets.

	ISBI 2014 dataset	ISBI 2015 dataset
Training set	810	320
Test set	4860	449

6.4 Results

Except for two parameters, the parameters in the framework were set either adaptively or empirically based on the image resolution and average brightness of a few typical images. For example, almost all nuclei have sizes larger than 115 and solidity larger than 0.91. Based on these observations, the parameters in the nucleus segmentation algorithm, such as minimum size, solidity, threshold ranges and minimum average intensity difference are set to 110, 0.9, [60, 150] and 15 in all experiments, respectively. Moreover, because in the third step (Section 6.2.3), a pixel is assigned to a cytoplasm only if it is contained in a segmented cell clump, I chose the values q (Eq. 6.1) and q' in a way that the foreground is not over-segmented. These values were set empirically to 0.06 and 0.0001. Different values of $q \in [0.01, 0.1]$ and different values of $q' \in [0.00001, 0.001]$ produce very similar results. Moreover, because the image sizes are powers of two I set W (introduced in Subsection 6.2.3.1) to $2^3 = 8$ as $W = 2$ or 4 worsened results and increased the computation time. Also, higher values (such as 16) of W make the boundary approximation inaccurate.

The only parameters that are searched and set based on the whole training set (separately for ISBI 2014 and ISBI 2015 datasets) are α and β in Eq. 6.4 and Eq. 6.6, respectively. Changing values for α or β *separately* can change the results significantly as they manage the overlapping degree of cytoplasm and the way subimages are assigned to different cells

cytoplasm. However, generally, if α is increased and β is decreased simultaneously (and vice versa) the produced result does not change significantly as it can be seen in Section 6.4.2. The process of setting the values of these two parameters is explained in detail in the following section.

I first discuss the evaluation parameters (Section 6.4.1) and then report the results of the framework on the ISBI 2015 dataset (Section 6.4.2) as the framework was originally proposed to work with the volume images that were not provided in the ISBI 2014 dataset. Finally, by a modification in the framework I also trained and tested it on ISBI 2014 dataset and the detailed results and discussion are presented in Section 6.4.3.

6.4.1 Evaluation Metrics

The Dice Similarity Coefficient (DSC) of two regions A and B is defined as

$$DSC_{A,B} = \frac{2|A \cap B|}{|A| + |B|}. \quad (6.10)$$

During evaluation a segmented cell in the ground truth is considered to be missed if there is no region in the segmentation result that has a DSC greater than 0.7 with it. The original evaluation metrics proposed in both challenges were DSC, False Negative Rate at object level (FNRo), True Positive Rate at pixel level (TPRp) and False Positive Rate at pixel level (FPRp). FNRo is the rate of cells missed in the ground truth as defined earlier and TPRp and FPRp are the average of true positive and false positive rates at the pixel level of those regions that are not missed. A typical cell is relatively small compared to the image size. Therefore, all previously reported results of different methods show a very small FPRp [51, 177, 178, 179, 172], typically less than 0.01. Hence, this measure does not effectively distinguish between the performance of different methods. Instead, I propose to report the False Discovery Rate at object level (FDRo). FDRo together with FNRo can give an assessment of the *detection performance* of different methods effectively. DSC is in fact the

F-measure at the pixel level:

$$\begin{aligned}
DSC_{A,B} &= \frac{2|A \cap B|}{|A| + |B|} \\
&= \frac{\frac{2|A \cap B|^2}{|A||B|}}{\frac{|A \cap B|(|A|+|B|)}{|A||B|}} \\
&= \frac{2 \frac{|A \cap B|}{|A|} \frac{|A \cap B|}{|B|}}{\frac{|A \cap B||A|}{|A||B|} + \frac{|A \cap B||B|}{|A||B|}} \\
&= \frac{2 \frac{|A \cap B|}{|A|} \frac{|A \cap B|}{|B|}}{\frac{|A \cap B|}{|B|} + \frac{|A \cap B|}{|A|}} \\
&= \frac{2RP}{P + R} \\
&= F_1,
\end{aligned} \tag{6.11}$$

where P and R are precision and recall considering A to be the ground truth region and B to be the segmented region. Therefore, the F -measure is commonly used for evaluating segmentation accuracy and therefore, the combination of DSC and TPRp can effectively evaluate the *segmentation accuracy* of different methods.

In experiments a segmentation is considered a *good* segmentation if it matches a region in ground truth with a DSC higher than 0.7 [51]. Otherwise, it is counted as a *bad* segmentation and therefore, a false discovery.

On a different note, unfortunately, because of an error in the original provided evaluation code in challenges I could not compare the method's results with most of the other proposed methods [177, 178, 179] fairly. It was observed that the original evaluation code may miss some *good* segmentations and therefore, the reported measures are not accurate. To deal with this issue, I implemented a new evaluation code computing the set of metrics described above and have made it publicly available for future evaluations on these or other datasets with ground truth¹. Because I had access to the source codes of the methods by Lu et al. [51]

¹http://www.csee.usf.edu/~hady/codes/2016_segmentation_evaluation.zip.

and Ushizima et al. [181] I could test their algorithms on both datasets and reevaluate their performance with the new evaluation code and metrics. I report their results in Section 6.4.3 for comparison (along with the previous version of the framework [172]). Note that both of their methods were originally proposed on the ISBI 2014 dataset whereas this approach was originally proposed on the ISBI 2015 dataset. All the results in Section 6.4.3 are obtained by setting the parameters based on the ISBI 2014 training set and testing them on the test sets of ISBI 2014 and ISBI 2015.

During experiments, it was observed that sometimes a marginally higher average DSC measure can be achieved with a relatively higher FNRo. As explained above, DSC and TPRp are measures of cell segmentation accuracy and FNRo and FDRo are measures of cell detection accuracy. Therefore, if only DSC is considered as a measure of performance, ignoring FNRo, only the segmentation accuracy is assessed and the detection accuracy of methods are ignored completely. Hence, I suggest using the Geometric Mean of DSC and True Positive Rate at the object level (TPRo), $GM = \sqrt{DSC(1 - FNRo)}$, as the final assessment measure. The GM measure actually combines one measure of segmentation accuracy with one measure of detection accuracy.

In the next section I report the framework’s result on the ISBI 2015 dataset and compare it to the previous version of the method (in [172]). In Section 6.4.3 I thoroughly analyze the framework results on both datasets and compare it to the method by Lu et al. [51] and Ushizima et al. [181].

6.4.2 Results on ISBI 2015 Dataset

The results presented in this section were produced by setting α and β using the training set from the ISBI 2015 dataset. I searched for the set of values for α and β that produced the highest GM in the training set. Ten different values for α ($\{1, 1.25, \dots, 3.25\}$) and 20 different values for β ($\{6, 7, \dots, 25\}$) were checked and the highest GM was obtained with

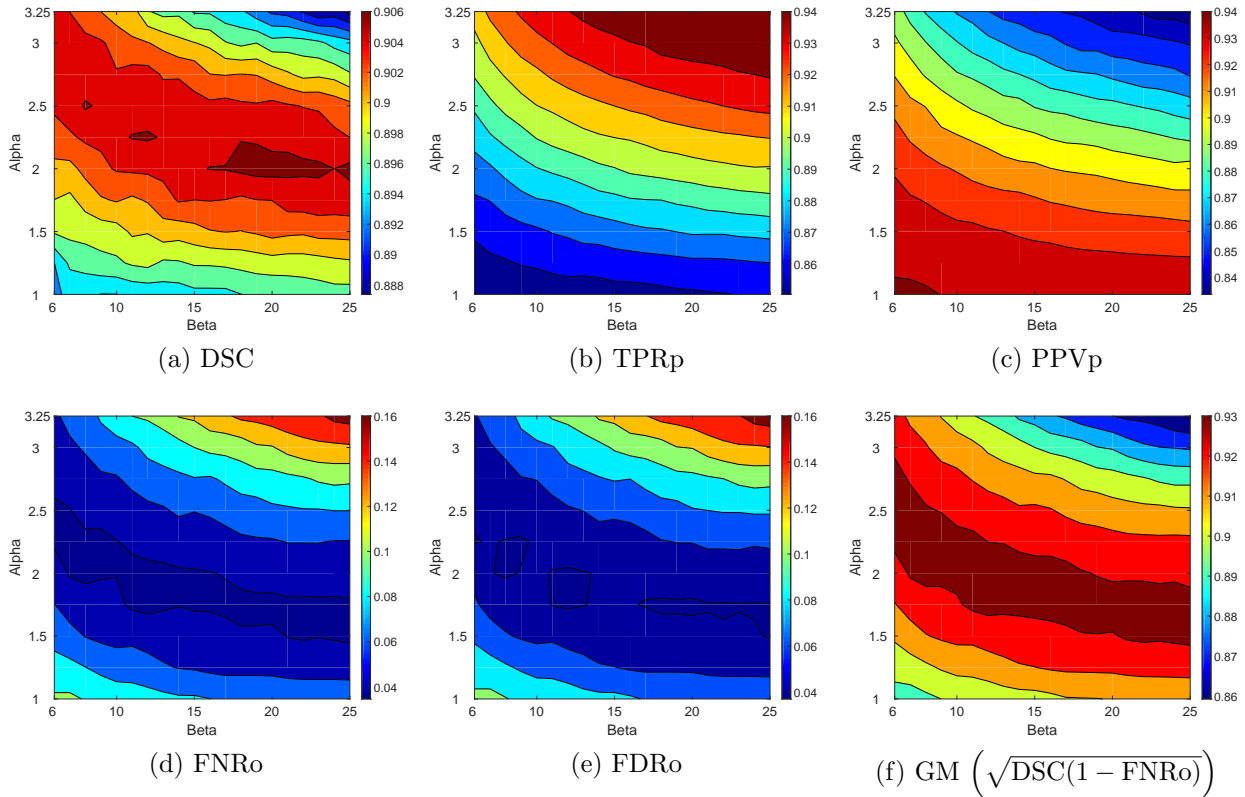


Figure 6.5: Visualization of results produced by different values of α and β .

$\alpha = 2.25$ and $\beta = 16$. Four sets of values producing the two highest GM, highest DSC and lowest FNRo and their corresponding results on the training set are summarized in Table 6.2². As can be seen marginally a higher DSC may be obtained for the cost of higher FNRo, and the GM measure is a good choice to optimize the algorithm parameters for both at the same time.

To show the importance of FDRo, it should be noted that usually reporting more regions in segmentation results in a higher DSC. To show this, I simply removed the solidity check in the nucleus segmentation algorithm. This will result in over-detecting nuclei in each image on average and hence, more regions will be reported in the final segmentation result. I set the α and β for this version separately and included its results in Table 6.3 that also compares the new results to those in [172] using the new evaluation code and metrics. It

²In each of the following tables superior results are shown with bold text.

Table 6.2: Four sets of values producing the two highest GM measures, highest DSC and lowest FNRo on training set of ISBI 2015 dataset.

α, β	DSC	FNRo	TPRp	FDRo	GM
2.25, 16	0.882	0.184	0.908	0.250	0.848
2, 25	0.884	0.188	0.907	0.253	0.847
3.25, 6	0.886	0.212	0.912	0.276	0.835
2, 9	0.876	0.181	0.875	0.247	0.847

shows that smaller FNRo and almost the same DSC can be achieved by reporting more regions (and leading to higher FDRo). However, this is not realistic as this version clearly segments significantly more nuclei than the number of nuclei in the ground truth. Therefore, it was concluded that one should strive for higher GM while keeping FDRo close to FNRo.

Table 6.3: Comparison between current version with previous version of the method [172] on test set of ISBI 2015 dataset.

	α, β	DSC	FNRo	TPRp	FDRo	GM
Previous Version [172]	2.25, 23	0.855	0.243	0.882	0.289	0.804
Improved version (nucleus over-detection)	2.75, 9	0.871	0.183	0.893	0.390	0.844
Improved version	2.25, 16	0.873	0.232	0.900	0.281	0.819

6.4.3 Comprehensive Results on Both Datasets

In this section I first report the results of the nucleus detection algorithm on the test set of the ISBI 2014 and compare it to other methods. In Subsection 6.4.3.2 I compare the framework’s results with those presented in [51] and [181].

Table 6.4: Detailed results of the framework on 810 synthetic images in the test set of the ISBI 2014 dataset. The results are presented in the format DSC, FNRo, TPRp, FDRo. O. is the overlap ratio.

	All overlaps	O. $\in [0, 0.1]$	O. $\in [0.1, 0.2]$	O. $\in [0.2, 0.3]$	O. $\in [0.3, 0.4]$	Overlap $\in [0.4, 0.5]$
All cells	.90, .07, .91, .04	.96, .02, .96, .01	.92, .03, .92, .02	.89, .04, .90, .03	.87, .11, .87, .07	.86, .16, .86, .09
2 cells	.93, .02, .94, .01	.96, .00, .97, .00	.93, .00, .95, .00	.92, .00, .92, .00	.91, .03, .92, .00	.91, .08, .92, .03
3 cells	.91, .06, .92, .03	.96, .02, .97, .00	.92, .02, .93, .00	.90, .00, .92, .00	.88, .13, .90, .08	.87, .11, .88, .06
4 cells	.91, .05, .92, .03	.96, .01, .96, .00	.94, .04, .94, .03	.90, .01, .91, .00	.89, .03, .89, .03	.85, .15, .87, .09
5 cells	.91, .07, .92, .04	.96, .02, .97, .00	.93, .01, .93, .00	.91, .04, .92, .01	.87, .13, .88, .10	.86, .14, .89, .07
6 cells	.90, .06, .90, .04	.96, .01, .95, .00	.91, .02, .91, .01	.90, .05, .91, .03	.87, .08, .86, .07	.85, .16, .86, .07
7 cells	.90, .07, .90, .04	.96, .02, .96, .00	.90, .03, .91, .02	.89, .06, .89, .03	.86, .11, .86, .05	.87, .10, .87, .07
8 cells	.90, .07, .90, .05	.96, .03, .96, .02	.92, .04, .93, .05	.89, .03, .88, .03	.87, .10, .87, .07	.84, .15, .83, .09
9 cells	.90, .08, .90, .05	.96, .01, .96, .01	.92, .03, .93, .03	.89, .02, .90, .01	.86, .10, .86, .08	.85, .23, .86, .13
10 cells	.90, .09, .90, .05	.96, .02, .96, .00	.92, .02, .93, .01	.89, .08, .89, .05	.86, .16, .87, .10	.85, .18, .85, .10

6.4.3.1 Nucleus Detection

A nucleus, represented by region A in ground truth, is considered to be detected, by region B in a segmentation result, if

$$\frac{|A \cap B|}{\max\{|A|, |B|\}} > 0.6. \quad (6.12)$$

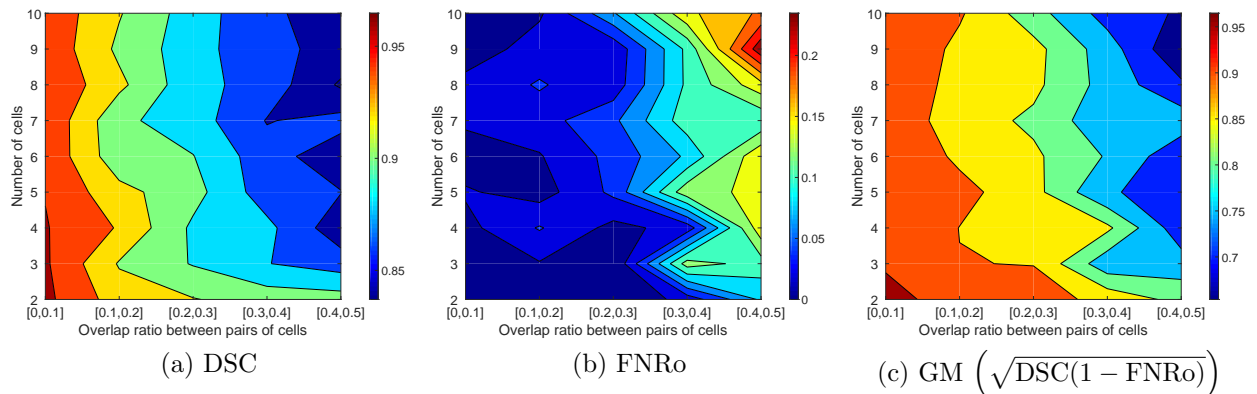


Figure 6.6: Visualization of results in Table 6.4.

Table 6.5 presents the nucleus detection algorithm results in terms of Precision, Recall and F-measure and compares it to the results presented in [177]. I also evaluated the nucleus detection algorithm presented in [172] on the test set of the ISBI 2014 dataset after setting its parameters using the training set of ISBI 2014 dataset. The nucleus detection algorithm achieves the highest Recall and F-measure while the method proposed by Lu et al. outperforms the proposed method in terms of Precision. Fig. 6.8 shows the nucleus segmentation result on some real EDF and synthetic images.

Table 6.5: Nucleus detection methods results on 810 synthetic images in the test set of ISBI 2014 dataset.

	Precision	Recall	F-measure
Ushizima et al. [181]	0.959	0.895	0.926
Nosrati et al. [177]	0.903	0.893	0.898
Lu et al. [177]	0.977	0.883	0.928
Phoulady et al. [172]	0.874	0.930	0.901
New Results	0.961	0.933	0.947

6.4.3.2 Cell Detection and Segmentation

The framework was originally proposed for the ISBI 2015 challenge and works with the image stacks along with the EDF images. However, only the third step (described in Subsection 6.2.3.1) to segment overlapping cytoplasm works with the volume images. Therefore, it can be modified to work only with the EDF images by excluding the focus distance (Eq. 6.2) effect on the boundary approximation process (Eq. 6.4). By doing so I could train the framework on the ISBI 2014 dataset that did not contain the image stacks and test it on the test set of both datasets.

Similar to the previous section, Table 6.6 presents the results of four sets of values for α and β .

Table 6.6: Four sets of values producing the two highest GM measures, highest DSC and lowest FNRo on the training set of ISBI 2014 dataset.

α, β	DSC	FNRo	TPRp	FDRo	GM
1.75, 20	0.904	0.035	0.892	0.037	0.934
2, 12	0.904	0.036	0.893	0.038	0.934
2, 20	0.907	0.049	0.906	0.052	0.928
1.75, 20	0.904	0.035	0.892	0.037	0.934

Fig. 6.5 presents a visualization of how the measures change by changing α and β . It seems that α and β correlate with each other somewhat linearly. This means that potentially the number of parameters that need to be set in the framework can be reduced to only one. TPR_p and Positive Predictive Value at the pixel level (PPV_p) seems to be correlated negatively, and DSC, which is the harmonic mean of the two, attains its largest values in the middle band. Finally, there is a large set of parameters that produce similar superior results (the middle band in Fig. 6.5f).

Using the parameters set by the training set from the ISBI 2014 dataset ($\alpha = 1.75$ and $\beta = 20$) I tested the framework on both testing sets and compared to the method by Lu et al. [51] in Table 6.7. The proposed method outperforms the method in [51] by having significantly lower FNR_o and FDR_o and marginally better DSC. However, it has marginally worse TPR_p. Moreover, the proposed method achieves marginally better results using the parameters set by ISBI 2014 training set compared to the results achieved by the parameters set by ISBI 2015 training set.

Table 6.7: Results of the framework and comparison with the other state-of-the-art methods.

	DSC	FNR _o	TPR _p	FDR _o	GM
Lu et al. [51]	0.887	0.229	0.907	0.146	0.827
Ushizima et al. [181]	0.868	0.209	0.842	0.152	0.829
Phoulady et al. [172]	0.883	0.087	0.902	0.142	0.898
New Results	0.901	0.070	0.906	0.041	0.915

(a) Results on 810 synthetic images in the test set of ISBI 2014 dataset

	DSC	FNR _o	TPR _p	FDR _o	GM
Lu et al. [51]	0.856	0.392	0.892	0.371	0.721
Ushizima et al. [181]	0.841	0.499	0.828	0.473	0.649
Phoulady et al. [172]	0.856	0.236	0.878	0.342	0.809
New Results	0.869	0.209	0.876	0.260	0.829

(b) Results on 9 real EDF images the test set of ISBI 2015 dataset

The test set of ISBI 2014 dataset is also accompanied by the number of cells and their overlap ratio in each image. This enables us to produce detailed results on this dataset as presented in Table 6.4. The results contain the detection and segmentation accuracy for different subsets of the whole test set as the number of cells and overlap ratio vary.

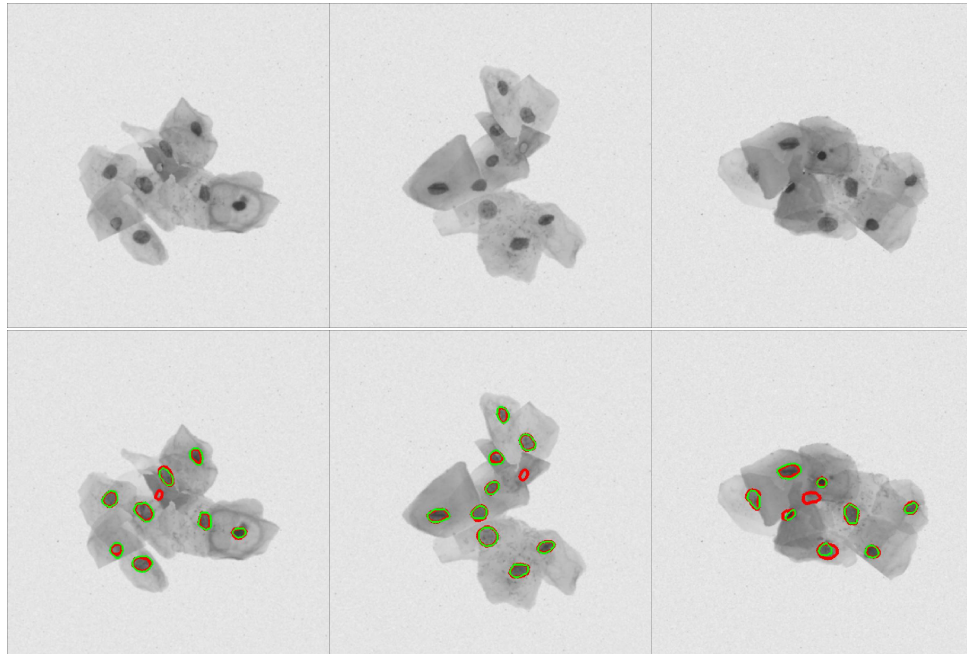


Figure 6.7: Five images with very low contrast nuclei (red and green lines are ground truth and segmentation region boundaries, respectively).

6.5 Discussions

Table 6.4 shows that when there are only 2 cells in an image the method misses only around 2 percents of cells and it does not miss any cells if the overlap ratio is less than 0.3. Also, when the overlap is low (in $[0, 0.1]$ range) only 2% of cells are missed on average in all images containing up to 10 cells. The highest miss ratio is for 9 cells with the highest overlap ratio ($[0.4, 0.5]$). The method misses less than 5% of all cells, if the pairwise overlap ratio is less than 0.3. But it quickly increases to around 10% when the overlap ratio is in the interval $[0.3, 0.4]$. Finally, when the overlap is highest, $[0.4, 0.5]$, the method misses 16%

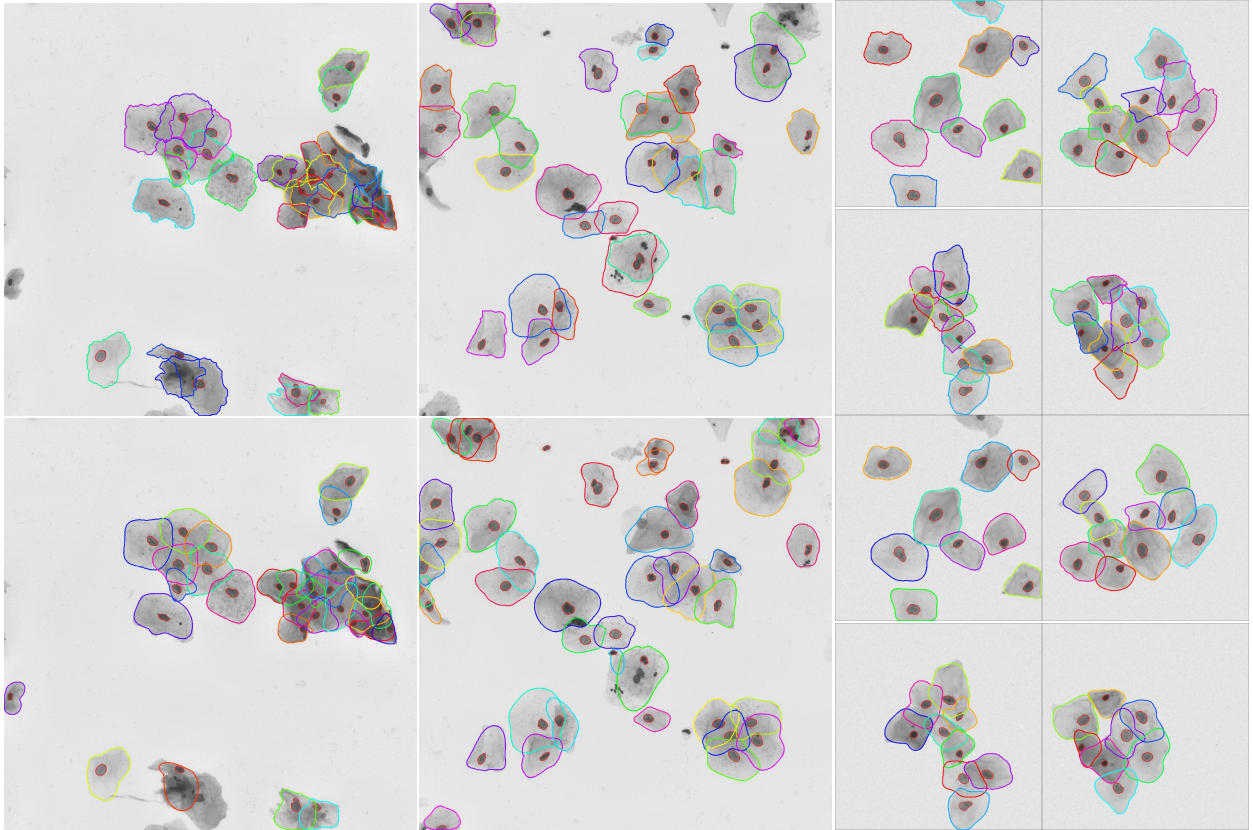


Figure 6.8: The ground truth (top row) and the nucleus and overlapping cells segmentation results of two real EDF and four synthetic images with nucleus.

of cells on average. Fig. 6.6 shows a visualization of results in Table 6.4. It shows that the mean DSC changes more uniformly than FNRo. Upon investigation I noticed that some of the cells are missed because of missed nuclei. In some synthetic images some nuclei do not have high contrast or even look brighter than their adjacent regions. Fig. 6.7 shows three such images. However, the number of such nuclei in images seem to be relatively low. Also, even if the nuclei are detected and segmented correctly, the boundaries may not be found effectively if the overlapping degree is very high and/or there are very little useful image information for the boundaries (one such example can be seen in the first EDF image in Fig. 6.8). On the other hand, around 70% of cell clumps in real images contain three or fewer cells [176]. Therefore, this issue does not happen frequently in real situations and the EDF images seem to be a good representation of the real environment. Moreover, on

both datasets, the boundary refinement steps improved the FNRo by around 5-10% based on different parameters (compared to when only the boundary approximation is used without any refinement). Fig. 6.8 shows some final segmentation results on real and synthetic images.

The Matlab code was run on a PC with 3.60 GHz i7-4790 processor and 16 GB of RAM. The processing *on a real EDF image* takes around 10 seconds on average: it takes around 2.5 seconds for the algorithm to detect and segment nuclei and cell clumps and around 7.5 seconds to segment the overlapping cell cytoplasm. A synthetic image, on the other hand, takes around 0.5 seconds on average. This indicates that the framework is at least 10 times faster than the fastest method evaluated in [177] on synthetic images. Processing an EDF image takes almost 20 times longer than a synthetic image as an EDF image is 4 times larger than a synthetic image and has around 8 times more cells on average.

6.6 Summary

A framework was proposed to segment the overlapping cytoplasm in cervical cytology images. In all three main steps (nucleus detection and segmentation, cell clump segmentation and overlapping cytoplasm segmentation) of the framework novel approaches were proposed.

The nucleus detection and segmentation method proposed in this work is substantially different from that proposed in [172]. It uses solidity as the main feature of nuclei regions and is more resistant to brightness changes in images and produces more consistent results. However, it tends to over-segment nuclei regions. Quantitative (Table 6.5) and qualitative (Fig. 6.8) results show that it can find nuclei regions in both synthetic and real images with high accuracy and it outperforms other existing methods on the same dataset. Cell clump segmentation is done accurately by learning a GMM over pixel intensities using the EM algorithm. Qualitative results of the segmentations in this step show that it only misses very small areas that have very low contrast. The cytoplasm segmentation for each detected nucleus was done by boundary approximation on the subimage followed by two refinement steps

at the subimage and pixel level. The proposed outliers removal procedure could effectively reduce the effect of outliers on boundary evolution.

The final results show that on synthetic images the framework misses only 7% of 4860 cells in 810 images that each contained 2-10 cells, and on real EDF images it misses around 20% of all cells. The detailed results in Table 6.4 show that the framework missed less than 5% of cells when the pairwise overlapping was not higher than 0.3 (in $[0, 0.3]$ range) and it missed around 20% of cells when there are 9-10 cells in images and the pairwise overlapping is very high (in $[0.4, 0.5]$ range). The method outperforms the other methods proposed on the same dataset [51] by a large margin (Table 6.7) in terms of False Negative Rate at object level while achieving higher Dice Similarity Coefficient. This shows a promising breakthrough in the challenging task of overlapping cytoplasm segmentation of cervical cells in cytology images.

Chapter 7

Conclusions

7.1 Summary

In Chapter 1, I discussed the motivation and background on CAD systems and the major approaches of CAD systems that process bright-field microscopy images.

In Chapter 2 the recent advances in microscopy image processing were investigated and some of the most recent and/or popular algorithms for nucleus detection and segmentation and cervical cell segmentation were reviewed. Most of the work in microscopy image processing is done on histology, specifically breast histology images. On the other hand, most of the researches on cytology are on cervical cytology segmentation. Cervical cytology segmentation, compared to breast histology segmentation, is a relatively less studied topic. However, more work has focused on it during the past few years. I divided the reviewed methods for nucleus segmentation into five main categories. Some methods, such as level set methods, mostly give more accurate segmentations but they are computationally intensive and are parameter sensitive. Some other methods, e.g. intensity based approaches, are faster but may give less accurate segmentations. Generally speaking, there is no known *optimal* type of method for medical image segmentation and to design and propose an algorithm one needs to take tissue type, slide preparation process and final goal¹ into considerations. Finally, although earlier methods of cervical cell segmentation focused primarily on segmenting free lying cells, more recent algorithms tackle the most challenging task of segmenting overlapping cells.

¹E.g., Is the final goal achieving a good segmentation or detecting specific regions in whole slides? Do we want to do classification? etc.

In Chapters 3, 4, 5 and 6, the methods that were published and were proposed for different tasks of segmentation and classification were presented. In Chapter 3, a segmentation method was presented that was proposed to segment nuclei in histology images of various tissues. In Chapters 4 and 5, two novel methods for cervical tissue classification using histology images were presented. These methods used the MNV and texture features, respectively, to classify tissues and could achieve high classification accuracies (84% and 93%). In Chapter 6, a robust framework was presented to segment overlapping cervical cells in cervical volume images and their corresponding EDF image.

7.2 Contributions

In Chapter 3, a general segmentation methods for segmenting nuclei in histology images was presented. While the algorithm achieved higher accuracy measures, it does not need any training data to learn or tune the parameters as they are adaptively set based on the data. It was shown that competitive results can be obtained by the proposed framework that adaptively sets the method parameters. This makes the algorithm more practical in real situations and makes it more expandable to other datasets.

In Chapter 4, an ensemble approach was proposed to classify cervical tissues using histology images. Four basic segmentors with different parameters settings were used to produce different segmentation of the same images. In an ensemble approach these segmentation results were combined to give the final value for the Mean Nuclear Volume (MNV) of each tissue. An extra step was also designed to identify and reject those cases that were not *reliably* processed. The results showed that the single feature of MNV can be used to classify tissues with high accuracy (over 84%). The work was one of the few works that investigated the effectiveness of an automatically computed MNV feature for the task of cervical tissue classification.

In Chapter 5, a framework (Adaptive Nucleus Shape Modeling) that was used to do the similar task of classifying cervical tissues (as Chapter 4) was presented. In that work, instead of using MNV as the feature, nucleus level texture features were extracted and used for classification. The images were first segmented using a new segmentation algorithm and the segmentation results were enhanced using ellipse fitting. This method further increased the accuracy of cervical tissue classification (from 84% to 93%) that was obtained by previous method. Furthermore, it does not reject any cases from processing and it overcame the limitation of missed nuclei labeling information by removing poorly segmented nuclei and reducing the number of mislabeled training instances. It also outperformed the results obtained by employing one of the state-of-the-art segmentation algorithms. It was shown that for the task of classification, a more simple segmentation algorithm can potentially produce marginally better results.

In Chapter 6, a framework was proposed to segment overlapping cervical cells in Pap smear cervical cytology images. Segmentation of overlapping cervical cells is a challenging task due to artifacts and overlapping cytoplasm. The main three steps of the algorithm were nucleus segmentation, cell clump segmentation and overlapping cytoplasm segmentation. Moreover, the proposed nucleus segmentation method was a novel iterative thresholding algorithm that outperformed other state-of-the-art nucleus segmentation methods in terms of detection accuracy. The cell clump segmentation was done efficiently and accurately by using a learned GMM to choose the thresholding parameter. Cervical volume stack images were used to approximate the cytoplasm boundary by using a novel focus vector. As the final step to refine the cytoplasm boundary a weight vector along radial pixels was proposed that could be used efficiently to find the correct edge pixels to fit the previously approximated boundary to real cell boundary. It was the first method that used the information in cervical volume images efficiently to increase the segmentation accuracy. It could improve the results of previous state-of-the-art algorithms substantially: the best results obtained by a method

on ISBI 2015 dataset showed around 40% missed cells while the proposed method missed only around 20% cells, which is a huge improvement. It also runs very fast and experiments showed that it can process images more than 10 times faster than other methods.

7.3 Future Directions

Several algorithms were proposed to segment nuclei and classify tissues using microscopy bright-field images. These methods can potentially be improved as discussed below.

1. The results obtained by the hierarchical multilevel thresholding algorithm (Chapter 3) can be potentially improved by an extra post-processing step to separate overlapping nuclei which is the main source of the error in the final segmentation result. Algorithms that aim to separate segmented overlapping regions can be employed for this purpose.
2. The classification accuracy of the framework proposed in Chapter 4 can be potentially increased by replacing the segmentors by more advanced segmentation algorithms. The computation of MNV is strictly dependent on the segmented regions. Therefore, segmented overlapping regions and under-segmented regions can adversely affect the final computed feature. A new extra step can be developed to eliminate such incorrectly segmented regions and potentially improve the accuracy of final computed MNV feature.
3. The method proposed in Chapter 5 can be potentially improved by extracting other image features other than texture features. A subset of the set of new features can be chosen by employing a feature selection approach to remove the less discriminatory features.
4. The segmentation method presented in Chapter 6 can be potentially improved by a few modifications: 1) although the nucleus segmentation algorithm outperforms other methods in terms of detection accuracy, it is still one of the major sources of error in the

final results. Because when a nucleus is missed, the framework does not have the chance of segmenting the cell as they are the seed points for different cells. The algorithm can be potentially improved by first over-detecting nuclei and then classifying them as nucleus or non-nucleus. Also, an ensemble algorithm can be used to potentially reduce the miss rate; 2) most of the inaccuracies in the final segmentation results happen when the overlapping degree is very high (greater than 40%). These areas can be detected (by checking the density of detected nuclei in different regions) and can be processed in a different way or with different method parameters.

References

- [1] M.T. McCann, J.A. Ozolek, C.A. Castro, B. Parvin, and J. Kovacevic. Automated histology analysis: Opportunities for signal processing. *Signal Processing Magazine, IEEE*, 32(1):78–87, Jan 2015. ISSN 1053-5888. doi: 10.1109/MSP.2014.2346443.
- [2] Best Doctors and the National Coalition on Health Care. Exploring diagnostic accuracy in cancer: A nationwide survey of 400 leading cancer specialists, 2012.
- [3] Robert Kelley. Where can \$700 billion in waste be cut annually from the us healthcare system. *Ann Arbor, MI: Thomson Reuters*, 24, 2009.
- [4] M.N. Gurcan, L.E. Boucheron, A. Can, A. Madabhushi, N.M. Rajpoot, and B. Yener. Histopathological image analysis: A review. *Biomedical Engineering, IEEE Reviews in*, 2:147–171, 2009. ISSN 1937-3333. doi: 10.1109/RBME.2009.2034865.
- [5] M. Veta, J.P.W. Pluim, P.J. van Diest, and M.A. Viergever. Breast cancer histopathology image analysis: A review. *Biomedical Engineering, IEEE Transactions on*, 61(5):1400–1411, May 2014. ISSN 0018-9294. doi: 10.1109/TBME.2014.2303852.
- [6] Shishir Shah and Edgar Gabriel. 2. image computing for digital pathology. In *Pattern Recognition, 2008. ICPR 2008. 19th International Conference on*, pages 1–1. IEEE, 2008.
- [7] American Cancer Society. Cancer facts & figures 2016. Atlanta: American Cancer Society, 2016.
- [8] Bernard W Stewart, Christopher P Wild, et al. *World cancer report 2014*. IARC Press, International Agency for Research on Cancer, 2014.
- [9] American Cancer Society. Cancer prevention & early detection facts & figures 2015-2016. Atlanta: American Cancer Society, 2015.
- [10] Ciaran BJ Woodman, Stuart I Collins, and Lawrence S Young. The natural history of cervical HPV infection: unresolved issues. *Nature Reviews Cancer*, 7(1):11–22, 2007.
- [11] Mark Schiffman, Philip E Castle, Jose Jeronimo, Ana C Rodriguez, and Sholom Wacholder. Human papillomavirus and cervical cancer. *The Lancet*, 370(9590):890–907, 2007. ISSN 0140-6736. doi: [http://dx.doi.org/10.1016/S0140-6736\(07\)61416-0](http://dx.doi.org/10.1016/S0140-6736(07)61416-0).
- [12] John HF Smith. Cytology, liquid-based cytology and automation. *Best Practice & Research Clinical Obstetrics & Gynaecology*, 25(5):585–596, 2011.

- [13] K Hagedorn, S Krämer, M Mitze, C Breuel, R Schulz-Wendtland, W Bautz, and N Lang. [interventional methods in breast diagnosis. histological vs. cytological evaluation of core cut biopsies of the breast]. *Aktuelle Radiologie*, 8(6):278–282, 1998.
- [14] Pablo Moura de Andrade Lima, Marcelo Parente Oliveira, George Rocha Ferreira, Túlio Paes de Medeiros Lima, Jairo de Andrade Lima, and Roberto José Vieira de Mello. Effectiveness of histology and cytology on musculoskeletal tumor diagnosis. *Acta ortopedica brasileira*, 22(3):132–135, 2014.
- [15] Raphael Rubin, David S Strayer, Emanuel Rubin, et al. *Rubin’s pathology: clinico-pathologic foundations of medicine*. Lippincott Williams & Wilkins, 2008.
- [16] Arnout C Ruifrok and Dennis A Johnston. Quantification of histochemical staining by color deconvolution. *Analytical and quantitative cytology and histology/the International Academy of Cytology [and] American Society of Cytology*, 23(4):291–299, 2001.
- [17] E. Reinhard, M. Adhikhmin, B. Gooch, and P. Shirley. Color transfer between images. *Computer Graphics and Applications, IEEE*, 21(5):34–41, Sep 2001. ISSN 0272-1716. doi: 10.1109/38.946629.
- [18] A. M. Khan, N. Rajpoot, D. Treanor, and D. Magee. A nonlinear mapping approach to stain normalization in digital histopathology images using image-specific color deconvolution. *Biomedical Engineering, IEEE Transactions on*, 61(6):1729–1738, June 2014. ISSN 0018-9294. doi: 10.1109/TBME.2014.2303294.
- [19] S. Naik, S. Doyle, S. Agner, A. Madabhushi, M. Feldman, and J. Tomaszewski. Automated gland and nuclei segmentation for grading of prostate and breast cancer histopathology. In *Biomedical Imaging: From Nano to Macro, 2008. ISBI 2008. 5th IEEE International Symposium on*, pages 284–287, May 2008. doi: 10.1109/ISBI.2008.4540988.
- [20] S. Kothari, J.H. Phan, R.A. Moffitt, T.H. Stokes, S.E. Hassberger, Q. Chaudry, A.N. Young, and M.D. Wang. Automatic batch-invariant color segmentation of histological cancer images. In *Biomedical Imaging: From Nano to Macro, 2011 IEEE International Symposium on*, pages 657–660, March 2011. doi: 10.1109/ISBI.2011.5872492.
- [21] Jelte Peter Vink, MB Van Leeuwen, CHM Van Deurzen, and G De Haan. Efficient nucleus detector in histopathology images. *Journal of microscopy*, 249(2):124–135, 2013.
- [22] Mitko Veta, Paul J van Diest, Robert Kornegoor, André Huisman, Max A Viergever, and Josien PW Pluim. Automatic nuclei segmentation in h&e stained breast cancer histopathology images. *PLoS One*, 8(7):e70221, July 2013.

- [23] A.N. Basavanhally, S. Ganesan, S. Agner, J.P. Monaco, M.D. Feldman, J.E. Tomaszewski, G. Bhanot, and A. Madabhushi. Computerized image-based detection and grading of lymphocytic infiltration in her2+ breast cancer histopathology. *Biomedical Engineering, IEEE Transactions on*, 57(3):642–653, March 2010. ISSN 0018-9294. doi: 10.1109/TBME.2009.2035305.
- [24] P. Bamford and B. Lovell. Method for accurate unsupervised cell nucleus segmentation. In *Engineering in Medicine and Biology Society, 2001. Proceedings of the 23rd Annual International Conference of the IEEE*, volume 3, pages 2704–2708 vol.3, 2001. doi: 10.1109/IEMBS.2001.1017341.
- [25] Xin Qi, Fuyong Xing, D.J. Foran, and Lin Yang. Robust segmentation of overlapping cells in histopathology specimens using parallel seed detection and repulsive level set. *Biomedical Engineering, IEEE Transactions on*, 59(3):754–765, March 2012. ISSN 0018-9294. doi: 10.1109/TBME.2011.2179298.
- [26] H. Fatakdawala, Jun Xu, A. Basavanhally, G. Bhanot, S. Ganesan, M. Feldman, J.E. Tomaszewski, and A. Madabhushi. Expectation–maximization-driven geodesic active contour with overlap resolution (emagacor): Application to lymphocyte segmentation on breast cancer histopathology. *Biomedical Engineering, IEEE Transactions on*, 57(7):1676–1689, July 2010. ISSN 0018-9294. doi: 10.1109/TBME.2010.2041232.
- [27] Gang Li, Tianming Liu, J Nie, L Guo, J Chen, J Zhu, W Xia, A Mara, S Holley, and STC Wong. Segmentation of touching cell nuclei using gradient flow tracking. *Journal of Microscopy*, 231(1):47–58, 2008.
- [28] Cigdem Demir and Bülent Yener. Automated cancer diagnosis based on histopathological images: a systematic survey. *Rensselaer Polytechnic Institute, Tech. Rep*, 2005.
- [29] H. Irshad, A. Veillard, L. Roux, and D. Racoceanu. Methods for nuclei detection, segmentation, and classification in digital histopathology: A review–current status and future potential. *Biomedical Engineering, IEEE Reviews in*, 7:97–114, 2014. ISSN 1937-3333. doi: 10.1109/RBME.2013.2295804.
- [30] Adnan M Khan. *Algorithms for breast cancer grading in digital histopathology images*. PhD thesis, University of Warwick, United Kingdom, 2014.
- [31] Mitko Veta. *Breast Cancer Histopathology Image Analysis*. PhD thesis, Utrecht University, The Netherlands, 2014.
- [32] M.N. Gurcan, T. Pan, H. Shimada, and J. Saltz. Image analysis for neuroblastoma classification: Segmentation of cell nuclei. In *Engineering in Medicine and Biology Society, 2006. EMBS '06. 28th Annual International Conference of the IEEE*, pages 4844–4847, Aug 2006. doi: 10.1109/IEMBS.2006.260837.

- [33] Stephan Wienert, Daniel Heim, Kai Saeger, Albrecht Stenzinger, Michael Beil, Peter Hufnagl, Manfred Dietel, Carsten Denkert, and Frederick Klauschen. Detection and segmentation of cell nuclei in virtual microscopy images: a minimum-model approach. *Scientific reports*, 2:503, 2012.
- [34] Ge Cong and Bahram Parvin. Model-based segmentation of nuclei. *Pattern Recognition*, 33(8):1383 – 1393, 2000. ISSN 0031-3203. doi: [http://dx.doi.org/10.1016/S0031-3203\(99\)00119-3](http://dx.doi.org/10.1016/S0031-3203(99)00119-3).
- [35] Daniela M Ushizima, Andrea G C Bianchi, and Claudia M Carneiro. Segmentation of subcellular compartments combining superpixel representation with voronoi diagrams. Overlapping Cervical Cytology Image Segmentation Challenge, IEEE ISBI, Beijing, China, April 2014. 1st Place.
- [36] G. L. B. Ramalho, D. S. Ferreira, A. G. C. Bianchi, C. M. Carneiro, F. N. S. Medeiros, and D. M. Ushizima. Cell reconstruction under voronoi and enclosing ellipses from 3d microscopy. The Second Overlapping Cervical Cytology Image Segmentation Challenge, IEEE ISBI, Brooklyn, NY, March 2015.
- [37] Sokol Petushi, C. Katsinis, C. Coward, F. Garcia, and A. Tozeren. Automated identification of microstructures on histology slides. In *Biomedical Imaging: Nano to Macro, 2004. IEEE International Symposium on*, pages 424–427 Vol. 1, April 2004. doi: 10.1109/ISBI.2004.1398565.
- [38] U. Adiga, R. Malladi, R. Fernandez-Gonzalez, and C.O. de Solorzano. High-throughput analysis of multispectral images of breast cancer tissue. *Image Processing, IEEE Transactions on*, 15(8):2259–2268, Aug 2006. ISSN 1057-7149. doi: 10.1109/TIP.2006.875205.
- [39] Norberto Malpica, Carlos Ortiz de Solorzano, Juan José Vaquero, Andrés Santos, Isabel Vallcorba, José Miguel Garcia-Sagredo, and Francisco del Pozo. Applying watershed algorithms to the segmentation of clustered nuclei. *Cytometry*, 28:289–29, 1997.
- [40] Roman Stoklasa, Lukáš Bálek, Pavel Krejčí, Petr Matula, et al. Automated cell segmentation in phase-contrast images based on classification and region growing. In *Biomedical Imaging (ISBI), 2015 IEEE 12th International Symposium on*, pages 1447–1451, April 2015. doi: 10.1109/ISBI.2015.7164149.
- [41] Mitko Veta, A Huisman, Max A Viergever, Paul J van Diest, and Josien PW Pluim. Marker-controlled watershed segmentation of nuclei in h&e stained breast cancer biopsy images. In *Biomedical Imaging: From Nano to Macro, 2011 IEEE International Symposium on*, pages 618–621. IEEE, 2011.
- [42] Aslı Gençtav, Selim Aksoy, and Sevgen Önder. Unsupervised segmentation and classification of cervical cell images. *Pattern Recognition*, 45(12):4151–4168, 2012. ISSN 0031-3203. doi: <http://dx.doi.org/10.1016/j.patcog.2012.05.006>.

- [43] Asli Gençtav and Selim Aksoy. Segmentation of cervical cell images. In *Pattern Recognition (ICPR), 2010 20th International Conference on*, pages 2399–2402. IEEE, 2010.
- [44] F. Cloppet and A. Boucher. Segmentation of overlapping/aggregating nuclei cells in biological images. In *Pattern Recognition, 2008. ICPR 2008. 19th International Conference on*, pages 1–4, Dec 2008. doi: 10.1109/ICPR.2008.4761451.
- [45] Chanhong Jung and Changick Kim. Segmenting clustered nuclei using h-minima transform-based marker extraction and contour parameterization. *Biomedical Engineering, IEEE Transactions on*, 57(10):2600–2604, Oct 2010. ISSN 0018-9294. doi: 10.1109/TBME.2010.2060336.
- [46] S. Ali and A. Madabhushi. An integrated region-, boundary-, shape-based active contour for multiple object overlap resolution in histological imagery. *Medical Imaging, IEEE Transactions on*, 31(7):1448–1460, July 2012. ISSN 0278-0062. doi: 10.1109/TMI.2012.2190089.
- [47] Jun Xu, Andrew Janowczyk, Sharat Chandran, and Anant Madabhushi. A weighted mean shift, normalized cuts initialized color gradient based geodesic active contour model: applications to histopathology image segmentation. In *SPIE Medical Imaging*, pages 76230Y–76230Y. International Society for Optics and Photonics, 2010.
- [48] Adel Hafiane, Filiz Bunyak, and Kannappan Palaniappan. Fuzzy clustering and active contours for histopathology image segmentation and nuclei detection. In *Advanced concepts for intelligent vision systems*, pages 903–914. Springer, 2008.
- [49] Jun Kong, Fusheng Wang, G. Teodoro, Yanhui Liang, Yangyang Zhu, C. Tucker-Burden, and D.J. Brat. Automated cell segmentation with 3d fluorescence microscopy images. In *Biomedical Imaging (ISBI), 2015 IEEE 12th International Symposium on*, pages 1212–1215, April 2015. doi: 10.1109/ISBI.2015.7164091.
- [50] Huiyu Zhou, Xuelong Li, Gerald Schaefer, M. Emre Celebi, and Paul Miller. Mean shift based gradient vector flow for image segmentation. *Computer Vision and Image Understanding*, 117(9):1004 – 1016, 2013. ISSN 1077-3142. doi: <http://dx.doi.org/10.1016/j.cviu.2012.11.015>.
- [51] Zhi Lu, G. Carneiro, and A.P. Bradley. An improved joint optimization of multiple level set functions for the segmentation of overlapping cervical cells. *Image Processing, IEEE Transactions on*, 24(4):1261–1272, April 2015. ISSN 1057-7149. doi: 10.1109/TIP.2015.2389619.

- [52] Zhi Lu, Gustavo Carneiro, and Andrew P. Bradley. Automated nucleus and cytoplasm segmentation of overlapping cervical cells. In Kensaku Mori, Ichiro Sakuma, Yoshinobu Sato, Christian Barillot, and Nassir Navab, editors, *Medical Image Computing and Computer-Assisted Intervention MICCAI 2013*, volume 8149 of *Lecture Notes in Computer Science*, pages 452–460. Springer Berlin Heidelberg, 2013. ISBN 978-3-642-40810-6. doi: 10.1007/978-3-642-40811-3_57.
- [53] M.S. Nosrati and G. Hamarneh. Segmentation of overlapping cervical cells: A variational method with star-shape prior. In *Biomedical Imaging (ISBI), 2015 IEEE 12th International Symposium on*, pages 186–189. IEEE, April 2015. doi: 10.1109/ISBI.2015.7163846.
- [54] Andreas Kårsnäs, Anders L Dahl, and Rasmus Larsen. Learning histopathological patterns. *Journal of pathology informatics*, 2, 2011.
- [55] Antoine Veillard, Maria Kulikova, and Daniel Racoceanu. Cell nuclei extraction from breast cancer histopathology images using color, texture, scale and shape information. In *11th European Congress on Telepathology and 5th International Congress on Virtual Microscopy*, 2012.
- [56] R. Shenoy, Min-Chi Shih, and K. Rose. A probabilistic framework for simultaneous segmentation and classification of multiple cells in multi-marker microscopy images. In *Biomedical Imaging (ISBI), 2015 IEEE 12th International Symposium on*, pages 1224–1227, April 2015. doi: 10.1109/ISBI.2015.7164094.
- [57] Adnan M Khan, Hesham El-Daly, and Nasir M Rajpoot. A gamma-gaussian mixture model for detection of mitotic cells in breast cancer histopathology images. In *Pattern Recognition (ICPR), 2012 21st International Conference on*, pages 149–152. IEEE, 2012.
- [58] Hang Chang, Ju Han, A. Borowsky, L. Loss, J.W. Gray, P.T. Spellman, and B. Parvin. Invariant delineation of nuclear architecture in glioblastoma multiforme for clinical and molecular association. *Medical Imaging, IEEE Transactions on*, 32(4):670–682, April 2013. ISSN 0278-0062. doi: 10.1109/TMI.2012.2231420.
- [59] Vinh-Thong Ta, Olivier Lézoray, Abderrahim Elmoataz, and Sophie Schüpp. Graph-based tools for microscopic cellular image segmentation. *Pattern Recognition*, 42(6):1113–1125, 2009.
- [60] E. Poulain, S. Prigent, E. Soubies, and X. Descombes. Cells detection using segmentation competition. In *Biomedical Imaging (ISBI), 2015 IEEE 12th International Symposium on*, pages 1208–1211, April 2015. doi: 10.1109/ISBI.2015.7164090.
- [61] J. Wang, J.D. MacKenzie, R. Ramachandran, Y. Zhang, H. Wang, and D.Z. Chen. Segmenting subcellular structures in histology tissue images. In *Biomedical Imaging (ISBI), 2015 IEEE 12th International Symposium on*, pages 556–559, April 2015. doi: 10.1109/ISBI.2015.7163934.

- [62] R. Bensch and O. Ronneberger. Cell segmentation and tracking in phase contrast images using graph cut with asymmetric boundary costs. In *Biomedical Imaging (ISBI), 2015 IEEE 12th International Symposium on*, pages 1220–1223, April 2015. doi: 10.1109/ISBI.2015.7164093.
- [63] DM Greig, BT Porteous, and Allan H Seheult. Exact maximum a posteriori estimation for binary images. *Journal of the Royal Statistical Society. Series B (Methodological)*, pages 271–279, 1989.
- [64] Y. Boykov, O. Veksler, and R. Zabih. Fast approximate energy minimization via graph cuts. In *Computer Vision, 1999. The Proceedings of the Seventh IEEE International Conference on*, volume 1, pages 377–384 vol.1, 1999. doi: 10.1109/ICCV.1999.791245.
- [65] Yuri Boykov and Gareth Funka-Lea. Graph cuts and efficient nd image segmentation. *International journal of computer vision*, 70(2):109–131, 2006.
- [66] Yuri Y Boykov and Marie-Pierre Jolly. Interactive graph cuts for optimal boundary & region segmentation of objects in nd images. In *Computer Vision, 2001. ICCV 2001. Proceedings. Eighth IEEE International Conference on*, volume 1, pages 105–112. IEEE, 2001.
- [67] Y. Al-Kofahi, W. Lassoued, W. Lee, and B. Roysam. Improved automatic detection and segmentation of cell nuclei in histopathology images. *Biomedical Engineering, IEEE Transactions on*, 57(4):841–852, April 2010. ISSN 0018-9294. doi: 10.1109/TBME.2009.2035102.
- [68] Chanho Jung, Changick Kim, Seoung Wan Chae, and Sukjoong Oh. Unsupervised segmentation of overlapped nuclei using bayesian classification. *Biomedical Engineering, IEEE Transactions on*, 57(12):2825–2832, Dec 2010. ISSN 0018-9294. doi: 10.1109/TBME.2010.2060486.
- [69] Hui Kong, M. Gurcan, and K. Belkacem-Boussaid. Partitioning histopathological images: An integrated framework for supervised color-texture segmentation and cell splitting. *Medical Imaging, IEEE Transactions on*, 30(9):1661–1677, Sept 2011. ISSN 0278-0062. doi: 10.1109/TMI.2011.2141674.
- [70] Chao-Hui Huang, Antoine Veillard, Ludovic Roux, Nicolas Lomnie, and Daniel Racoceanu. Time-efficient sparse analysis of histopathological whole slide images. *Computerized Medical Imaging and Graphics*, 35(78):579 – 591, 2011. ISSN 0895-6111. doi: <http://dx.doi.org/10.1016/j.compmedimag.2010.11.009>. Whole Slide Image Process.
- [71] Jia-Mei Chen, Ai-Ping Qu, Lin-Wei Wang, Jing-Ping Yuan, Fang Yang, Qing-Ming Xiang, Ninu Maskey, Gui-Fang Yang, Juan Liu, and Yan Li. New breast cancer prognostic factors identified by computer-aided image analysis of he stained histopathology images. *Scientific Reports*, 5, 2015.

- [72] Hai Su, Fujun Liu, Yuanpu Xie, Fuyong Xing, S. Meyyappan, and Lin Yang. Region segmentation in histopathological breast cancer images using deep convolutional neural network. In *Biomedical Imaging (ISBI), 2015 IEEE 12th International Symposium on*, pages 55–58, April 2015. doi: 10.1109/ISBI.2015.7163815.
- [73] A. Santamaria-Pang, J. Rittscher, M. Gerdes, and D. Padfield. Cell segmentation and classification by hierarchical supervised shape ranking. In *Biomedical Imaging (ISBI), 2015 IEEE 12th International Symposium on*, pages 1296–1299, April 2015. doi: 10.1109/ISBI.2015.7164112.
- [74] H. Su, Z. Yin, S. Huh, T. Kanade, and J. Zhu. Interactive cell segmentation based on active and semi-supervised learning. *Medical Imaging, IEEE Transactions on*, PP (99):1–1, 2015. ISSN 0278-0062. doi: 10.1109/TMI.2015.2494582.
- [75] Yin Zhou, Hang Chang, K.E. Barner, and B. Parvin. Nuclei segmentation via sparsity constrained convolutional regression. In *Biomedical Imaging (ISBI), 2015 IEEE 12th International Symposium on*, pages 1284–1287, April 2015. doi: 10.1109/ISBI.2015.7164109.
- [76] Benoît Lelandais and Frédéric Ducongé. Deconvolution regularized using fuzzy c-means algorithm for biomedical image deblurring and segmentation. In *Biomedical Imaging (ISBI), 2015 IEEE 12th International Symposium on*, pages 1457–1461, April 2015. doi: 10.1109/ISBI.2015.7164151.
- [77] Stephen J Keenan, James Diamond, W Glenn McCluggage, Hoshang Bharucha, Deborah Thompson, Peter H Bartels, and Peter W Hamilton. An automated machine vision system for the histological grading of cervical intraepithelial neoplasia (cin). *The Journal of pathology*, 192(3):351–362, 2000.
- [78] Yin Hai Wang, Danny Crookes, Osama Sharaf Eldin, Shilan Wang, Peter Hamilton, and Jim Diamond. Assisted diagnosis of cervical intraepithelial neoplasia (cin). *Selected Topics in Signal Processing, IEEE Journal of*, 3(1):112–121, 2009.
- [79] P. Guo, K. Banerjee, R.J. Stanley, R. Long, S. Antani, G. Thoma, R. Zuna, S.R. Frazier, R.H. Moss, and W.V. Stoecker. Nuclei-based features for uterine cervical cancer histology image analysis with fusion-based classification. *Biomedical and Health Informatics, IEEE Journal of*, PP(99):1–1, 2015. ISSN 2168-2194. doi: 10.1109/JBHI.2015.2483318.
- [80] Dan C Cireşan, Alessandro Giusti, Luca M Gambardella, and Jürgen Schmidhuber. Mitosis detection in breast cancer histology images with deep neural networks. In *Medical Image Computing and Computer-Assisted Intervention–MICCAI 2013*, pages 411–418. Springer, 2013.
- [81] Sokol Petushi, Fernando U Garcia, Marian M Haber, Constantine Katsinis, and Aydin Tozeren. Large-scale computations on histology images reveal grade-differentiating parameters for breast cancer. *BMC Medical Imaging*, 6(1):14, 2006.

- [82] Jean-romain Dalle, Hao Li, Chao hui Huang, Wee Kheng Leow, Daniel Racoceanu, and Thomas C. Putti. Nuclear pleomorphism scoring by selective cell nuclei detection. *Applications of Computer Vision (WACV)*, IEEE Workshop on, 2009.
- [83] J. Kong, O. Sertel, H. Shimada, K.L. Boyer, J.H. Saltz, and M.N. Gurcan. Computer-aided evaluation of neuroblastoma on whole-slide histology images: Classifying grade of neuroblastic differentiation. *Pattern Recognition*, 42(6):1080 – 1092, 2009. ISSN 0031-3203. doi: <http://dx.doi.org/10.1016/j.patcog.2008.10.035>. *Digital Image Processing and Pattern Recognition Techniques for the Detection of Cancer*.
- [84] E. Cosatto, M. Miller, H.P. Graf, and J.S. Meyer. Grading nuclear pleomorphism on histological micrographs. In *Pattern Recognition, 2008. ICPR 2008. 19th International Conference on*, pages 1–4, Dec 2008. doi: 10.1109/ICPR.2008.4761112.
- [85] JiWan Han, TobyP. Breckon, DavidA. Randell, and Gabriel Landini. The application of support vector machine classification to detect cell nuclei for automated microscopy. *Machine Vision and Applications*, 23(1):15–24, 2012. ISSN 0932-8092. doi: 10.1007/s00138-010-0275-y.
- [86] P. Hufnagl and K. Voss. Ein zeitoptimaler konturfolgealgorithmus (a time-optimal contour search algorithm). *Digitale Bildverarbeitung, Wiss. Beitr. d. TU Dresden*, 1983.
- [87] Gunilla Borgefors. Distance transformations in digital images. *Comput. Vision Graph. Image Process.*, 34(3):344–371, June 1986. ISSN 0734-189X. doi: 10.1016/S0734-189X(86)80047-0.
- [88] Nobuyuki Otsu. A threshold selection method from gray-level histograms. *Systems, Man and Cybernetics, IEEE Transactions on*, 9(1):62–66, Jan 1979. ISSN 0018-9472. doi: 10.1109/TSMC.1979.4310076.
- [89] Carlos Arteta, Victor Lempitsky, J.Alison Noble, and Andrew Zisserman. Learning to detect cells using non-overlapping extremal regions. In Nicholas Ayache, Herv Delingette, Polina Golland, and Kensaku Mori, editors, *Medical Image Computing and Computer-Assisted Intervention MICCAI 2012*, volume 7510 of *Lecture Notes in Computer Science*, pages 348–356. Springer Berlin Heidelberg, 2012. ISBN 978-3-642-33414-6. doi: 10.1007/978-3-642-33415-3_43.
- [90] J Matas, O Chum, M Urban, and T Pajdla. Robust wide-baseline stereo from maximally stable extremal regions. *Image and Vision Computing*, 22(10):761 – 767, 2004. ISSN 0262-8856. doi: <http://dx.doi.org/10.1016/j.imavis.2004.02.006>. *British Machine Vision Computing 2002*.
- [91] A. Hafiane, B. Zavidovique, and S. Chaudhuri. A modified fcm with optimal peano scans for image segmentation. In *Image Processing, 2005. ICIP 2005. IEEE International Conference on*, volume 3, pages III–840–3, Sept 2005. doi: 10.1109/ICIP.2005.1530523.

- [92] Luminita A Vese and Tony F Chan. A multiphase level set framework for image segmentation using the mumford and shah model. *International journal of computer vision*, 50(3):271–293, 2002.
- [93] David Mumford and Jayant Shah. Optimal approximations by piecewise smooth functions and associated variational problems. *Communications on pure and applied mathematics*, 42(5):577–685, 1989.
- [94] T.F. Chan and L.A. Vese. Active contours without edges. *Image Processing, IEEE Transactions on*, 10(2):266–277, Feb 2001. ISSN 1057-7149. doi: 10.1109/83.902291.
- [95] B. Parvin, Qing Yang, Ju Han, Hang Chang, B. Rydberg, and M.H. Barcellos-Hoff. Iterative voting for inference of structural saliency and characterization of subcellular events. *Image Processing, IEEE Transactions on*, 16(3):615–623, March 2007. ISSN 1057-7149. doi: 10.1109/TIP.2007.891154.
- [96] Oliver Schmitt and Maria Hasse. Radial symmetries based decomposition of cell clusters in binary and gray level images. *Pattern Recognition*, 41(6):1905–1923, 2008.
- [97] G. Loy and A. Zelinsky. Fast radial symmetry for detecting points of interest. *Pattern Analysis and Machine Intelligence, IEEE Transactions on*, 25(8):959–973, Aug 2003. ISSN 0162-8828. doi: 10.1109/TPAMI.2003.1217601.
- [98] Min Zhang, T. Wu, and K.M. Bennett. Small blob identification in medical images using regional features from optimum scale. *Biomedical Engineering, IEEE Transactions on*, 62(4):1051–1062, April 2015. ISSN 0018-9294. doi: 10.1109/TBME.2014.2360154.
- [99] Paul Rosin and Tim Ellis. Image difference threshold strategies and shadow detection. In *in Proc. British Machine Vision Conf*, pages 347–356. BMVA Press, 1995.
- [100] P. Saint-Marc, J.-S. Chen, and G. Medioni. Adaptive smoothing: a general tool for early vision. *Pattern Analysis and Machine Intelligence, IEEE Transactions on*, 13(6):514–529, Jun 1991. ISSN 0162-8828. doi: 10.1109/34.87339.
- [101] S. Kumar, Song Han, D. Goldgof, and K. Bowyer. On recovering hyperquadrics from range data. *Pattern Analysis and Machine Intelligence, IEEE Transactions on*, 17(11):1079–1083, Nov 1995. ISSN 0162-8828. doi: 10.1109/34.473234.
- [102] Gunilla Borgefors. On digital distance transforms in three dimensions. *Computer vision and image understanding*, 64(3):368–376, 1996.
- [103] Chenyang Xu and Jerry L Prince. Snakes, shapes, and gradient vector flow. *Image Processing, IEEE Transactions on*, 7(3):359–369, 1998.
- [104] Xianghua Xie and M. Mirmehdi. Mac: Magnetostatic active contour model. *Pattern Analysis and Machine Intelligence, IEEE Transactions on*, 30(4):632–646, April 2008. ISSN 0162-8828. doi: 10.1109/TPAMI.2007.70737.

- [105] Christopher M Bishop. *Neural networks for pattern recognition*. Oxford university press, 1995.
- [106] R. Achanta, A. Shaji, K. Smith, A. Lucchi, P. Fua, and S. Süsstrunk. Slic superpixels compared to state-of-the-art superpixel methods. *Pattern Analysis and Machine Intelligence, IEEE Transactions on*, 34(11):2274–2282, Nov 2012. ISSN 0162-8828. doi: 10.1109/TPAMI.2012.120.
- [107] Pierre Soille. *Morphological image analysis: principles and applications*. Springer Science & Business Media, 2013.
- [108] James Albert Sethian. *Level set methods and fast marching methods: evolving interfaces in computational geometry, fluid mechanics, computer vision, and materials science*, volume 3. Cambridge university press, 1999.
- [109] A. Gamal-Eldin, X. Descombes, and J. Zerubia. Multiple birth and cut algorithm for point process optimization. In *Signal-Image Technology and Internet-Based Systems (SITIS), 2010 Sixth International Conference on*, pages 35–42, Dec 2010. doi: 10.1109/SITIS.2010.17.
- [110] A. Giusti, D.C. Ciresan, J. Masci, L.M. Gambardella, and J. Schmidhuber. Fast image scanning with deep max-pooling convolutional neural networks. In *Image Processing (ICIP), 2013 20th IEEE International Conference on*, pages 4034–4038, Sept 2013. doi: 10.1109/ICIP.2013.6738831.
- [111] Marina E Plissiti, Christophoros Nikou, and Antonia Charchanti. Automated detection of cell nuclei in pap smear images using morphological reconstruction and clustering. *Information Technology in Biomedicine, IEEE Transactions on*, 15(2): 233–241, 2011.
- [112] Meng-Husiun Tsai, Yung-Kuan Chan, Zhe-Zheng Lin, Shys-Fan Yang-Mao, and Po-Chi Huang. Nucleus and cytoplasm contour detector of cervical smear image. *Pattern Recognition Letters*, 29(9):1441–1453, 2008.
- [113] Shys-Fan Yang-Mao, Yung-Kuan Chan, and Yen-Ping Chu. Edge enhancement nucleus and cytoplasm contour detector of cervical smear images. *Systems, Man, and Cybernetics, Part B: Cybernetics, IEEE Transactions on*, 38(2):353–366, 2008.
- [114] Christoph Bergmeir, Miguel García Silvente, and José Manuel Benítez. Segmentation of cervical cell nuclei in high-resolution microscopic images: A new algorithm and a web-based software framework. *Computer methods and programs in biomedicine*, 107(3):497–512, 2012.
- [115] Pei-Yan Pai, Chin-Chen Chang, and Yung-Kuan Chan. Nucleus and cytoplasm contour detector from a cervical smear image. *Expert Systems with Applications*, 39(1):154–161, 2012.

- [116] Marina E Plissiti, Christophoros Nikou, and Antonia Charchanti. Combining shape, texture and intensity features for cell nuclei extraction in pap smear images. *Pattern Recognition Letters*, 32(6):838–853, 2011.
- [117] Negar M Harandi, Saeed Sadri, Noushin A Moghaddam, and Rassul Amirfattahi. An automated method for segmentation of epithelial cervical cells in images of thinprep. *Journal of Medical Systems*, 34(6):1043–1058, 2010.
- [118] Kuan Li, Zhi Lu, Wenyin Liu, and Jianping Yin. Cytoplasm and nucleus segmentation in cervical smear images using radiating gvf snake. *Pattern Recognition*, 45(4):1255–1264, 2012.
- [119] Marina E Plissiti and Christophoros Nikou. Overlapping cell nuclei segmentation using a spatially adaptive active physical model. *Image Processing, IEEE Transactions on*, 21(11):4568–4580, 2012.
- [120] Ling Zhang, Hui Kong, Chien Ting Chin, Shaoxiong Liu, Zhi Chen, Tianfu Wang, and Siping Chen. Segmentation of cytoplasm and nuclei of abnormal cells in cervical cytology using global and local graph cuts. *Computerized Medical Imaging and Graphics*, 38(5):369–380, 2014. ISSN 0895-6111.
- [121] Ling Zhang, Hui Kong, Chien Ting Chin, Shaoxiong Liu, Tianfu Wang, and Siping Chen. Automated segmentation of abnormal cervical cells using global and local graph cuts. In *Biomedical Imaging (ISBI), 2014 IEEE 11th International Symposium on*, pages 485–488. IEEE, 2014.
- [122] N Béliz-Osorio, José Crespo, Marcial García-Rojo, Alberto Muñoz, and Javier Azpiazu. Cytology imaging segmentation using the locally constrained watershed transform. In *Mathematical Morphology and Its Applications to Image and Signal Processing*, pages 429–438. Springer, 2011.
- [123] H.-S. Wu, J. Gil, and J. Barba. Optimal segmentation of cell images. *Vision, Image and Signal Processing, IEE Proceedings -*, 145(1):50–56, Feb 1998. ISSN 1350-245X. doi: 10.1049/ip-vis:19981690.
- [124] Dwiza Riana, Marina E. Plissiti, Christophoros Nikou, Dwi H. Widiantoro, Tati Latifah R. Mengko, and Oemie Kalsoem. Inflammatory cell extraction and nuclei detection in pap smear images. *Int. J. E-Health Med. Commun.*, 6(2):27–43, April 2015. ISSN 1947-315X. doi: 10.4018/IJEHMC.2015040103.
- [125] Izzati Muhimmah, Rahmad Kurniawan, et al. Analysis of features to distinguish epithelial cells and inflammatory cells in pap smear images. In *Biomedical Engineering and Informatics (BMEI), 2013 6th International Conference on*, pages 519–523. IEEE, 2013.

- [126] Roy E Lee, David S McClintock, Nora M Laver, Yukako Yagi, et al. Evaluation and optimization for liquid-based preparation cytology in whole slide imaging. *Journal of pathology Informatics*, 2(1):46, 2011.
- [127] Andrew P Bradley and Pascal C Bamford. A one-pass extended depth of field algorithm based on the over-complete discrete wavelet transform. In *Image and Vision Computing'04 New Zealand (IVCNZ'04)*, pages 279–284. not found, 2004.
- [128] Brigitte Forster, Dimitri Van De Ville, Jesse Berent, Daniel Sage, and Michael Unser. Complex wavelets for extended depth-of-field: a new method for the fusion of multi-channel microscopy images. *Microscopy Research and technique*, 65(LIB-ARTICLE-2004-003):33–42, 2004.
- [129] John Canny. A computational approach to edge detection. *Pattern Analysis and Machine Intelligence, IEEE Transactions on*, (6):679–698, 1986.
- [130] Meng-Hsiun Tsai, Ming-Hung Wang, Ting-Yuan Chang, Pei-Yan Pai, and Yung-Kuan Chan. An adaptable threshold decision method. In *Information Assurance and Security, 2009. IAS'09. Fifth International Conference on*, volume 1, pages 45–48. IEEE, 2009.
- [131] Andrea Vedaldi and Stefano Soatto. Quick shift and kernel methods for mode seeking. In *Computer Vision–ECCV 2008*, pages 705–718. Springer, 2008.
- [132] Mikael Rousson and Nikos Paragios. Shape priors for level set representations. In *Computer Vision–ECCV 2002*, pages 78–92. Springer, 2002.
- [133] Carlo Tomasi and Roberto Manduchi. Bilateral filtering for gray and color images. In *Computer Vision, 1998. Sixth International Conference on*, pages 839–846. IEEE, 1998.
- [134] Karel Zuiderveld. Contrast limited adaptive histogram equalization. In *Graphics gems IV*, pages 474–485. Academic Press Professional, Inc., 1994.
- [135] Richard Nock and Frank Nielsen. Statistical region merging. *Pattern Analysis and Machine Intelligence, IEEE Transactions on*, 26(11):1452–1458, 2004.
- [136] Neerad Phansalkar, Sumit More, Ashish Sabale, and Madhuri Joshi. Adaptive local thresholding for detection of nuclei in diversity stained cytology images. In *Communications and Signal Processing (ICCSP), 2011 International Conference on*, pages 218–220. IEEE, 2011.
- [137] Olga Veksler. Star shape prior for graph-cut image segmentation. In *Computer Vision–ECCV 2008*, pages 454–467. Springer, 2008.

- [138] Navneet Dalal and Bill Triggs. Histograms of oriented gradients for human detection. In *Computer Vision and Pattern Recognition, 2005. CVPR 2005. IEEE Computer Society Conference on*, volume 1, pages 886–893. IEEE, June 2005. doi: 10.1109/CVPR.2005.177.
- [139] Hady Ahmady Phoulady, Dmitry B. Goldgof, Lawrence O. Hall, and Peter R. Mouton. Nucleus segmentation in histology images with hierarchical multilevel thresholding. In *SPIE Medical Imaging Symposium: Digital Pathology*, pages 979111–979111. International Society for Optics and Photonics, 2016.
- [140] H. Fatakdawala, Jun Xu, A. Basavanahally, G. Bhanot, S. Ganesan, M. Feldman, J. E. Tomaszewski, and A. Madabhushi. Expectation maximization-driven geodesic active contour with overlap resolution (emagacor): Application to lymphocyte segmentation on breast cancer histopathology. *Biomedical Engineering, IEEE Transactions on*, 57(7):1676–1689, July 2010. ISSN 0018-9294. doi: 10.1109/TBME.2010.2041232.
- [141] Po-Whei Huang and Yan-Hao Lai. Effective segmentation and classification for hcc biopsy images. *Pattern Recognition*, 43(4):1550 – 1563, 2010. ISSN 0031-3203. doi: <http://dx.doi.org/10.1016/j.patcog.2009.10.014>.
- [142] P. S. Liao, T. S. Chen, and P. C. Chung. A fast algorithm for multilevel thresholding. *Journal of Information Science and Engineering*, 17:713–727, 2001.
- [143] Baishali Chaudhury, Hady Ahmady Phoulady, Dmitry B. Goldgof, Lawrence O. Hall, Peter R. Mouton, Ardeshir Hakam, and Erin M. Siegel. An ensemble algorithm framework for automated stereology of cervical cancer. In Alfredo Petrosino, editor, *2013 International Conference on Image Analysis and Processing (ICIAP)*, volume 8156 of *Lecture Notes in Computer Science*, pages 823–832. Springer Berlin Heidelberg, 2013. ISBN 978-3-642-41180-9. doi: 10.1007/978-3-642-41181-6_83.
- [144] Hady Ahmady Phoulady, Baishali Chaudhury, Dmitry B. Goldgof, Lawrence O. Hall, Peter R. Mouton, Ardeshir Hakam, and Erin M. Siegel. Experiments with large ensembles for segmentation and classification of cervical cancer biopsy images. In *2014 IEEE International Conference on Systems, Man, and Cybernetics (SMC)*, pages 870–875, Oct 2014. doi: 10.1109/SMC.2014.6974021.
- [145] F. B. Sørensen, P. Bichel, and A. Jakobsen. DNA level and stereologic estimates of nuclear volume in squamous cell carcinomas of the uterine cervix. a comparative study with analysis of prognostic impact. *Cancer*, 69(1):187–199, 1992. ISSN 1097-0142. doi: 10.1002/1097-0142(19920101)69:1<187::AID-CNCR2820690131>3.0.CO;2-R.
- [146] Pranab Dey and Manish Powari. Mean nuclear volume in cervical intraepithelial neoplasia and carcinoma. *Analytical and Quantitative Cytology and Histology*, 24(2): 70–72, 2002. ISSN 0884-6812.

- [147] A. Alush and J. Goldberger. Ensemble segmentation using efficient integer linear programming. *Pattern Analysis and Machine Intelligence, IEEE Transactions on*, 34(10):1966–1977, Oct 2012. ISSN 0162-8828. doi: 10.1109/TPAMI.2011.280.
- [148] G. Rafiee, S. S. Dlay, and W. L. Woo. Automatic segmentation of interest regions in low depth of field images using ensemble clustering and graph cut optimization approaches. In *Multimedia (ISM), 2012 IEEE International Symposium on*, pages 161–164, Dec 2012. doi: 10.1109/ISM.2012.39.
- [149] Y. Gu, V. Kumar, L. O. Hall, D. B. Goldgof, C. Li, R. Korn, C. Bendtsen, E. Rios Velazquez, A. Dekker, H. Aerts, P. Lambin, X. Li, J. Tian, R. A. Gatenby, and R. J. Gillies. Automated delineation of lung tumors from {CT} images using a single click ensemble segmentation approach. *Pattern Recognition*, 46(3):692 – 702, 2013. ISSN 0031-3203. doi: <http://dx.doi.org/10.1016/j.patcog.2012.10.005>.
- [150] V. Manohar, S. N. Vitaladevuni, H. Cao, R. Prasad, and P. Natarajan. Graph clustering-based ensemble method for handwritten text line segmentation. In *Document Analysis and Recognition (ICDAR), 2011 International Conference on*, pages 574–578, Sept 2011. doi: 10.1109/ICDAR.2011.121.
- [151] S. Avidan. Ensemble methods for tracking and segmentation (abstract). In C. Sansone, J. Kittler, and F. Roli, editors, *Multiple Classifier Systems*, volume 6713 of *Lecture Notes in Computer Science*, pages 1–1. Springer Berlin Heidelberg, 2011. ISBN 978-3-642-21556-8. doi: 10.1007/978-3-642-21557-5_1.
- [152] L. Franek, D. D. Abdala, S. Vega-Pons, and X. Jiang. Image segmentation fusion using general ensemble clustering methods. In R. Kimmel, R. Klette, and A. Sugimoto, editors, *Computer Vision ACCV 2010*, volume 6495 of *Lecture Notes in Computer Science*, pages 373–384. Springer Berlin Heidelberg, 2011. ISBN 978-3-642-19281-4. doi: 10.1007/978-3-642-19282-1_30.
- [153] H. B. Mitchell. Ensemble color image segmentation. In *Image Fusion*, pages 229–232. Springer Berlin Heidelberg, 2010. ISBN 978-3-642-11215-7. doi: 10.1007/978-3-642-11216-4_20.
- [154] P. Wattuya and X. Jiang. Ensemble combination for solving the parameter selection problem in image segmentation. In N. Vitoria Lobo, T. Kasparis, F. Roli, J. T. Kwok, M. Georgiopoulos, G. C. Anagnostopoulos, and M. Loog, editors, *Structural, Syntactic, and Statistical Pattern Recognition*, volume 5342 of *Lecture Notes in Computer Science*, pages 392–401. Springer Berlin Heidelberg, 2008. ISBN 978-3-540-89688-3. doi: 10.1007/978-3-540-89689-0_43.

- [155] L. Franek and X. Jiang. Adaptive parameter selection for image segmentation based on similarity estimation of multiple segmenters. In R. Kimmel, R. Klette, and A. Sugimoto, editors, *Computer Vision ACCV 2010*, volume 6493 of *Lecture Notes in Computer Science*, pages 697–708. Springer Berlin Heidelberg, 2011. ISBN 978-3-642-19308-8. doi: 10.1007/978-3-642-19309-5_54.
- [156] L. Shoemaker and L. O. Hall. Anomaly detection using ensembles. In Carlo Sansone, Josef Kittler, and Fabio Roli, editors, *Multiple Classifier Systems*, volume 6713 of *Lecture Notes in Computer Science*, pages 6–15. Springer Berlin Heidelberg, 2011. ISBN 978-3-642-21556-8. doi: 10.1007/978-3-642-21557-5_3.
- [157] R. E. Banfield, L. O. Hall, K. W. Bowyer, and W. P. Kegelmeyer. A comparison of decision tree ensemble creation techniques. *Pattern Analysis and Machine Intelligence, IEEE Transactions on*, 29(1):173–180, Jan 2007. ISSN 0162-8828. doi: 10.1109/TPAMI.2007.250609.
- [158] RD Dony. Karhunen-loeve transform. *The transform and data compression handbook*, pages 20–55, 2001.
- [159] F. B. Sørensen, P. Bichel, and A. Jakobsen. Stereological estimates of nuclear volume in squamous cell carcinoma of the uterine cervix and its precursors. *Virchows Archiv A*, 418(3):225–233, 1991. ISSN 0174-7398. doi: 10.1007/BF01606060.
- [160] Hady Ahmady Phoulady, Mu Zhou, Dmitry B Goldgof, Lawrence O Hall, and Peter R Mouton. Automatic quantification and classification of cervical cancer via adaptive nucleus shape modeling. In *2016 IEEE International Conference on Image Processing (ICIP)*, pages 2658–2662. IEEE, 2016.
- [161] L. J. van Bogaert. Influence of knowledge of human immunodeficiency virus serostatus on accuracy of cervical cytologic diagnosis. *Cancer Cytopathology*, 122(12):909913, 2014.
- [162] X. Zhang, L. Yang, W. Liu, H. Su, and S. Zhang. Mining histopathological images via composite hashing and online learning. In Polina Golland, Nobuhiko Hata, Christian Barillot, Joachim Hornegger, and Robert Howe, editors, *MICCAI 2014*, volume 8674 of *LNCS*, pages 479–486. Springer International Publishing, 2014. ISBN 978-3-319-10469-0. doi: 10.1007/978-3-319-10470-6_60.
- [163] C. W. Wang and C. P. Yu. Automated morphological classification of lung cancer subtypes using h&e tissue images. *Machine Vision and Applications*, 24(7):1383–1391, 2013. ISSN 0932-8092. doi: 10.1007/s00138-012-0457-x.
- [164] James Diamond, Neil H. Anderson, Peter H. Bartels, Rodolfo Montironi, and Peter W. Hamilton. The use of morphological characteristics and texture analysis in the identification of tissue composition in prostatic neoplasia. *Human Pathology*, 35(9):1121 – 1131, 2004. ISSN 0046-8177. doi: <http://dx.doi.org/10.1016/j.humpath.2004.05.010>.

- [165] H. Chang, Y. Zhou, A. Borowsky, K. Barner, P. Spellman, and B. Parvin. Stacked predictive sparse decomposition for classification of histology sections. *International Journal of Computer Vision*, pages 1–16, 2014. ISSN 0920-5691. doi: 10.1007/s11263-014-0790-9.
- [166] J. C. Caicedo, A. Cruz, and F. A. Gonzalez. Histopathology image classification using bag of features and kernel functions. In Carlo Combi, Yuval Shahar, and Ameen Abu-Hanna, editors, *Artificial Intelligence in Medicine*, volume 5651 of *LNCS*, pages 126–135. Springer Berlin Heidelberg, 2009. ISBN 978-3-642-02975-2. doi: 10.1007/978-3-642-02976-9_17.
- [167] S. Lazebnik, C. Schmid, and J. Ponce. Beyond bags of features: Spatial pyramid matching for recognizing natural scene categories. In *CVPR, 2006 IEEE Computer Society Conference on*, volume 2, pages 2169–2178, 2006. doi: 10.1109/CVPR.2006.68.
- [168] J. Yang, K. Yu, Y. Gong, and T. Huang. Linear spatial pyramid matching using sparse coding for image classification. In *Computer Vision and Pattern Recognition, 2009. CVPR 2009. IEEE Conference on*, pages 1794–1801, June 2009. doi: 10.1109/CVPR.2009.5206757.
- [169] Y. Zhang, B. Zhang, F. Coenen, and W. Lu. Breast cancer diagnosis from biopsy images with highly reliable random subspace classifier ensembles. *Machine Vision and Applications*, 24(7):1405–1420, 2013. ISSN 0932-8092. doi: 10.1007/s00138-012-0459-8.
- [170] Sonal Kothari, John H. Phan, Andrew N. Young, and May D. Wang. Histological image classification using biologically interpretable shape-based features. *BMC Medical Imaging*, 13(1):1–17, 2013. ISSN 1471-2342. doi: 10.1186/1471-2342-13-9.
- [171] P. F. Felzenszwalb, R. B. Girshick, D. McAllester, and D. Ramanan. Object detection with discriminatively trained part-based models. *Pattern Analysis and Machine Intelligence, IEEE Transactions on*, 32(9):1627–1645, Sept 2010. ISSN 0162-8828. doi: 10.1109/TPAMI.2009.167.
- [172] Hady Ahmady Phoulady, Dmitry B. Goldgof, Lawrence O. Hall, and Peter R. Mouton. A new approach to detect and segment overlapping cells in multi-layer cervical cell volume images. In *2016 IEEE 13th International Symposium on Biomedical Imaging (ISBI)*, pages 201–204, April 2016. doi: 10.1109/ISBI.2016.7493244.
- [173] Hady Ahmady Phoulady, Dmitry B. Goldgof, Lawrence O. Hall, and Peter R. Mouton. A framework for nucleus and overlapping cytoplasm segmentation in cervical cytology extended depth of field and volume images. *Under review for Computerized Medical Imaging and Graphics*, submitted on October 11, 2016.

- [174] Diane Solomon, Diane Davey, Robert Kurman, Ann Moriarty, Dennis O'Connor, Marianne Prey, Stephen Raab, Mark Sherman, David Wilbur, Thomas Wright Jr, et al. The 2001 Bethesda system: terminology for reporting results of cervical cytology. *Jama*, 287(16):2114–2119, 2002.
- [175] Eileen M Burd. Human papillomavirus and cervical cancer. *Clinical microbiology reviews*, 16(1):1–17, 2003.
- [176] Yilun Fan and Andrew P. Bradley. A method for quantitative analysis of clump thickness in cervical cytology slides. *Micron*, 80:73–82, 2016. ISSN 0968-4328.
- [177] Z. Lu, G. Carneiro, A. Bradley, D. Ushizima, M. S. Nosrati, A. Bianchi, C. Carneiro, and G. Hamarneh. Evaluation of three algorithms for the segmentation of overlapping cervical cells. *IEEE Journal of Biomedical and Health Informatics*, PP(99):1–1, 2016. ISSN 2168-2194. doi: 10.1109/JBHI.2016.2519686.
- [178] A. Tareef, Y. Song, W. Cai, D. D. Feng, and M. Chen. Automated three-stage nucleus and cytoplasm segmentation of overlapping cells. In *Control Automation Robotics Vision (ICARCV), 2014 13th International Conference on*, pages 865–870, Dec 2014. doi: 10.1109/ICARCV.2014.7064418.
- [179] Hansang Lee and Junmo Kim. Segmentation of overlapping cervical cells in microscopic images with superpixel partitioning and cell-wise contour refinement. In *Proceedings of the IEEE Conference on Computer Vision and Pattern Recognition Workshops*, pages 63–69, 2016.
- [180] Andrea Vedaldi and Stefano Soatto. Quick shift and kernel methods for mode seeking. In *European Conference on Computer Vision*, pages 705–718. Springer, 2008.
- [181] Daniela M Ushizima, Andrea GC Bianchi, and Claudia M Carneiro. Segmentation of subcellular compartments combining superpixel representation with voronoi diagrams. Overlapping Cervical Cytology Image Segmentation Challenge, IEEE ISBI, Beijing, China, April 2014. 1st Place.
- [182] GW Zack, WE Rogers, and SA Latt. Automatic measurement of sister chromatid exchange frequency. *Journal of Histochemistry & Cytochemistry*, 25(7):741–753, 1977.
- [183] Jae S. Lim. *Two-dimensional Signal and Image Processing*. Prentice-Hall, Inc., Upper Saddle River, NJ, USA, 1990. ISBN 0-13-935322-4.
- [184] Jack E Bresenham. Algorithm for computer control of a digital plotter. *IBM Systems journal*, 4(1):25–30, 1965.
- [185] Abraham Savitzky and Marcel JE Golay. Smoothing and differentiation of data by simplified least squares procedures. *Analytical chemistry*, 36(8):1627–1639, 1964.

Appendices

Appendix A Permissions for Use

Permissions to use images in Fig. 1.1 and Fig. 2.2 are acquired through RightsLink[®].

Fair use of images in Fig. 2.1 is permitted (Creative Commons License ¹).

Images in Fig. 2.3 are taken from [91] which are taken from open-access article [22] and is permitted to be used in this work.

No permission is required to use images in Fig. 2.4, which are taken from an IEEE publication, in this work.

License Details

This is a License Agreement between Hady Ahmady Phoulady ("You") and Nature Publishing Group ("Nature Publishing Group"). The license consists of your order details, the terms and conditions provided by Nature Publishing Group, and the [payment terms and conditions](#).

[Get the printable license](#).

License Number	3784350438350
License date	Jan 08, 2016
Licensed Content Publisher	Nature Publishing Group
Licensed Content Publication	Nature Reviews Cancer
Licensed Content Title	The natural history of cervical HPV infection: unresolved issues
Licensed Content Author	Ciaran B. J. Woodman, Stuart I. Collins and Lawrence S. Young
Licensed Content Date	Jan 1, 2007
Type of Use	reuse in a dissertation / thesis
Volume number	7
Issue number	1
Requestor type	academic/educational
Format	print and electronic
Portion	figures/tables/illustrations
Number of figures/tables/illustrations	1
High-res required	no
Figures	Progression from HPV infection to invasive cancer.
Author of this NPG article	no
Your reference number	16
Title of your thesis / dissertation	Algorithms for Nucleus Detection and Segmentation in Microscopy Images
Expected completion date	Aug 2016
Estimated size (number of pages)	100
Total	0.00 USD

¹<http://creativecommons.org/licenses/by-nc-sa/3.0/>

Appendix A (Continued)

License Details

Thank you very much for your order.

This is a License Agreement between Hady Ahmady Phoulady ("You") and Elsevier ("Elsevier"). The license consists of your order details, the terms and conditions provided by Elsevier, and the [payment terms and conditions](#).

[Get the printable license.](#)

License Number	3784360449127
License date	Jan 08, 2016
Licensed Content Publisher	Elsevier
Licensed Content Publication	The Lancet
Licensed Content Title	Human papillomavirus and cervical cancer
Licensed Content Author	Mark Schiffman, Philip E Castle, Jose Jeronimo, Ana C Rodriguez, Sholom Wacholder
Licensed Content Date	8–14 September 2007
Licensed content volume number	370
Licensed content issue number	9590
Number of pages	18
Type of Use	reuse in a thesis/dissertation
Portion	figures/tables/illustrations
Number of figures/tables/illustrations	4
Format	both print and electronic
Are you the author of this Elsevier article?	No
Will you be translating?	No
Original figure numbers	3
Title of your thesis/dissertation	Algorithms for Nucleus Detection and Segmentation in Microscopy Images
Expected completion date	Aug 2016
Estimated size (number of pages)	100
Elsevier VAT number	GB 494 6272 12
Price	0.00 USD
VAT/Local Sales Tax	0.00 USD / 0.00 GBP
Total	0.00 USD


License Details

This is a License Agreement between Hady Ahmady Phoulady ("You") and Springer ("Springer"). The license consists of your order details, the terms and conditions provided by Springer, and the [payment terms and conditions](#).

[Get the printable license.](#)

License Number	3784370720034
License date	Jan 08, 2016
Licensed Content Publisher	Springer
Licensed Content Publication	Springer eBook
Licensed Content Title	Fuzzy Clustering and Active Contours for Histopathology Image Segmentation and Nuclei Detection
Licensed Content Author	Adel Hafiane
Licensed Content Date	Jan 1, 2008
Type of Use	Thesis/Dissertation
Portion	Figures/tables/illustrations
Number of figures/tables/illustrations	1
Author of this Springer article	No
Order reference number	39
Original figure numbers	4
Title of your thesis / dissertation	Algorithms for Nucleus Detection and Segmentation in Microscopy Images
Expected completion date	Aug 2016
Estimated size(pages)	100
Total	0.00 USD

Appendix A (Continued)


Attribution-NonCommercial-ShareAlike 3.0 Unported (CC BY-NC-SA 3.0)

This is a human-readable summary of (and not a substitute for) the [license](#).

[Disclaimer](#)


You are free to:


Share — copy and redistribute the material in any medium or format


Adapt — remix, transform, and build upon the material

The licensor cannot revoke these freedoms as long as you follow the license terms.

Under the following terms:

 **Attribution** — You must give **appropriate credit**, provide a link to the license, and **indicate if changes were made**. You may do so in any reasonable manner, but not in any way that suggests the licensor endorses you or your use.

 **NonCommercial** — You may not use the material for **commercial purposes**.

 **ShareAlike** — If you remix, transform, or build upon the material, you must distribute your contributions under the **same license** as the original.

No additional restrictions — You may not apply legal terms or **technological measures** that legally restrict others from doing anything the license permits.

Notices:

You do not have to comply with the license for elements of the material in the public domain or where your use is permitted by an applicable **exception or limitation**.

No warranties are given. The license may not give you all of the permissions necessary for your intended use. For example, other rights such as **publicity, privacy, or moral rights** may limit how you use the material.

Appendix A (Continued)

Copyright: © 2013 Veta et al. This is an open-access article distributed under the terms of the Creative Commons Attribution License, which permits unrestricted use, distribution, and reproduction in any medium, provided the original author and source are credited.

Thesis / Dissertation Reuse

The IEEE does not require individuals working on a thesis to obtain a formal reuse license, however, you may print out this statement to be used as a permission grant:

Requirements to be followed when using any portion (e.g., figure, graph, table, or textual material) of an IEEE copyrighted paper in a thesis:

- 1) In the case of textual material (e.g., using short quotes or referring to the work within these papers) users must give full credit to the original source (author, paper, publication) followed by the IEEE copyright line © 2011 IEEE.
- 2) In the case of illustrations or tabular material, we require that the copyright line © [Year of original publication] IEEE appear prominently with each reprinted figure and/or table.
- 3) If a substantial portion of the original paper is to be used, and if you are not the senior author, also obtain the senior author's approval.

Requirements to be followed when using an entire IEEE copyrighted paper in a thesis:

- 1) The following IEEE copyright/ credit notice should be placed prominently in the references: © [year of original publication] IEEE. Reprinted, with permission, from [author names, paper title, IEEE publication title, and month/year of publication]
- 2) Only the accepted version of an IEEE copyrighted paper can be used when posting the paper or your thesis on-line.
- 3) In placing the thesis on the author's university website, please display the following message in a prominent place on the website: In reference to IEEE copyrighted material which is used with permission in this thesis, the IEEE does not endorse any of [university/educational entity's name goes here]'s products or services. Internal or personal use of this material is permitted. If interested in reprinting/republishing IEEE copyrighted material for advertising or promotional purposes or for creating new collective works for resale or redistribution, please go to http://www.ieee.org/publications_standards/publications/rights/rights_link.html to learn how to obtain a License from RightsLink.

If applicable, University Microfilms and/or ProQuest Library, or the Archives of Canada may supply single copies of the dissertation.

About the Author

Hady Ahmady Phoulady obtained his Bachelor of Science in Pure Mathematics from Shahid Beheshti University (Tehran, Iran) in 2007. He obtained two Master of Science degrees in Mathematics and Financial Mathematics from Uppsala University (Uppsala, Sweden) in 2012. He joined the Department of Computer Science and Engineering in 2013 and obtained his Master of Science in Computer Science and Engineering in 2015. His research interests are medical image analysis, machine learning, and biomedical image segmentation.